ARMY RESEARCH LABORATORY

Formation of Gaps at the Specimen-Bar Interfaces in Numerical Simulations of Compression Hopkinson Bar Tests on Soft, Nearly Incompressible Materials

by Mike Scheidler and Martin N. Raftenberg

ARL-TR-5301 **September 2010**

NOTICES

Disclaimers

The findings in this report are not to be construed as an official Department of the Army position unless so designated by other authorized documents.

Citation of manufacturer's or trade names does not constitute an official endorsement or approval of the use thereof.

Destroy this report when it is no longer needed. Do not return it to the originator.

Army Research Laboratory
Aberdeen Proving Ground, MD 21005-5066

ARL-TR-5301 **September 2010**

Formation of Gaps at the Specimen-Bar Interfaces in Numerical Simulations of Compression Hopkinson Bar Tests on Soft, Nearly Incompressible Materials

Mike Scheidler and Martin N. Raftenberg
Weapons and Materials Research Directorate, ARL

REPORT DOCUMENTATION PAGE

Form Approved
OMB No. 0704-0188

1. REPORT DATE *(DD-MM-YYYY)*	2. REPORT TYPE	3. DATES COVERED (From - To)
September 2010	Final	July 2008–December 2009

4. TITLE AND SUBTITLE
Formation of Gaps at the Specimen-Bar Interfaces in Numerical Simulations of Compression Hopkinson Bar Tests on Soft, Nearly Incompressible Materials

5a. CONTRACT NUMBER

5b. GRANT NUMBER

5c. PROGRAM ELEMENT NUMBER

6. AUTHOR(S)
Mike Scheidler and Martin N. Raftenberg

5d. PROJECT NUMBER
105

5e. TASK NUMBER

5f. WORK UNIT NUMBER

7. PERFORMING ORGANIZATION NAME(S) AND ADDRESS(ES)
U.S. Army Research Laboratory
ATTN: RDRL-WMP-B
Aberdeen Proving Ground, MD 21005-5066

8. PERFORMING ORGANIZATION REPORT NUMBER
ARL-TR-5301

9. SPONSORING/MONITORING AGENCY NAME(S) AND ADDRESS(ES)

10. SPONSOR/MONITOR'S ACRONYM(S)

11. SPONSOR/MONITOR'S REPORT NUMBER(S)

12. DISTRIBUTION/AVAILABILITY STATEMENT
Approved for public release; distribution is unlimited.

13. SUPPLEMENTARY NOTES

14. ABSTRACT
Numerical simulations of compression Hopkinson bar tests on soft, nearly incompressible materials were performed in an effort to understand inertial effects in these tests. The specimen was modeled as either a linear elastic or a nonlinear elastic solid; the nonlinear model was calibrated to ballistic gelatin data. The simulations revealed a previously unreported phenomenon, namely, for sufficiently high strain rates in the specimen and sufficiently short rise times to the final strain rate, small gaps formed at both the specimen-incident bar and the specimen-transmission bar interfaces. The size of these gaps ranged from sub-micron to as large as 43 μm. Gaps formed at small specimen strains but persisted out to large strains, closing and re-opening multiple times. At some instants the gaps extended over most of the face of the specimen. Unloading of the specimen and the pressure bars accompanied these gaps. In an effort to rule out numerical artifacts, the sensitivity of these results to mesh size and contact algorithm parameters was studied.

15. SUBJECT TERMS
Hopkinson bar, gaps, nearly incompressible, Mooney-Rivlin, inertial effects

16. SECURITY CLASSIFICATION OF:			17. LIMITATION OF ABSTRACT	18. NUMBER OF PAGES	19a. NAME OF RESPONSIBLE PERSON
a. REPORT	b. ABSTRACT	c. THIS PAGE			Mike Scheidler
Unclassified	Unclassified	Unclassified	UU	122	19b. TELEPHONE NUMBER (*Include area code*) 410-278-5436

Standard Form 298 (Rev. 8/98)
Prescribed by ANSI Std. Z39.18

Contents

List of Figures v

List of Tables viii

Acknowledgments ix

1. Introduction 1

2. Problem Description 3

2.1 Problem Geometry 3

2.2 Loading and Boundary Conditions....5

2.3 Material Properties 6

2.4 Wave Speeds and Travel Times 8

2.5 Measurement of Gap Size 10

2.6 Stress, Stretch and Strain....11

3. The Mooney-Rivlin Constitutive Model for the Specimen 14

3.1 Incompressible and Compressible Versions....14

3.2 Calibration of the Mooney-Rivlin Model for Ballistic Gelatin....15

4. Computational Parameters 16

4.1 Geometry and Meshing 16

4.2 Boundary Conditions....17

4.3 Miscellaneous....18

5. Wave Propagation in the Pressure Bars 18

5.1 General Remarks 18

5.2 Considerations Governing the Bar Lengths 19

5.3 Velocity Histories in the Incident Bar....20

6. Simulations with the Moony-Rivlin Model and a 1-μs Rise Time 25

6.1 Results on the Centerline....25

6.1.1 General Remarks 26
6.1.2 The Initial Loading of the Specimen: Stage I (140–165 μs) 32
6.1.3 Gap Opening and Closure (Stages II–VI) 34
6.2 Results at Other Radial Locations 35
6.3 Pressure Contours 38
6.4 Effects of Pressure Bar Radius on Gap Formation 47

7. Simulations with the Moony-Rivlin Model and a 25-μs Rise Time 49
7.1 Results on the Centerline 49
7.1.1 General Remarks 49
7.1.2 The Initial Loading of the Specimen: Stage I (143–184 μs) 54
7.1.3 Gap Opening and Closure (Stages II–IV) 55
7.2 Gap Size vs. Radius at Selected Times 56
7.3 Force History in the Transmission Bar 57

8. Simulations with a Linear Elastic Model for the Specimen 61
8.1 The 1-μs Initial Rise Time 61
8.2 The 25-μs Initial Rise Time 67

9. Discussion and Concluding Remarks 72

10. References 75

Appendix A. The Mooney-Rivlin Constitutive Model 79

Appendix B. Sensitivity Studies 85

Appendix C. Additional Computational Studies 99

List of Symbols, Abbreviations, and Acronyms 104

Distribution List 106

List of Figures

Figure 1. Geometry and coordinate system for the SHPB simulations (not drawn to scale). 4

Figure 2. Meshes for the Incident Bar (IB), Transmission Bar (TB), and Specimen (S). The baseline mesh for the specimen is shown in case (a). 17

Figure 3. The scaled axial velocity vs. non-dimensional time at three locations on the centerline of the incident bar: the loading end with a 1-μs rise time, 1/3 of the way from the loading end, and 2/3 of the way from the loading end (blue curve). 21

Figure 4. The scaled axial velocity vs. non-dimensional time at three locations on the centerline of the incident bar: the loading end with a 25-μs rise time, 1/3 of the way from the loading end, and 2/3 of the way from the loading end (blue curve). 22

Figure 5. The scaled axial velocity history on the centerline of the incident bar at the S-IB interface for a 1-μs (initial) rise time. 23

Figure 6. The scaled axial velocity history on the centerline of the incident bar at the S-IB interface for a 25-μs (initial) rise time. 24

Figure 7. The histories of the axial displacement of the incident bar and the specimen on the centerline at the S-IB interface. Also shown is the history of the corresponding gap size (blue). 26

Figure 8. The histories of the axial displacement of the transmission bar and the specimen on the centerline at the S-TB interface. Also shown is the history of the corresponding gap size (blue). 27

Figure 9. A comparison of the histories of the gap sizes on the centerline at the S-IB and S-TB interfaces. Also shown is the history of mean axial stretch in the specimen (blue). 28

Figure 10. A comparison of the histories of the gap sizes on the centerline at the S-IB and S-TB interfaces in the vicinity of the time at which they first form. Also shown is the history of mean axial stretch in the specimen (blue). 29

Figure 11. Histories of the axial stress (negative in compression) and the gap size on the centerline at the S-IB interface. The stress is measured at the centroids of the specimen and incident bar elements adjacent to the centerline. 31

Figure 12. Histories of the axial stress (negative in compression) and the gap size on the centerline at the S-TB interface. The stress is measured at the centroids of the specimen and transmission bar elements adjacent to the centerline. 32

Figure 13. Deformed mesh plots in the vicinity of the specimen at $t = 236$ μs and an axial strain of 21%: (a) full specimen mesh; (b) enlargement of the mesh near the centerline, where the gap size is about 37 μm. 36

Figure 14. Gap size vs. deformed specimen radius at the S-IB interface at selected times. 37

Figure 15. Gap size vs. deformed specimen radius at the S-IB interface at selected times. 37

Figure 16. Gap size vs. deformed specimen radius at the S-TB interface at selected times. 38

Figure 17. Pressure contours in the vicinity of the specimen at selected times. 40

Figure 18. Pressure contours in the vicinity of the specimen at selected times. 41
Figure 19. Pressure contours in the vicinity of the specimen at selected times. 42
Figure 20. Pressure contours in the vicinity of the specimen at selected times. 43
Figure 21. Pressure contours in the vicinity of the specimen at selected times. 45
Figure 22. Pressure contours in the vicinity of the specimen at selected times. 46
Figure 23. Pressure contours in the vicinity of the specimen at selected times. 47
Figure 24: Histories of the gap size on the centerline at the S-IB interface (top) and S-TB interface (bottom) for two different bar radii. 48
Figure 25. Histories of the gap size on the centerline at the S-IB interface for two loading waves with different initial rise times. 50
Figure 26. Histories of the gap size on the centerline at the S-TB interface for two loading waves with different initial rise times. 51
Figure 27. Histories of the axial stress (negative in compression) and the gap size on the centerline at the S-IB interface. The stress is measured at the centroids of the specimen and incident bar elements adjacent to the centerline. 52
Figure 28. Histories of the axial stress (negative in compression) and the gap size on the centerline at the S-TB interface. The stress is measured at the centroids of the specimen and incident bar elements adjacent to the centerline. 53
Figure 29. Gap size vs. deformed specimen radius at the S-IB interface at selected times. 57
Figure 30. History of the total force (positive in compression) at the stress gage location in the transmission bar (2.52 mm from the specimen interface) compared with the history of the gap size on the centerline at the S-TB interface. 58
Figure 31. A comparison of the histories of the gap sizes on the centerline at the S-IB and S-TB interfaces for a 1-μs rise time and $\nu = 0.49999$ (linear elastic model). Also shown is the history of mean axial stretch in the specimen (blue). 62
Figure 32. A comparison of the histories of the gap sizes on the centerline at the S-IB interface for a 1-μs rise time and selected values of Poisson's ratio (linear elastic model). 63
Figure 33. A comparison of the histories of the gap sizes on the centerline at the S-TB interface for a 1-μs rise time and selected values of Poisson's ratio (linear elastic model). 64
Figure 34. The maximum gap size at the centerline for each interface as a function of Poisson's ratio (linear elastic model, 1-μs rise time). 65
Figure 35. Deformed mesh in the vicinity of the specimen at $t = 276$ μs for Poisson's ratio $\nu = 0.4990$ (linear elastic model, 1-μs rise time). 66
Figure 36. A comparison of the histories of the gap sizes on the centerline at the S-IB and S-TB interfaces for a 25-μs rise time and $\nu = 0.49999$ (linear elastic model). Also shown is the history of mean axial stretch in the specimen (blue). 67
Figure 37. A comparison of the histories of the gap sizes on the centerline at the S-IB interface for a 25-μs rise time and selected values of Poisson's ratio (linear elastic model). 68

Figure 38. A comparison of the histories of the gap sizes on the centerline at the S-TB interface for a 25-μs rise time and selected values of Poisson's ratio (linear elastic model). 69

Figure 39. The maximum gap size at the centerline for each interface as a function of Poisson's ratio (linear elastic model, 25-μs rise time). 70

Figure 40. Deformed mesh in the vicinity of the specimen at $t = 286$ μs for Poisson's ratio $\nu = 0.4990$ (linear elastic model, 25-μs rise time). 71

Figure A-1. Stress components as a function of axial stretch λ_z for a uniaxial stress test on a single element using the compressible Mooney-Rivlin model with $\nu = 0.495$ (colored curves). Comparison with axial stress σ_{zz} for the incompressible model (dashed curve). 84

Figure B-1. Histories of the gap sizes on the centerline at the S-IB interface for three specimen meshes and a 1-μs initial rise time for the loading wave. 86

Figure B-2. Histories of the gap sizes on the centerline at the S-TB interface for three specimen meshes and a 1-μs initial rise time for the loading wave. 87

Figure B-3. Histories of the gap sizes on the centerline at the S-IB interface for three specimen meshes and a 25-μs initial rise time for the loading wave. 88

Figure B-4. Histories of the gap sizes on the centerline at the S-TB interface for three specimen meshes and a 25-μs initial rise time for the loading wave. 89

Figure B-5. Histories of the gap sizes on the centerline at the S-IB interface for three values of the contact parameter SFACT and a 1-μs initial rise time for the loading wave. 91

Figure B-6. Histories of the gap sizes on the centerline at the S-TB interface for three values of the contact parameter SFACT and a 1-μs initial rise time for the loading wave. 92

Figure B-7. Histories of the gap sizes on the centerline at the S-IB interface for two values of the contact parameter VDC and a 1-μs initial rise time for the loading wave. 93

Figure B-8. Histories of the gap sizes on the centerline at the S-TB interface for two values of the contact parameter VDC and a 1-μs initial rise time for the loading wave. 94

Figure B-9. Histories of the gap sizes on the centerline at the S-IB interface for three values of the contact parameter SFACT and a 25-μs initial rise time for the loading wave. 95

Figure B-10. Histories of the gap sizes on the centerline at the S-TB interface for three values of the contact parameter SFACT and a 25-μs initial rise time for the loading wave. ..96

Figure B-11. Histories of the gap sizes on the centerline at the S-IB interface for two values of the contact parameter VDC and a 25-μs initial rise time for the loading wave. 97

Figure B-12. Histories of the gap sizes on the centerline at the S-TB interface for two values of the contact parameter VDC and a 25-μs initial rise time for the loading wave. 98

Figure C-1. Pressure contours in the vicinity of an annular specimen at 7% axial strain. Any positive pressure (compression) is shaded red; other colors indicate negative (tensile) pressure in units of GPa. The loading wave had a 1-μs initial rise time. Observe the gap along most of the S-IB interface. 102

List of Tables

Table 1. Linear elastic constants for materials used in the numerical simulations. 7
Table 2. Geometric parameters and wave travel times. 9
Table 3. Parameters for the compressible Mooney-Rivlin Model. 15

Acknowledgments

The authors express their appreciation to Bryan Love for performing independent numerical simulations to verify some of the results presented here.

INTENTIONALLY LEFT BLANK.

1. Introduction

The split Hopkinson pressure bar (SHPB), also known as the Kolsky bar, is an experimental technique that is widely used for studying the strain rate sensitivity of inelastic materials in a state of compressive uniaxial stress. The standard relations for analyzing data from SHPB tests rely on the assumption of uniform stress, strain and strain rate throughout the specimen. These conditions, as well as a nearly constant nominal strain rate, can often be achieved after an initial "ringing-up" period. The review articles by Gray (*1*) and Gama et al. (*2*) are recommended for historical background, discussions of experimental procedures and data analysis techniques, and additional references to the literature.

The most common version of the SHPB test assumes that the two pressure bars undergo small strain, linear elastic deformations, that the specimen remains in contact with the pressure bars, and that the faces of the bars in contact with the specimen remain planar. These conditions require that the specimen be softer than the pressure bars. However, difficulties arise in the analysis of the experimental data when the specimen is extremely soft relative to the bars. These difficulties as well as techniques that have been developed to overcome them are discussed in Gray (*1*) and Gama et al. (*2*) and also in Gray and Blumenthal (*3*), Song and Chen (*4*), Moy et al. (*5*), and Song et al. (*6*). One source of difficulty is that the signal in the transmission bar may be too weak to provide accurate measurements of stress in the specimen; this issue is not addressed here. Another difficulty when the imposed axial strain rate is sufficiently high is that the stress and strain within a soft specimen may be non-uniform and the stress state non-uniaxial throughout the test. Such conditions either invalidate the test or at least require appropriate "inertial" corrections to the test data.

The original objective of the present work was to perform numerical simulations on very soft materials in order to test the validity of some approximate, analytical, inertial corrections for SHPB test data. These relations, which were developed by Scheidler (*7*), utilized the simplifying approximation of constant volume and thus are limited to nearly incompressible materials, that is, to materials that are substantially stiffer in dilatation than in shear. Examples of soft, nearly incompressible materials include many types of rubber as well as many biological materials due to their high water content. Ballistic gelatin, which is 80–90% water by mass, also falls into this category; it is widely used as a tissue surrogate in impact and penetration tests.

We performed numerous axisymmetric finite-element simulations of SHPB tests on soft, nearly incompressible materials using the commercial code LS-DYNA (*8*). The initial simulations used a nonlinear elastic model for the specimen, namely, LS-DYNA's compressible version of the Mooney-Rivlin model (*8, 9*). The model was calibrated to give rough agreement with the uniaxial compression data on ballistic gelatin obtained by Moy et al. (*5*) and with the pressure-volume data on ballistic gelatin in Aihaiti and Hemley (*10*). We used a relatively thin specimen

(1.45-mm thickness, 12.7-mm diameter) and a nominal strain rate of 2500/s in all simulations. These were chosen to agree with the test conditions in Moy et al. (*5*). For these initial simulations we used solid (as opposed to annular) specimens.

Much to our surprise, we observed that small gaps formed along both the specimen-incident bar (S-IB) interface and the specimen-transmission bar (S-TB) interface. The size of these gaps ranged from sub-micron to as large as 43 μm, depending on the rise time of the loading wave in the incident bar, the time after the arrival of the wave at the specimen, the particular interface, and the radial location on that interface. The gaps closed and re-opened multiple times, and did not necessarily form over the entire face of the specimen. However, for the S-IB interface and the shortest rise time, a gap existed over most of the face of the specimen for axial strains ranging from 4% to 19%, and out to half of the specimen radius for strains up to 28%.[1] The faces of the pressure bars remained very nearly planar, as expected; the gaps formed as the specimen moved axially inward toward its center. Large pressure spikes were observed on the axis of the bars and the specimen as these gaps closed up and the specimen "slapped" the bars. To the best of our knowledge, this phenomenon has not been reported in either the experimental or the computational literature on SHPB tests,[2] although certain features of previously reported experimental data appear to be consistent with the opening and closing of gaps.

The assumption of contact between the specimen and the bars is implicit in any analysis of the SHPB test, including the inertial corrections that we had intended to validate. Consequently, the focus of our study shifted to the gap phenomenon. In particular, we sought to determine whether the gaps were a numerical artifact. The dependence of gap formation on the following conditions was examined:

1. Constitutive Model for the Specimen:
    a) Model type:
        i) nonlinear elastic (compressible Mooney-Rivlin)
        ii) linear elastic
    b) Model parameters (linear elastic case only)
2. Loading Condition:
    a) Linear ramp (1 or 25 μs) to constant velocity at the far end of the incident bar
    b) Impact of a striker bar on the far end of a long incident bar
    c) Direct impact of a striker bar on the specimen

[1] Gaps at the S-IB interface are clearly visible in figure 13 (solid specimen) and figure C-1 (annular specimen).

[2] However, a summary of some of the results in this report is given the proceedings paper (*11*).

3. Geometry:
    a) Pressure bar diameter
    b) Specimen geometry:
        i) solid
        ii) annular
4. Boundary Condition on the Lateral Surfaces:
    a) Stress-free
    b) Radially constrained
5. Computational Parameters:
    a) Specimen mesh size
    b) Contact algorithm parameters
6. *The code used for the simulations*

The organization of the report can be inferred from the table of contents. Sections 2, 3, 4, 5.1, 5.2, and appendix A contain preliminary and background material. The results of a selected set of numerical simulations are presented in detail in sections 5.3, 6, 7, 8, and appendix B. Appendix C consists of less detailed summaries of simulations for which some of the conditions differed from those in the main body of the report. These conditions are italicized in the list above. In particular, all of the numerical simulations discussed in the main body of this report were performed with LS-DYNA. In appendix C-3, we summarize the results of some analogous simulations performed by Bryan Love at the U.S. Army Research Laboratory (ARL) using the finite element code PRESTO (from Sandia National Laboratories) with loading condition described in 2.b above.

2. Problem Description

2.1 Problem Geometry

The SHPB experiment was modeled using the three parts shown in figure 1, which is not to scale. As indicated in the figure, a cylindrical coordinate system was used with the origin located on the axis of symmetry or centerline of the specimen and the pressure bars at the S-IB interface. The reference or material coordinates (R, Z) are the coordinates in the undeformed state at time $t = 0$; the corresponding coordinates in the deformed state are denoted by (r, z). For axisymmetric deformations, the Z-axis, the z-axis, the set of points with $r = 0$, and the set of points with $R = 0$ all describe the centerline. The positive direction of the Z-axis is along the direction of propagation of the initial loading wave, that is, from incident bar to specimen to

transmission bar. All coordinate values and problem dimensions are given in millimeters, whereas element sizes (section 4.1) and gap sizes are specified in microns.

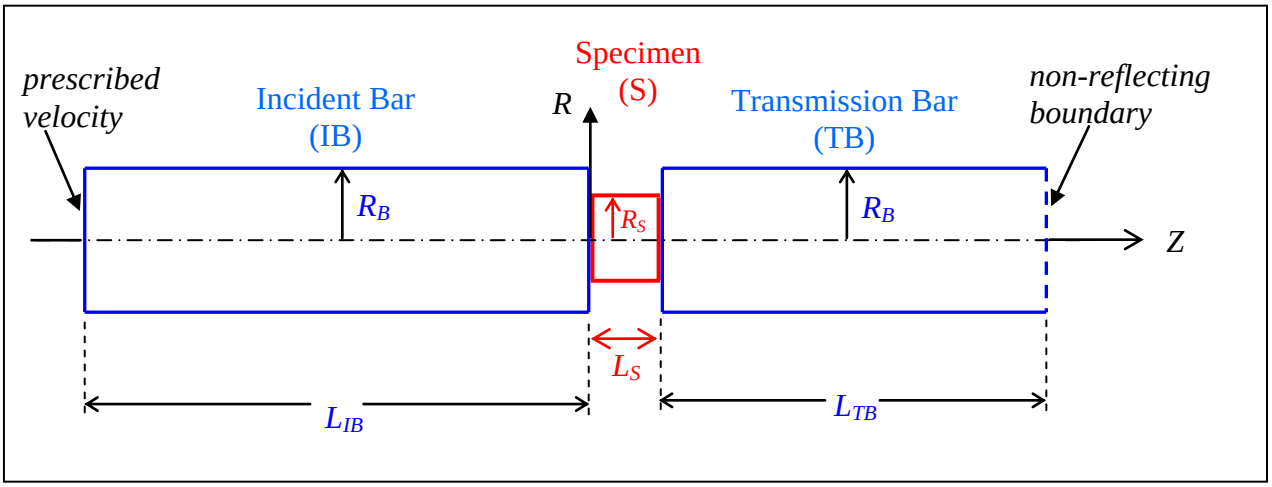

Figure 1. Geometry and coordinate system for the SHPB simulations (not drawn to scale).

A solid, disk-shaped specimen (S) was used for most of the simulations described in this report. A brief summary of simulations involving annular, washer-shaped specimens is given in appendices C-2 and C-3. Unless specified otherwise, a solid specimen is assumed in subsequent discussions. The specimen has initial thickness (or length) $L_S = 1.45$ mm and an initial diameter of 12.7 mm, giving a length-to-diameter ratio of 0.114. Relatively thin specimens are commonly used to decrease the time it takes to "ring-up" to a uniform state.

The incident bar (IB) and the transmission bar (TB) have the same diameter. Two bar diameters were considered, 25.6 mm and 19.0 mm. Most of the simulations were done with the larger bar diameter. Discussion of simulations with the smaller bar diameter is confined to section 6.4 and appendix C-2. The length of the incident bar used in the simulations is $L_{IB} = 768$ mm. This gives a length-to-diameter ratio of 30.0 for the larger diameter bar and 40.4 for the smaller diameter bar. The length of the transmission bar used in the simulations is $L_{TB} = 256$ mm, which is 1/3 the length of the incident bar and gives length-to-diameter ratios of 10.0 and 13.5.

The dimensions of the specimen and the smaller diameter bar were chosen to agree with those used in the experimental study on gelatin by Moy et al. (5). However, we used the larger diameter bar in most of our simulations. This was motivated by our original goal of studying inertial effects at large strains. We wished to obtain nominal axial strains of up to 75% in compression, which corresponds to an axial stretch of 0.25, that is, a specimen compressed to ¼ of its original thickness. This results in a radial stretch of 2.0, assuming incompressibility and a homogeneous deformation. Hence the diameter of the specimen would increase by a factor of 2, that is, from 12.7 to 25.4 mm. And because the deformed specimen must not extend beyond the pressure bars, we chose a diameter of 25.6 mm for the bars.

We will often refer to the specimen and bar radii rather than the diameters. The initial radius of the specimen is $R_S = 6.35$ mm, and the two pressure bar radii considered are $R_B = 12.8$ mm and $R_B = 9.5$ mm.

2.2 Loading and Boundary Conditions

In the simplest version of the SHPB test, a striker bar impacts the incident bar and generates a compressive stress pulse which propagates down the length of the incident bar and subsequently into the specimen and the transmission bar. A direct impact of a striker bar on the incident bar would have been easy to simulate, but it can also be approximated reasonably well by a prescribed step in the axial velocity at the end of the incident bar.

For the purpose of reducing inertial effects in soft specimens, it is beneficial to insert a pulse shaper between the striker and incident bars (*4*–*6*). This is a thin disk of another soft material (generally not the same as the specimen) which serves to smooth the incident pulse and increase its rise time. To avoid the complexity of modeling the pulse shaping material and, in particular, the computational issues associated with the extremely large deformations of the pulse shaper, we chose instead to approximate the effect the pulse shaper on the incident pulse. As in the computational study by Song et al. (*6*), we prescribed an axial velocity, $v_z(t)$, on the impact end of the incident bar. This prescribed velocity has an initial value of zero and rises linearly with time until attaining a plateau value v_0 at time t_R:

$$v_z(t) = \begin{cases} v_0 \cdot \dfrac{t}{t_R} & ; \quad 0 \le t \le t_R \\ v_0 & ; \quad t \ge t_R \end{cases} \tag{1}$$

We set v_0 to 1.8125 m/s in all calculations. This value was chosen to produce a nominal axial strain rate of approximately 2500/s in the specimen, in agreement with the tests in Moy et al. (*5*). We considered two values for the initial rise time t_R, 1 and 25 μs.

In an SHPB test, the lateral surfaces of the pressure bars ($R = R_B$) and the specimen ($R = R_S$) are unconstrained and hence stress-free. The same condition was used in the numerical simulations with two exceptions. For these two exceptional cases (discussed in appendix C-1.1), the lateral surfaces were constrained in order to study the effects of eliminating the unloading waves from these surfaces and reducing the radial acceleration in the specimen.

Friction between the faces of the specimen and the bars can result in bulging of the specimen on compression. In SHPB tests the specimen faces are lubricated to eliminate (or at least substantially reduce) the friction. Consequently, in the numerical simulations the S-IB and S-TB interfaces were modeled with frictionless contact (see section 4.2).

At the far end of the transmission bar, a non-reflecting boundary condition was used; refer to sections 4.2 and 5.2 for further discussion.

2.3 Material Properties

For soft specimens, pressure bar materials with low mechanical impedance are often used to improve the signal to noise ratio (*1–6*). For example, the tests reported in Moy et al. (*5*) and Song et al. (*6*) utilized 7075-T6 aluminum bars. For the imposed velocity history discussed above, the stress in an aluminum bar remains well below yield (see section 5.1). We used an isotropic, linear elastic constitutive model for the incident and transmission bars, with material properties appropriate for aluminum. These properties (obtained from Song et al. [*6*]) are a density of 2.7 g/cm^3, a Young's modulus of 68 GPa, and a Poisson's ratio of 0.33.

As mentioned in the Introduction, we chose ballistic gelatin as a representative soft, nearly incompressible material, and for this we used a compressible version of the classical Mooney-Rivlin constitutive model for incompressible materials. This isotropic, nonlinear elastic constitutive model and its calibration are discussed briefly in section 3 and in more detail in appendix A, and the results of simulations with this model are given in sections 6 and 7 and appendices B and C. At this point we simply note that the density of the specimen was chosen to be that of water, 1 g/cm^3. This same density was also used in subsequent simulations with a linear elastic model for the specimen (see section 8).[3] These simulations were performed to determine whether or not the formation of gaps was attributable to the nonlinearity and/or near incompressibility of the constitutive model. It turned out that gaps formed for all but one of the six sets of material parameters used in the linear elastic model for the specimen.

Table 1 lists the density and linear elastic properties used for the pressure bars and the specimen in the various simulations. For the ballistic gelatin specimen, these parameters represent the small strain, linear elastic approximation to the compressible Mooney-Rivlin model (section 3) and so do not accurately reflect the large strain response. Nevertheless, the table allows one to quickly assess the relative stiffnesses of the materials. E, G, K, and L denote the Young's modulus, shear modulus, bulk modulus, and longitudinal modulus; they govern the response to uniaxial stress, simple shear, pure dilatation, and uniaxial strain, respectively. ν and ρ denote Poisson's ratio and the initial density. Since all the materials are isotropic, any two of the material parameters E, G, K, L, and ν determine the other three. For example,

$$K = \frac{2}{3}\frac{1+\nu}{1-2\nu}G \qquad \text{and} \qquad L = \frac{1-\nu}{(1+\nu)(1-2\nu)}E = K + \frac{4}{3}G\,. \tag{2}$$

[3] However, the linear elastic constants used in these simulations are not necessarily those appropriate for the small strain response of ballistic gelatin.

Table 1. Linear elastic constants for materials used in the numerical simulations.

Material	**Density (g/cm^3)**	**Elastic Moduli (GPa)**				**Dimensionless Elastic Constants**		**Wave Speeds (mm/μs)**			**Impedance Ratios (specimen/bar)**	
	ρ	E	G	K	L	ν	G/K	c_L	c_E	c_G	**Based on c_L**	**Based on c_E**
Aluminum Bars	2.70	68.0	25.6	66.7	101.	0.33	0.383	6.11	5.02	3.08	×	×
Ballistic Gelatin Specimen	1.00	2.40×10^{-4}	8.00×10^{-5}	4.00	4.00	0.49999	2.00×10^{-5}	2.00	0.0155	0.00894	0.121	0.00114
Linear Elastic Specimen	1.00	4.30×10^{-4}	1.43×10^{-4}	7.17	7.17	0.49999	2.00×10^{-5}	2.68	0.0207	0.0120	0.162	0.00153
				0.717	0.717	0.49990	2.00×10^{-4}	0.847			0.0513	
				0.143	0.144	0.49950	0.00100	0.379			0.0230	
				0.0717	0.0719	0.49900	0.00200	0.268			0.0163	
			1.44×10^{-4}	0.00717	0.00736	0.49000	0.0201	0.0858			0.00520	
			1.45×10^{-4}	0.00358	0.00378	0.48000	0.0405	0.0615		0.0121	0.00373	

These and other relations between the moduli and Poisson's ratio may be found in most textbooks on elasticity or elastic wave propagation. It is clear from table 1 that the aluminum pressure bars are substantially stiffer than the specimen materials. This is particularly true in shear. The shear modulus of the specimen materials is 4–5 orders of magnitude smaller than the shear modulus of the bars.

The dimensionless parameter *G/K*, the ratio of the shear to the bulk modulus, is a measure of the incompressibility of the material. It is a strictly decreasing function of Poisson's ratio ν and approaches zero as ν and approaches ½ from below, as follows from equation 2_1. Materials for which $G/K \leq 0.01$ are typically referred to as *nearly incompressible*. From equation 2_1, we find that this condition is equivalent to $\nu \geq 0.495$.[4] Note that for the specimen, all cases but the last two in table 1 satisfy this condition. For nearly incompressible materials, volumetric and shear strains of the same magnitude will generate a pressure that is several orders of magnitude larger than the shear stress; conversely, pressure and shear stresses of the same magnitude will generate a volumetric strain that is several orders of magnitude smaller than the shear strain.

2.4 Wave Speeds and Travel Times

Table 1 also lists three different linear elastic wave speeds for each material: the longitudinal wave speed[5] c_L, the shear wave speed c_G, and the "bar wave speed" c_E (see section 5.1) The subscript indicates which elastic modulus is used to compute the wave speed from the relation $c_M = \sqrt{M / \rho}$, where *M* denotes one of the moduli *L*, *G*, or *E*. The table does not list the Rayleigh wave speeds, which govern the propagation of surface waves. For all the specimen materials considered here, the Rayleigh wave speed is about 95% of the corresponding shear wave speed; for the aluminum bars, it is about 93% of the shear wave speed.[6]

The mechanical impedances corresponding to the longitudinal modulus and the Young's modulus are ρc_L and ρc_E, respectively. The ratio of specimen impedance to bar impedance governs the transmission and reflection of the loading wave. Table 1 lists the values of this ratio. In the one-dimensional theory of wave propagation the different cross-sectional areas of the specimen and the bar would also be taken into account, and in such analyses the impedances based on the "bar speed" (i.e., ρc_E) are typically used. However, at early times after the arrival of the loading wave, the specimen deformation is far from one-dimensional and the longitudinal wave speed c_L is more relevant, particularly in the interior of the specimen and the bars.

Table 2 summarizes the geometric parameters of the problem and also gives the corresponding wave travel times based on the wave speeds in table 1. The travel times (in μs) are listed in two groups: the time for a wave to travel the length of the bar or the specimen, and the time for a

---

[4] Some authors use the less restrictive condition $\nu \geq 0.49$ as the criterion for near incompressibility; this is equivalent to the condition $G/K \leq 0.02$.

[5] This is also referred to as the dilatational wave speed.

[6] See table 7.5.1 in Eringen and Suhubi (*12*).

wave to travel the radius of the bar or the specimen. Of course, these travel times depend on the type of wave under consideration. Travel times for the lengths are given for the longitudinal, shear, and bar waves. Travel times for the radius are given for the longitudinal and shear waves only, since the bar wave speed is not relevant in this case.

Table 2. Geometric parameters and wave travel times.

Material	**Length (mm)**	**Travel Times (μs)**			**Radius (mm)**	**Travel Times (μs)**	
		Based on c_L	**Based on c_E**	**Based on c_G**		**Based on c_L**	**Based on c_G**
Incident Bar	768.0	125.7	153.0	249.6	12.8	2.10	4.16
	768.0	125.7	153.0	249.6	9.5	1.56	3.09
Transmission Bar	256.0	41.9	51.0	83.2	12.8	2.10	4.16
	256.0	41.9	51.0	83.2	9.5	1.56	3.09
Ballistic Gelatin Specimen	1.45	0.72	93.60	162.1	6.35	3.17	710.0
Linear Elastic Specimen $\nu = 0.49999$	1.45	0.54	69.93	121.1	6.35	2.37	530.4
$\nu = 0.49990$		1.71		121.1		7.50	530.4
$\nu = 0.49950$		3.83		121.1		16.76	530.3
$\nu = 0.49900$		5.41		121.1		23.69	530.2
$\nu = 0.49000$		16.91		120.7		74.02	528.6
$\nu = 0.4800$		23.59		120.3		103.3	526.6

The wave speeds listed in tables 1 and 2 for the Mooney-Rivlin model for the specimen are only approximate since they are based on the linear elastic approximation to a nonlinear constitutive model. The wave speeds, and hence the impedance ratios and travel times, will change with the deformation. Also, since the specimen undergoes large deformations (for both the nonlinear and linear elastic models), and since the travel times are based on the undeformed lengths, these times are only approximate for the deformed specimen. Nevertheless, the tabulated values

provide an order of magnitude estimate for the wave speeds and travel times in the specimen. These estimates for the wave travel times are useful for determining whether certain features of the specimen response (to be discussed later) correlate with the arrival of certain waves.

2.5 Measurement of Gap Size

Many of the figures in this report give (for one or both interfaces) the gap size as a function of time on the centerline or the gap size as a function of radius at fixed times. In this section, we specify the convention used in measuring these gaps. We begin by restricting attention to the centerline.

Material points initially on the centerline must remain on the centerline, that is, $r = 0$ if and only if $R = 0$. Hence, the radial displacement of points on the centerline is zero. The axial displacements of the specimen and the incident bar at their interface ($Z = 0$) on the centerline are denoted by $u_{\text{S-IB}}$ and u_{IB}, respectively; similarly, $z_{\text{S-IB}}$ and z_{IB} denote the corresponding deformed axial coordinates. Since the specimen and the bar are initially in contact, they will continue to be in contact at some later time t if and only if their axial displacements coincide at time t or, equivalently, their deformed axial coordinates coincide at time t. If the specimen and the incident bar separate, that is, if a gap forms between them, then the size of this gap, $\Delta_{\text{S-IB}}$, is given by the difference in their displacements or, equivalently, by the difference in their deformed axial coordinates:

$$\Delta_{\text{S-IB}} = u_{\text{S-IB}} - u_{\text{IB}} = z_{\text{S-IB}} - z_{\text{IB}} \,. \tag{3}$$

Similarly, the axial displacements of the transmission bar and the specimen at their interface ($Z = L_{\text{S}} = 1.45$) on the centerline are denoted by u_{TB} and $u_{\text{S-TB}}$, respectively; and z_{TB} and $z_{\text{S-TB}}$ denote the corresponding deformed axial coordinates. If the specimen and the transmission bar separate, then the size of the gap between them, $\Delta_{\text{S-TB}}$, is given by the difference in their displacements or, equivalently, by the difference in their deformed axial coordinates:

$$\Delta_{\text{S-TB}} = u_{\text{TB}} - u_{\text{S-TB}} = z_{\text{TB}} - z_{\text{S-TB}} \,. \tag{4}$$

As will be seen in subsequent figures, when gaps do form it is the result of the specimen moving away from the bars, so that for the coordinate system in figure 1, $u_{\text{S-IB}} > u_{\text{IB}}$ for a gap at the incident bar, and $u_{\text{S-TB}} < u_{\text{TB}}$ for a gap at the transmission bar. The definitions of the gap sizes given above were chosen so that the sign of the gap would be positive in these cases; of course, a value of zero for the gap implies that the specimen and bar are in contact.

If, as above, we restrict attention to the centerline, then the gap sizes are a function of time only. The majority of our plots of gap size are for this case. However, we have also included a few plots of gap size versus radial location at selected times. For this case it makes a difference whether the axial displacements are referred to points on the specimen and bar with the same initial radius R or to points on the specimen and bar with the same deformed radius r. The latter case, that is, the axial separation of the specimen and bar along a line of constant radius in the

deformed state, is of more interest and is used here. With this caveat, the definitions above still apply.[7]

2.6 Stress, Stretch and Strain

When the specimen remains in contact with the bars, the deformed thickness (or length) of the specimen, ℓ_S, is determined either from the current positions of its faces or from its initial length L_S and the current displacements of its faces:

$$\ell_S = z_{TB} - z_{IB} = L_S + u_{TB} - u_{IB} \,. \tag{5}$$

These variables may be measured at any radial location since the faces of the bars remain very nearly planar when the specimen is relatively soft, as in the cases considered here. At radial locations where there are substantial gaps between the specimen and the bars, equation 5 will overestimate the deformed thickness.

The term *stretch* denotes the local ratio of deformed to undeformed length, which, of course, varies with direction. The stretch in all directions is unity in the undeformed state. A stretch greater than 1 corresponds to extension in the given direction; a stretch between 0 and 1 corresponds to compression. The stretches in the radial, hoop and axial directions are denoted by λ_r, λ_θ and λ_z, respectively. They are the diagonal components of the deformation gradient tensor $\boldsymbol{F}$ and are given by the relations

$$\lambda_r = \frac{\partial r}{\partial R}, \quad \lambda_\theta = \frac{r}{R}, \quad \lambda_z = \frac{\partial z}{\partial Z} \,. \tag{6}$$

We are primarily interested in the stretches and strains in the specimen and, in particular, in the axial stretch and corresponding axial strain. The nominal (or engineering) strain e_z and the logarithmic (or true) strain ε_z in the axial direction are given by

$$e_z = 1 - \lambda_z \,, \qquad \varepsilon_z = -\ln \lambda_z \,. \tag{7}$$

Both of these strain measures are used in the experimental literature for reporting SHBP test data. The radial and hoop strains are defined similarly. Note that these strain measures have been taken positive if the particular coordinate direction is in compression. In the general continuum mechanics literature, the sign convention for strain is "positive in extension" and "negative in compression". However, in the SHPB literature the opposite convention is typically used since the specimen is under axial compression; we have followed that convention here.

The average or mean value of the axial stretch in the specimen is the ratio of the deformed to undeformed thickness:

---

[7] The deformed axial coordinates are computed at element nodes. The specimen and bar nodes off the centerline do not necessarily line up. For a specimen node with deformed radius r, we used linear interpolation between the two incident bar nodes whose deformed radius bounded r in order to determine $z_{IB}(r)$; similarly for the transmission bar.

$$\lambda_z = \frac{l_S}{L_S} = 1 + \frac{u_{TB} - u_{IB}}{L_S}, \tag{8}$$

where the relation on the right follows from equation 5. The mean value of the nominal axial strain[8] is given by

$$e_z = 1 - \lambda_z = 1 - \frac{l_S}{L_S} = \frac{u_{IB} - u_{TB}}{L_S}. \tag{9}$$

Note that we use the same notation for local and mean values; it should be clear from the context which meaning is intended.

We use a superposed dot to denote the material time derivative. It follows from equation 9 that the mean value of the nominal axial strain rate is given by

$$\dot{e}_z = -\dot{\lambda}_z = \frac{v_{IB} - v_{TB}}{L_S} \approx \frac{v_{IB}}{L_S}, \tag{10}$$

where v_{IB} and v_{TB} denote the axial component of velocity of the incident and transmission bars at the specimen interfaces. The approximation on the right follows from the fact that for soft specimens, v_{IB} will generally be much larger than v_{TB}.[9] This approximate relation yields an even cruder approximation for the "strain acceleration": $\ddot{e}_z = -\ddot{\lambda}_z \approx \dot{v}_{IB} / L_S$. For the imposed velocity history at the far end of the incident bar, as described in equation 1, v_{IB} eventually oscillates around a mean value of roughly twice v_0 (see section 5.3).

Note that it is the mean values of axial strain and axial strain rate that are actually measured[10] in an SHPB test. Similarly, the values of the axial stretch given in our figures are the mean values computed from equation 8; consequently, the corresponding nominal axial strains cited in subsequent discussions are the mean values determined from equation 9. These mean values may differ substantially from the local values if the specimen deformation is highly non-uniform. This will certainly be the case during the "ring-up" period when wave propagation dominates. Also, at radial locations where there are substantial gaps between the specimen and the bars, the relation 8 will overestimate the axial stretch, and consequently, the relation 9 will underestimate the axial strain. Likewise, the relations for the mean value of the nominal axial strain rate in equation 10 will not be valid when a gap forms.

The Cauchy stress tensor is denoted by $\boldsymbol{\sigma}$. Its components, which give force per unit deformed area, are often referred to as *true* stresses. We follow the sign convention in the general

[8] A mean value of the logarithmic axial strain is provided by equation 7_2 with λ_z given by equation 8.

[9] The displacement histories at the S-IB and S-TB interfaces in figures 7 and 8 are consistent with this assertion.

[10] More precisely, they are inferred from strain gage measurements in the pressure bars.

continuum mechanics literature, that is, the stress components are taken positive in tension and negative in compression,[11] whereas the pressure p is taken to be positive in compression:

$$p = -\frac{1}{3}\operatorname{tr}\boldsymbol{\sigma} = -\frac{1}{3}\left(\sigma_{rr} + \sigma_{\theta\theta} + \sigma_{zz}\right). \tag{11}$$

Here, "tr" denotes the trace, and σ_{rr}, $\sigma_{\theta\theta}$, and σ_{zz} are the radial, hoop and axial components of $\boldsymbol{\sigma}$. Since axisymmetric deformations are imposed and the constitutive models for all materials are isotropic,

$$\sigma_{\theta z} = \sigma_{z\theta} = \sigma_{r\theta} = \sigma_{\theta r} = 0. \tag{12}$$

However, the shear stress component $\sigma_{rz} = \sigma_{zr}$ need not be zero in general; in particular, σ_{rz} will be nonzero in the specimen whenever there is bulging.

Since only isotropic elastic constitutive relations are used here, the principal axes of stress and strain coincide. The θ (i.e., hoop) direction is always a principal axis of stress and strain for axisymmetric deformations, but the r and z (i.e., radial and axial) directions will be principal axes if and only if the shear stress σ_{rz} is zero. In this case, the radial, hoop and axial stretches are the principal stretches, and the Jacobian[12] of the deformation, J, is given by

$$J = \lambda_r \lambda_\theta \lambda_z. \tag{13}$$

There are two situations where the condition $\sigma_{rz} = 0$, the relation 13, and the relations

$$\sigma_{rr} = \sigma_{\theta\theta}\,, \quad e_r = e_\theta\,, \quad \lambda_r = \lambda_\theta = \frac{J}{\sqrt{\lambda_z}}\,, \tag{14}$$

can be guaranteed to hold exactly. One of these occurs when the deformation is uniform, which is the desired state in an SHPB test. The other occurs at any point on the centerline of a solid specimen, regardless of whether or not the deformation is uniform.[13] Furthermore, for the nearly incompressible specimen materials considered here, J will generally be close to one even for large deformations, in which case equation 14_3 yields the approximation

$$\lambda_r = \lambda_\theta \approx \frac{1}{\sqrt{\lambda_z}} \tag{15}$$

---

[11] This is also the sign convention used in LS-DYNA. However, in the SHPB literature it is more common to take stress positive in compression, since the specimen is under axial compression during the useful part of the test.

[12] This is the determinant of the deformation gradient $\boldsymbol{F}$ and represents the local ratio of deformed to undeformed volume.

[13] That $\sigma_{rr} = \sigma_{\theta\theta}$ and $\sigma_{rz} = 0$ on the centerline follow from the radial and axial components, respectively, of the momentum balance equation, after multiplying by r and taking the limit as r approaches zero. That $\lambda_r = \lambda_\theta$ on the centerline follows from equations 6, since r/R approaches $\partial r/\partial R$ as R and r approach zero. Also, both $\partial r/\partial Z$ and $\partial z/\partial R$ must be zero on the centerline to prohibit singularities.

on the centerline. When the deformation in the specimen is non-uniform, the relations 13-15 will hold approximately at points near the centerline, and they may even hold approximately at points substantially off the centerline.

3. The Mooney-Rivlin Constitutive Model for the Specimen

3.1 Incompressible and Compressible Versions

The classical Mooney-Rivlin model is a nonlinear elastic constitutive model for isotropic, incompressible solids. It is one of the earliest models of this type, and was originally applied to the response of rubber under large deformations; see the original papers by Mooney (*13*) and Rivlin (*14*) and the book by Treloar (*15*). Because of its simplicity, the model is widely used in theoretical studies and is often applied to nearly incompressible materials other than rubber. The Mooney-Rivlin model is discussed in many textbooks on nonlinear elasticity and continuum mechanics; see (*16–19*). A description of the model is provided in appendix A-2.

The incompressibility assumption is, of course, an idealization. For quasi-static problems with at least one free surface, the assumption of incompressibility typically yields reasonable results if the bulk modulus is at least two orders of magnitude larger than the shear modulus. However, the incompressibility constraint is inconsistent with the propagation of longitudinal waves, so for dynamic problems involving nearly incompressible materials, some degree of compressibility must be added to the constitutive model.

The simulations described in sections 6 and 7 and in appendices B and C used LS-DYNA's compressible version of the Mooney-Rivlin model for the specimen; this is Material Type 27 in the manuals (*8, 9*). The model has three material constants (aside from the density): the elastic moduli[14] A_1 and A_2, and the Poisson's ratio ν. The two moduli characterize the response to volume-preserving deformations (just as in the incompressible version), whereas the nonlinear pressure-volume relation involves all three constants. We refer to this as the "compressible Mooney-Rivlin model"; it is discussed in more detail in appendix A-3. Verification of the model implementation is discussed in appendix A-4. For the purposes of the present discussion, we simply note that the shear modulus G in the small strain, linear elastic approximation to the model is related to the moduli A_1 and A_2 by

$$G = 2(A_1 + A_2) \, . \tag{16}$$

Since the linear elastic bulk modulus K is given in terms of the shear modulus and Poisson's ratio by equation 2_1, ν can be adjusted so as to yield the bulk modulus for the material in question, once A_1 and A_2 (and hence G) have been determined. For the nearly incompressible materials of interest here, this means choosing ν very close to ½.

[14] The LS-DYNA manuals (*8, 9*) use the symbols A and B for the constants A_1 and A_2, respectively.

3.2 Calibration of the Mooney-Rivlin Model for Ballistic Gelatin

Ballistic gelatin is a prime example of a soft, nearly incompressible material. Gelatin powder is an aggregate of large protein molecules (collagen) of various sizes, extracted from animal tissues (*20*). In this report, the term *gelatin* refers to the solution of this powder in water. The common formulations of ballistic gelatin are 20% and 10% powder by mass (80% and 90% water by mass). Both formulations are used as tissue surrogates in impact and penetration tests.

LS-DYNA's compressible Mooney-Rivlin model was calibrated to yield a response typical of 20% ballistic gelatin. The parameters A_1 and A_2 listed in table 3 were chosen to give rough agreement with quasi-static uniaxial compression data on ballistic gelatin obtained in an experimental study by Moy et al. (*5*). More precisely, these values give a stress-strain curve that lies slightly above their curve for a strain rate of 1/s.[15] This represents a rough extrapolation of their quasi-static data (strain rates of 0.001/s, 0.01/s, 1/s) to strain rates on the order of 2500/s.[16] By equation 16, the corresponding small strain shear modulus is G = 80 kPa. Substantially lower values for these moduli would be expected for 10% gelatin.

Table 3. Parameters for the compressible Mooney-Rivlin Model.

ρ (g/cm^3)	A_1 (kPa)	A_2 (kPa)	ν
1.00	12.0	28.0	0.49999

Since gelatin is mostly water, one would expect its density and (initial) bulk modulus to be close to that of water, namely, 1 g/cm^3 and 2.3 GPa, respectively. The room temperature densities for 20% gelatin reported in Aihaiti and Hemley (*10*) and Winter and Shifler (*20*) are about 1.00 g/cm^3 and 1.06 g/cm^3, respectively.[17] We used the value 1.00 g/cm^3. However, the estimated bulk modulus for 20% ballistic gelatin in Aihaiti and Hemley (*10*) is more than twice that of water.[18] We chose a Poisson's ratio of ν = 0.49999, which together with the shear modulus of 80 kPa (calculated above) yields a bulk modulus of K = 4.0 GPa. Note that this is more than five orders of magnitude larger than the shear modulus.

---

[15] The corresponding stress-stretch curve is plotted in figure A-1 in our appendix A-4. As discussed their, these curves are largely insensitive the value of ν, provided that it is close to ½.

[16] This extrapolated curve lies well below their stress-strain curve at a strain rate of 2500/s, obtained in an SHPB test on an annular specimen. We believe that there are large inertial effects in that test and, in particular, that the stress state is not uniaxial and so not comparable with the quasi-static data. The quasi-static data referred to here was provided by Tusit Weerasooriya of ARL. This data is not included in (*5*), except for the upper stress-strain curve in figure 6(a) in that report, which is described there as corresponding to a strain rate of 1/s but which appears to be the 0.001/s curve in the data provided to us.

[17] The value 1.00 g/cm^3 is based on a slight extrapolation of the data given in Aihaiti and Hemley (*10*); the authors attribute this data to Dana Dattlebaum at Los Alamos National Laboratory (LANL).

[18] The value reported in Aihaiti and Hemley (*10*) varied from about 4.6 to 5.2 GPa at room temperature, depending on the functional form of the equations used to fit the data. However, it appears that even the lowest of these values may be too high. After are computational study was completed, we were informed that the data in Aihaiti and Hemley (*10*) is inconsistent with the shock Hugoniot data from LANL, and that the latter implies an initial bulk modulus much closer to that of water (*21*).

We emphasize that our intention in this study was neither to develop a constitutive model for ballistic gelatin nor to simulate a particular SHPB experiment on gelatin. Ballistic gelatin is known to exhibit viscoelastic behavior. The rate-dependence of the large strain compression data in (*5*) and elsewhere is consistent with this, as is the small strain rheometer data in Juliano et al. (*22*). An accurate model for ballistic gelatin would require the addition of a viscoelastic component to the constitutive model. Consequently, numerical simulations capable of duplicating high-rate SHPB experiments would likely require a properly calibrated nonlinear viscoelastic model. The use of a purely elastic model was motivated by our original objective of quantifying inertial effects in SHPB tests. Since there are no strain rate effects in an elastic model, any differences observed between quasi-static and high-rate uniaxial compression tests must be due to inertial effects in the latter.

4. Computational Parameters

4.1 Geometry and Meshing

The meshes for the specimen and pressure bars consisted of 4-node quadrilateral elements used in 2-D axisymmetric mode. Single-point integration was used throughout. Three different meshes were used for the specimen, as shown in figure 2. Since the axial strain in the specimen is approximately twice the radial strain, it was beneficial to use specimen elements whose initial length in the axial direction was twice that in the radial direction, so that the element became more nearly square under severe axial compression. The default or baseline mesh is shown in figure 2a and referred to as the "25×50 μm mesh": all specimen elements had a radial edge length of 25 μm and an axial edge length of 50 μm. This specimen mesh was used in all simulations with the exception of the mesh sensitivity study discussed in appendix B-1, where the results for the baseline mesh are compared with the results for a coarser mesh (50×100 μm in figure 2b) and a finer mesh (12.3×12.5 μm in figure 2c)

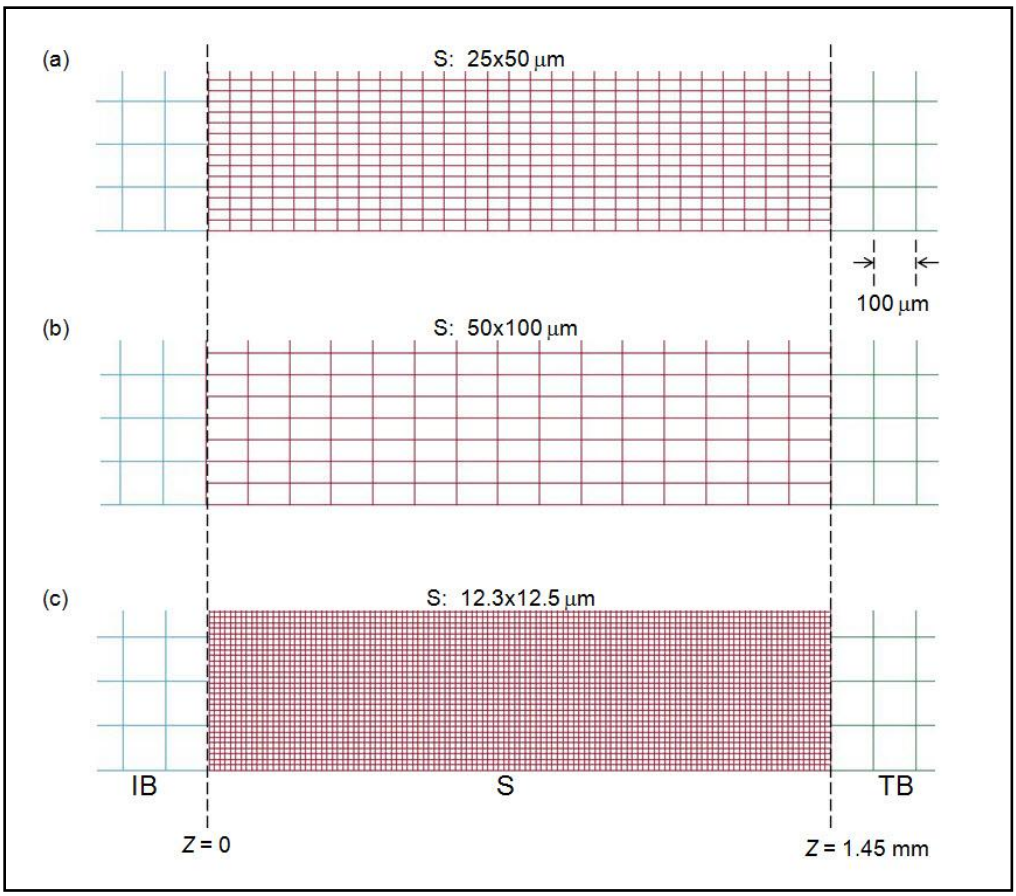

Figure 2. Meshes for the Incident Bar (IB), Transmission Bar (TB), and Specimen (S). The baseline mesh for the specimen is shown in case (a).

All incident bar and transmission bar elements were squares with a 100-μm edge length. Differences between bar and specimen element sizes in the axial direction could result in a computational impedance mismatch if the specimen and bars had similar mechanical impedances. This was not an issue here since the specimen and bar impedances were already quite dissimilar (see table 1). Also, since the faces of the stiffer bars are expected to remain nearly flat, elements with larger radial edge length could be tolerated. The element size in the bars does need to be small enough to capture the essential features of the wave propagation (see section 5). The 100-μm edge length seemed to be sufficient for this.

4.2 Boundary Conditions

The interaction of the specimen and the bars at the S-IB interface and the S-TB interface was governed by the LS-DYNA segment-based penalty algorithm CONTACT_2D with the option AUTOMATIC_SURFACE_TO_SURFACE (*8, 9*). This algorithm requires three input parameters: SFACT, a scale factor for the penalty force stiffness; VDC, a viscous damping coefficient (in percent of the level for critical damping); and a Coulomb friction coefficient, which was set to zero for frictionless contact (see section 2.2). The LS-DYNA default values

SFAC = 1 and VDC = 10 were used for all simulations with the exception of the contact algorithm parameter sensitivity study in appendix B-2.

As discussed in section 2.2, the boundary condition at the impact end of the incident bar is a prescribed axial velocity history. No radial constraint was placed on the nodes there.

At the far end of the transmission bar, we used the LS-DYNA non-reflecting boundary condition BOUNDARY_NON_REFLECTING_2D (*8, 9*) to simulate a semi-infinite transmission bar. This algorithm imposes normal and shearing stresses given by

$$\sigma_{\text{normal}} = -\rho c_L \mathrm{v}_{\text{normal}}, \qquad \sigma_{\text{shear}} = -\rho c_G \mathrm{v}_{\text{tangential}}. \tag{17}$$

Here c_L and c_G are the longitudinal and shear wave speeds, respectively, of the transmitting material (in our case aluminum), and $\mathrm{v}_{\text{normal}}$ and $\mathrm{v}_{\text{tangential}}$ are the particle velocities in the normal and tangential direction, respectively. We conducted some preliminary tests on this boundary condition and found that it performed extremely well in one-dimensional uniaxial strain, and reasonably well for waves of the type generated in our simulations. Once the loading wave travels through the specimen and reaches the transmission bar, it takes about 42 μs for a longitudinal wave and 51 μs for the bar wave to travel the length of the transmission bar (see table 2), and then another 42–51 μs for any slight reflections from the supposedly non-reflecting boundary to arrive back at the specimen. Thus any influence that slight reflections from the far end of the transmission bar might have on the interactions at the S-TB interface could not possibly be felt earlier than 84–102 μs after the loading wave first reached that interface.

4.3 Miscellaneous

The default values, 1.5 and 0.06, were used for the quadratic and linear artificial viscosity coefficients, respectively. The time step factor of safety, TSSFAC, was set to 0.1, meaning that the time step computed using the Courant condition is then multiplied by 0.1.

LS-DYNA's Orthotropic Elastic model (Material Model 2 in LS-DYNA [*8*] and Hallquist [*9*]) was used for the pressure bars. The material constants for this orthotropic, linear elastic model were chosen in such a way as to yield an isotropic, linear elastic model. Values of the material constants appropriate for aluminum were used in all the simulations and are given in table 1.

5. Wave Propagation in the Pressure Bars

5.1 General Remarks

The loading wave in the incident bar generates an axial stress on the order of $\rho c_E \mathrm{v}_0$, where v_0 is the plateau of the imposed velocity at the impact end, as described in equation 1. For the value $\mathrm{v}_0 = 1.8125$ m/s used in our simulations this gives an axial stress on the order of 25 MPa for

aluminum, which is well below the dynamic yield stress.[19] This justifies the use of a linear elastic model for the pressure bars in our simulations. Linear elastic deformation of the bars is also a requirement in actual SHPB tests, since the analysis of test data is based on linear elastic wave propagation theory (*1*, *2*).

A good reference for linear elastic wave propagation in bars is Chapters 2 and 8 in Graff (*24*); see also Eringen and Suhubi (*12*). The one-dimensional theory of wave propagation in long bars predicts that a longitudinal elastic wave travels undistorted at the "bar speed" c_E, that is, at the speed governed by the Young's modulus E. The more accurate results of the three-dimensional theory are much more complex, particularly near the loading end where the wave becomes highly distorted with large oscillations. These oscillations decay somewhat as the wave progresses down the bar, but they do not go away entirely. Near the centerline of the bar the wave initially propagates at the longitudinal elastic wave speed c_L. But release waves from the stress-free lateral surface interact with the longitudinal wave, so that by the time the wave has traveled 10–20-bar diameters only a trace of the initial longitudinal wave remains. Most of the energy is contained in a wave moving at the slower bar speed c_E. Due to wave dispersion, the rise time of the loading pulse increases as it moves down the bar and the axial stress, strain and particle velocity oscillate about the value predicted by the one-dimensional theory.

According to table 2, for the material properties and incident bar length considered here, the longitudinal and bar waves should take about 126 and 153 μs, respectively, to arrive at the specimen. The average of these arrival times is about 140 μs. As will be seen in section 5.3, the velocity histories in the incident bar in the simulations are consistent with the preceding observations.

5.2 Considerations Governing the Bar Lengths

In an SHPB experiment the length of the striker bar determines the duration of the loading pulse, which in turn determines the duration of the test. The length of the incident bar is determined by the requirement that the incident and reflected pulses measured by a strain gage mounted midway down the bar must not overlap. As a result, incident bar lengths of several meters are commonly used.

In order to reduce the size of the output files and particularly the run times of the simulations, we did not wish to model the full length of a real incident bar. Indeed, there was no need to do so, as the prescribed velocity history (equation 1) is not a pulse but instead has essentially infinite duration, and there is no strain gage to consider. Nevertheless, two considerations govern the minimum length required for the incident bar in our numerical simulations. First, a bar of length at least 20 diameters is desirable in order to simulate the effects of dispersion on the loading wave. Second, in the simulations the total strain that can be imposed on the specimen is proportional to the length of incident bar. To see this, note that the compressive incident wave

[19] The value of the Hugoniot elastic limit for 7075-T6 aluminum listed in Steinberg (*23*) is 420 MPa.

reflects from the lower impedance specimen as a tensile wave, travels back down the bar, reflects from the loading end as tensile wave,[20] and eventually arrives back at the specimen, after which time the simulation is no longer useful. The time for this round trip is thus twice the time to travel one length of the bar, and this time window limits the total strain that can be imposed on the specimen.

We chose an incident bar length of L_{IB} = 768 mm, which gives a length-to-diameter ratio of 30.0 for the larger diameter bar and a time window of roughly 2×140 μs = 280 μs, which suffices for large strains in the specimen. Since the incident wave arrives at the specimen at about t = 140 μs, specimen loading would occur from about t = 140 μs to t = 420 μs. However, when gaps formed (as they did in most of our simulations), they developed shortly after the arrival of the incident wave. And since this became the focus of our study, we terminated most of the simulations at 340 μs. Thus most of our time history plots are restricted to the 200-μs time window from t = 140 μs to t = 340 μs.

As discussed at the end of section 4.2, slight reflections from the supposedly non-reflecting boundary at the far end of the transmission bar could not possibly be felt at the S-TB interface earlier than 84–102 μs after the loading wave first reaches that interface. Using t = 140 μs for the latter arrival time,[21] we see that the effects of any deficiencies in the non-reflecting boundary condition cannot be felt earlier than about t = 230 μs. As will be seen below, gaps formed at the S-TB interface well before this time, although we cannot rule out the possibility of some influence at later times.

5.3 Velocity Histories in the Incident Bar

Figures 3–6 are plots of the time history of the axial component of the particle velocity, v_z, at four locations on the centerline of the incident bar ($r = R = 0$). The velocity is scaled by the plateau value (v_0 = 1.8125 m/s) of the input velocity. All plots are for the bar with the larger radius (R_B = 12.8 mm), although the results for the smaller radius should be similar.

Figures 3 and 4 give velocity histories at the loading end ($Z = -L_{IB}$), 1/3 of the way from the loading end ($Z = -0.666\ L_{IB}$), and 2/3 of the way from the loading end ($Z = -0.333\ L_{IB}$). On these two plots the time is scaled by the transit time of a longitudinal wave along the length of the bar, which is L_{IB} / c_L^{Al} = 125.7 μs, where c_L^{Al} is the longitudinal wave speed of aluminum.

Figure 3 is for an initial rise time t_R of 1 μs, which is too short for the linear ramp to be distinguishable on the time scale of this plot. Figure 4 is for the 25-μs initial rise time; in this case the linear ramp is clearly distinguishable. For both cases, the velocity at the two interior locations oscillates about the plateau value v_0.

---

[20] The fixed velocity boundary condition at the loading end produces the same effect on the stress wave as a rigid boundary would, that is, a tensile wave is reflected as a tensile wave. Indeed, relative to an observer moving with the imposed velocity v_0, that boundary would appear rigid.

[21] Note that the travel time through the specimen is less than 1 μs for the Mooney-Rivlin model as well as for the linear elastic model with ν = 0.49999 (see table 2).

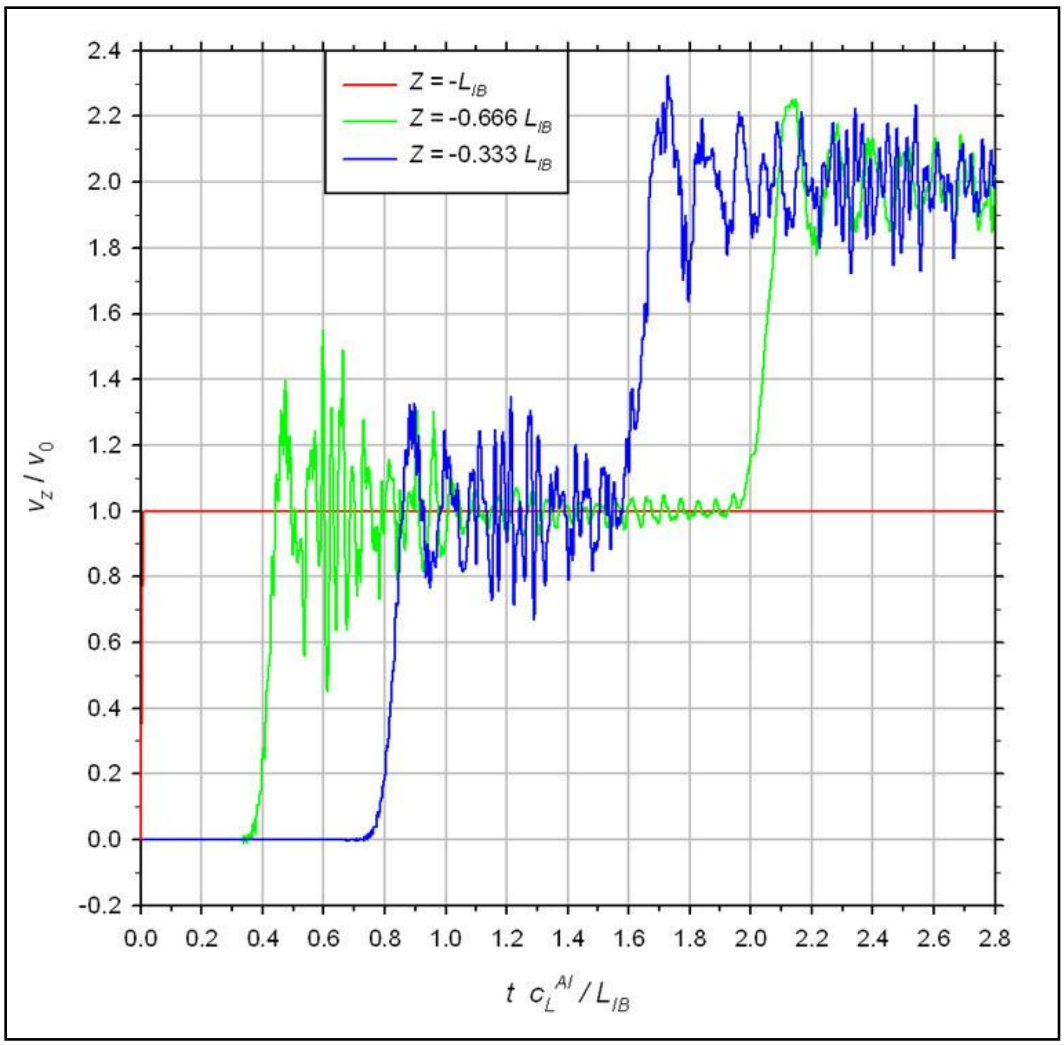

Figure 3. The scaled axial velocity vs. non-dimensional time at three locations on the centerline of the incident bar: the loading end with a 1-μs rise time, 1/3 of the way from the loading end, and 2/3 of the way from the loading end (blue curve).

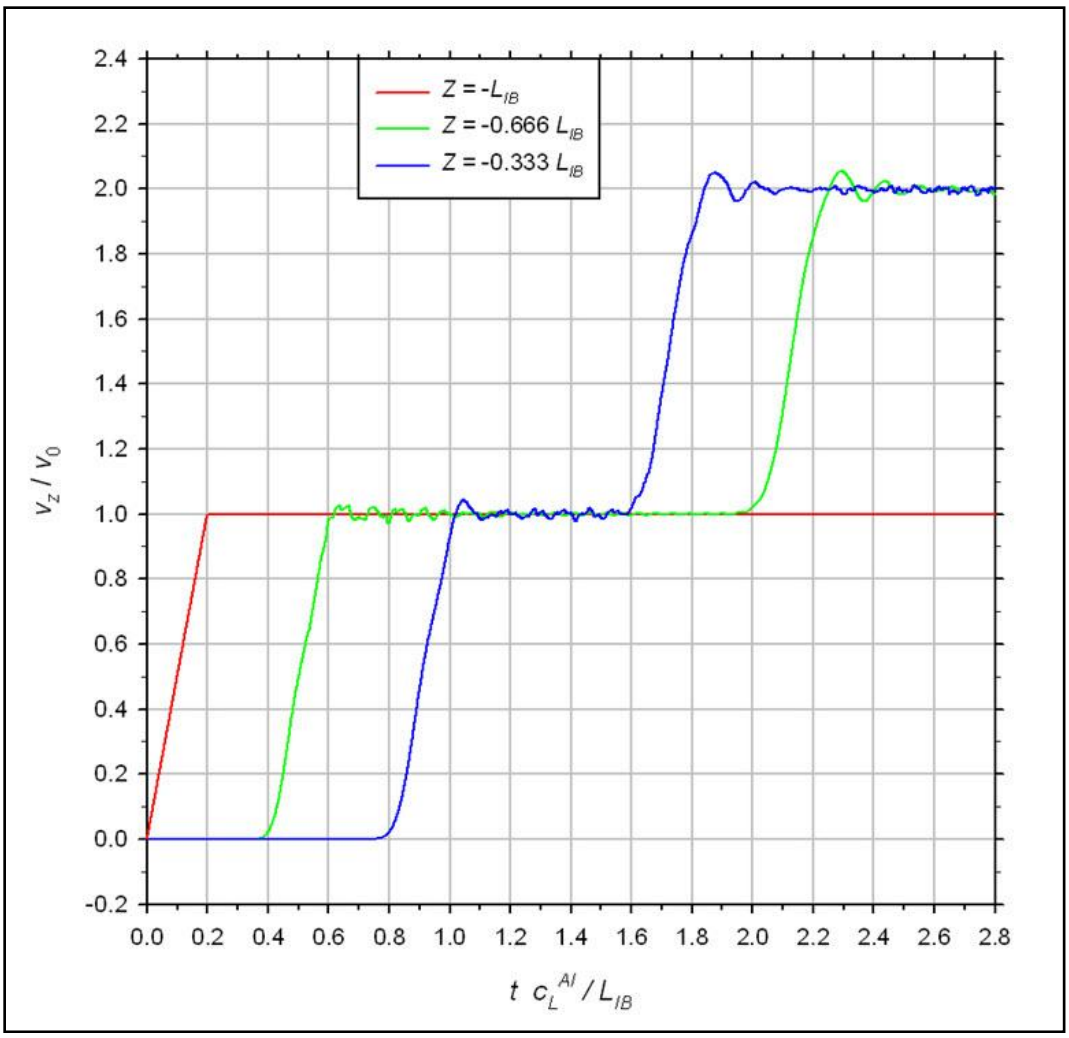

Figure 4. The scaled axial velocity vs. non-dimensional time at three locations on the centerline of the incident bar: the loading end with a 25-μs rise time, 1/3 of the way from the loading end, and 2/3 of the way from the loading end (blue curve).

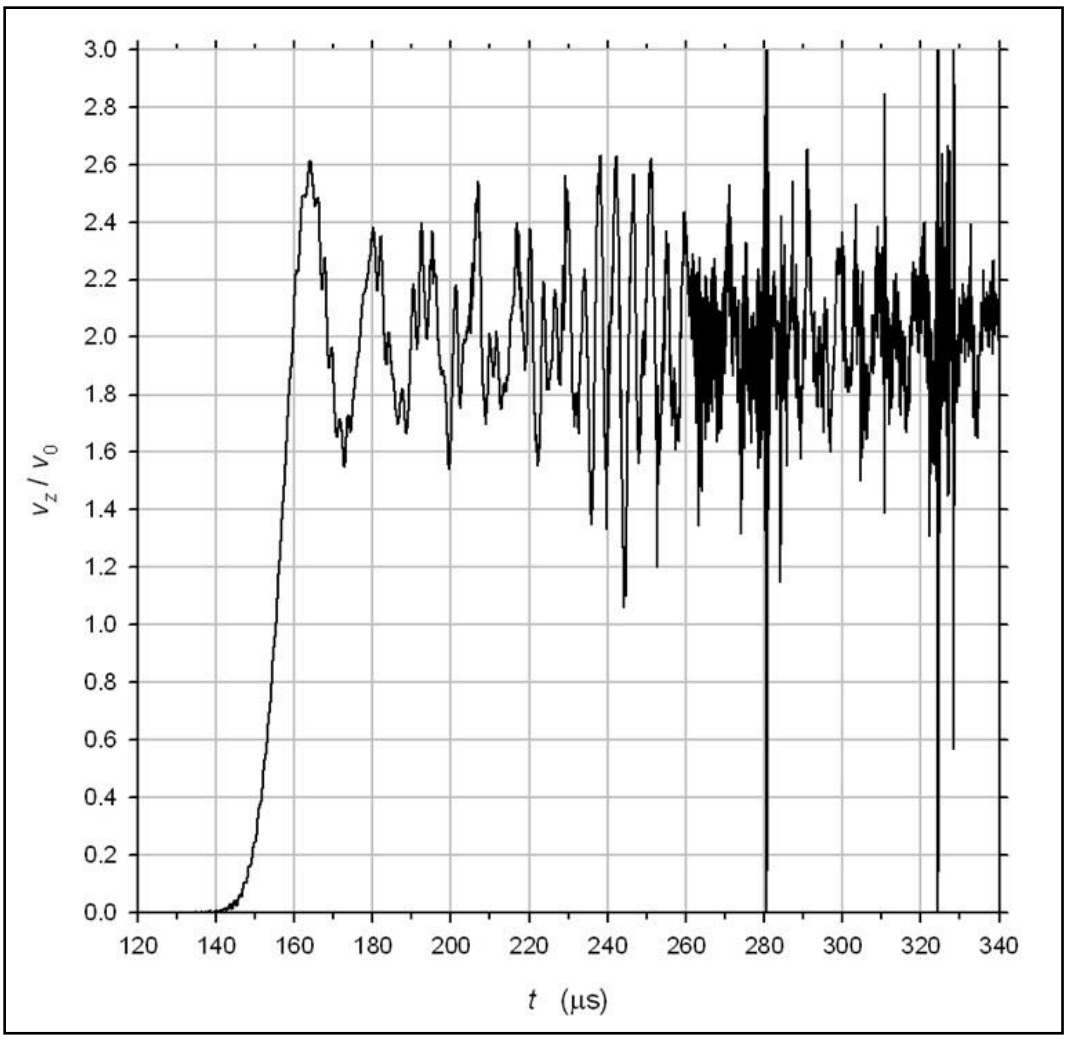

Figure 5. The scaled axial velocity history on the centerline of the incident bar at the S-IB interface for a 1-μs (initial) rise time.

Figures 5 and 6 give the velocity history on the centerline of the incident bar at the S-IB interface for the 1- and 25-μs initial rise times, respectively.[22] In these two figures the time is given in μs for later comparison with other plots. Note that the particle velocity ramps up to nearly double its initial value plateau v_0, as would be expected from reflection of the wave at a free surface. This is consistent with the small specimen/bar impedance ratio (see table 1). This doubling of the velocity on reflection is also evident at later times for the two interior locations in figures 3 and 4. The Mooney-Rivlin model was used for the specimen in these simulations, but in view of the low impedance ratios for all specimen models considered here, only small differences in the particle velocity histories in the incident bar after reflection would be expected for the other specimen models.

[22] The incident bar velocity v_z in these figures was denoted by v_{IB} in equation 10.

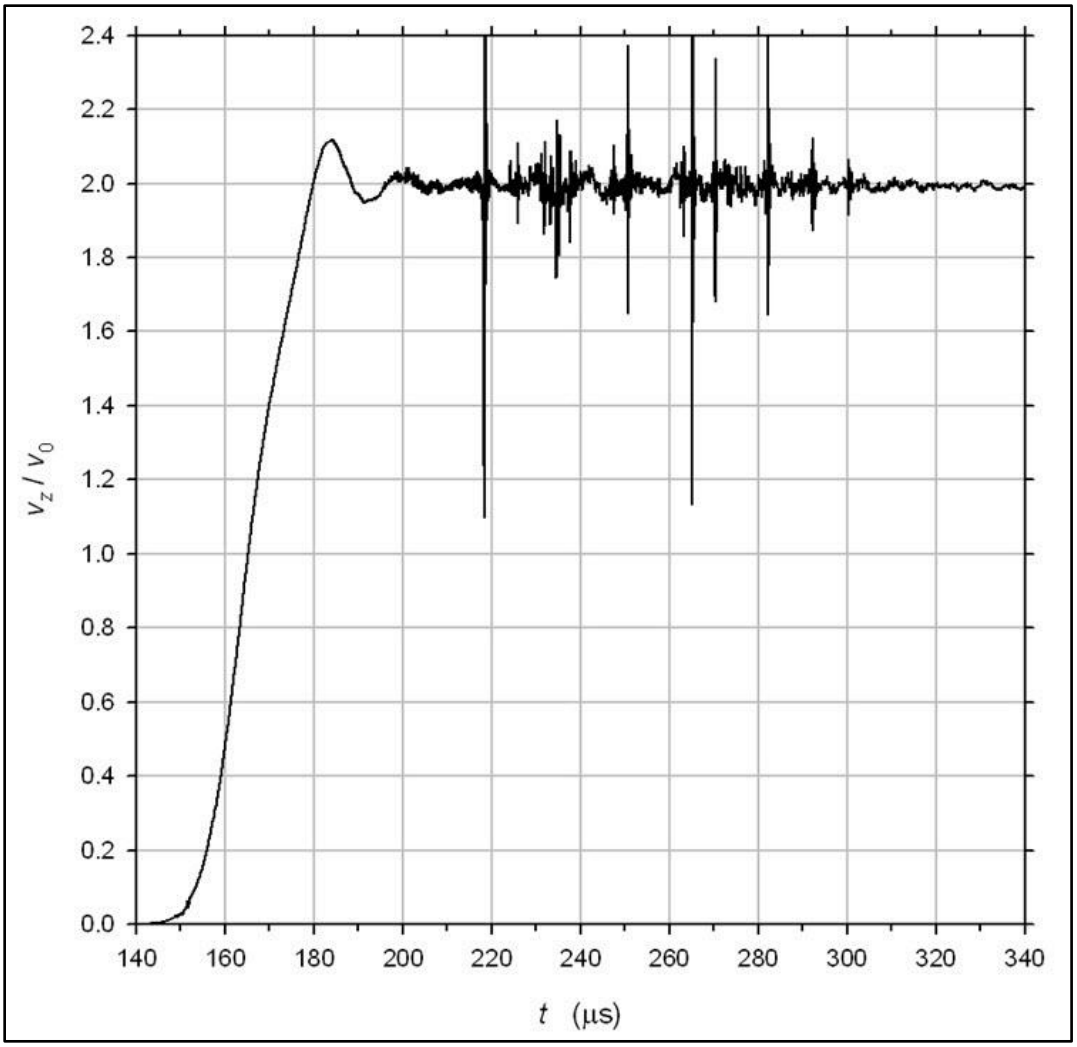

Figure 6. The scaled axial velocity history on the centerline of the incident bar at the S-IB interface for a 25-μs (initial) rise time.

A comparison of figures 3 and 5 (1-μs initial rise time) with figures 4 and 6 (25-μs initial rise time) shows that the computational "pulse shaping" has substantially smoothed the loading wave in the latter case. Also of interest is the increase in the final rise times of these waves due to dispersion in the bar. This final rise time could be defined as the difference between the time at the first peak in velocity at the S-IB interface and the arrival time of the wave at the S-IB interface. However, precise arrival times are difficult to determine from the plots in figures 5 and 6. A close inspection of figure 5, for example, reveals barely discernable peaks in the oscillatory toe of the velocity history starting at about 135 μs, although there is no substantial increase in velocity until about 140 μs. Thus, for the 1-μs *initial* rise time, most of the *final* rise in particle velocity at the S-IB interface occurs from 140 to 164 μs, that is, over a 24-μs time interval. For the 25-μs *initial* rise time, most of the *final* rise in particle velocity at the S-IB interface occurs from 143 μs to 184 μs, that is, over a 41-μs time interval.

Of the three curves in figures 3 and 4, the blue curves correspond to a point in the incident bar closest to the specimen, namely, 1/3 of the bar length back from the S-IB interface. In the following discussion, we consider the velocity history at this interior location at early times, that is, prior to the arrival of the reflected wave at a non-dimensional time of about 1.6. This represents the loading wave shortly before it arrives at the S-IB interface. For a given initial rise time, we compare this loading wave with the velocity history at the S-IB interface over a time interval that includes the first two major peaks in velocity at these two locations. Clearly, these velocity histories are qualitatively similar.[23] In particular, for the 25-μs rise time, a close inspection of the plots reveals that both curves have three inflection points prior to the first peak in velocity. For the 1-μs rise time, the situation is more complicated due to the small oscillations superimposed on the main curves; but if these are neglected, both curves would appear to have only one inflection point between the toe and the first peak. These inflection points in the velocity history correspond to extreme values in the acceleration of the bar, which turn out to be important for interpreting the stress histories in the specimen. Furthermore, the fact that these features are also exhibited prior to the arrival of the wave at the S-IB interface implies that they are not a consequence of interaction with the specimen, but instead are imposed upon the specimen.

Finally, we note that the axial velocity and axial acceleration of the specimen at the S-IB interface will coincide with the axial velocity and acceleration of the incident bar as long as the specimen and bar are in contact, but when a gap forms at this interface the velocities and accelerations of the bar and the specimen will generally be different.

6. Simulations with the Moony-Rivlin Model and a 1-μs Rise Time

All the simulations in this section are for the loading wave with a 1-μs initial rise time and the compressible Mooney-Rivlin model for the specimen. Conventions pertaining to the gaps are discussed in section 2.5. The results for the larger radius bar (the default radius R_B = 12.8 mm in this report) are presented in subsections 6.1–6.3. These results are compared with those for the smaller radius bar in subsection 6.4.

6.1 Results on the Centerline

All results in this subsection pertain to points on the centerline at the S-IB or the S-TB interface. We begin with some remarks about the figures and a few general observations, and then proceed to discuss the details of gap formation on the centerline.

[23] Of course, they differ quantitatively by a factor of nearly 2 due to a near doubling of the particle velocity on reflection of the wave at the S-IB interface. Also, as will be demonstrated in sections 6 and 7, the large velocity spikes at later times in figures 5 and 6 coincide with the closing of gaps on the centerline at the S-IB interface.

6.1.1 General Remarks

Figure 7 shows the time histories of the axial displacement of the incident bar (u_{IB}) and the specimen ($u_{S\text{-}IB}$) at the S-IB interface, as well as the history of the corresponding gap size ($\Delta_{S\text{-}IB} = u_{S\text{-}IB} - u_{IB}$). Similarly, figure 8 shows the time histories of the axial displacement of the transmission bar (u_{TB}) and the specimen ($u_{S\text{-}TB}$) at the S-TB interface, as well as the history of the corresponding gap size ($\Delta_{S\text{-}TB} = u_{TB} - u_{S\text{-}TB}$). In all of the figures in this report, the displacements and gaps are measured in microns. The histories of the gaps at the two interfaces are compared in figure 9. Figure 10 enlarges the plot in figure 9 in the vicinity of the time at which the gaps initially form. From figures 7 to 10, it is clear that gaps first form at both interfaces at about 165 μs. These gaps open and close several times, and they do so more frequently at the S-TB interface.

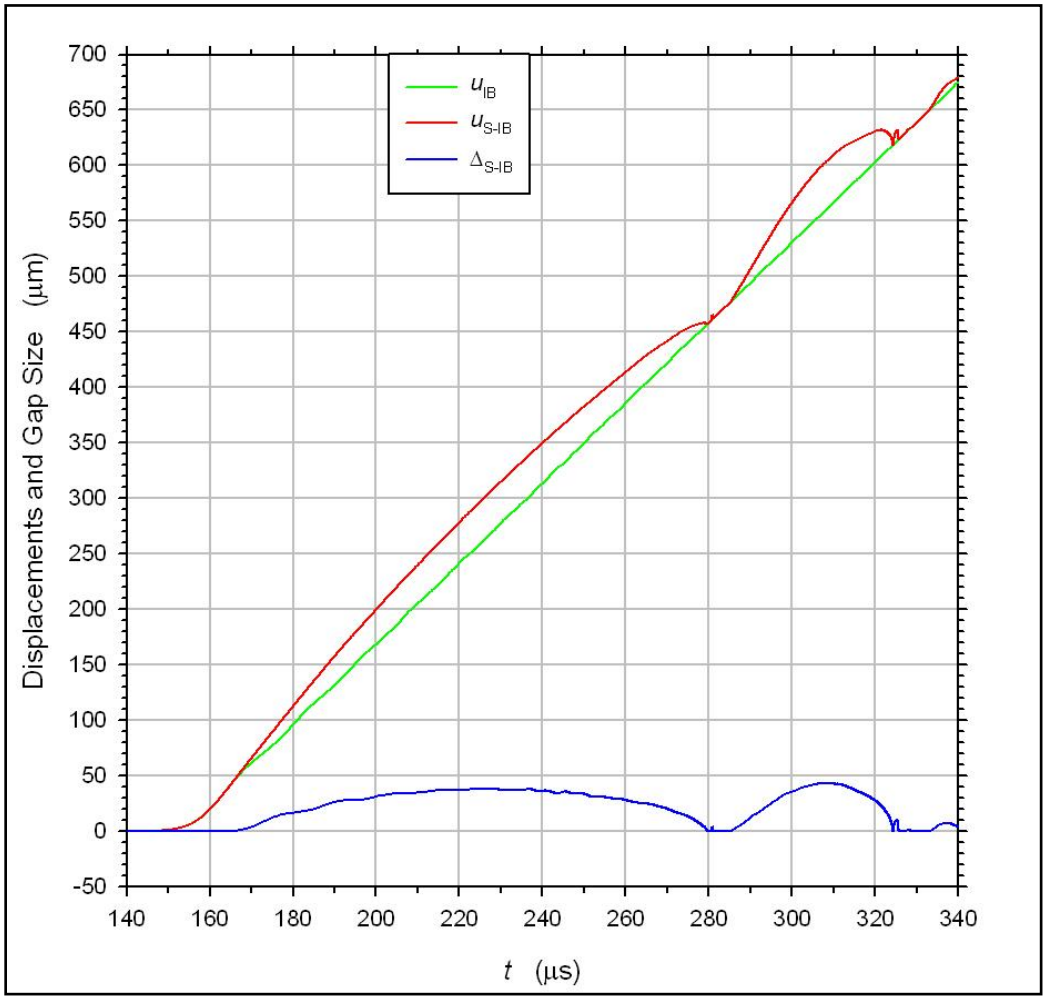

Figure 7. The histories of the axial displacement of the incident bar and the specimen on the centerline at the S-IB interface. Also shown is the history of the corresponding gap size (blue).

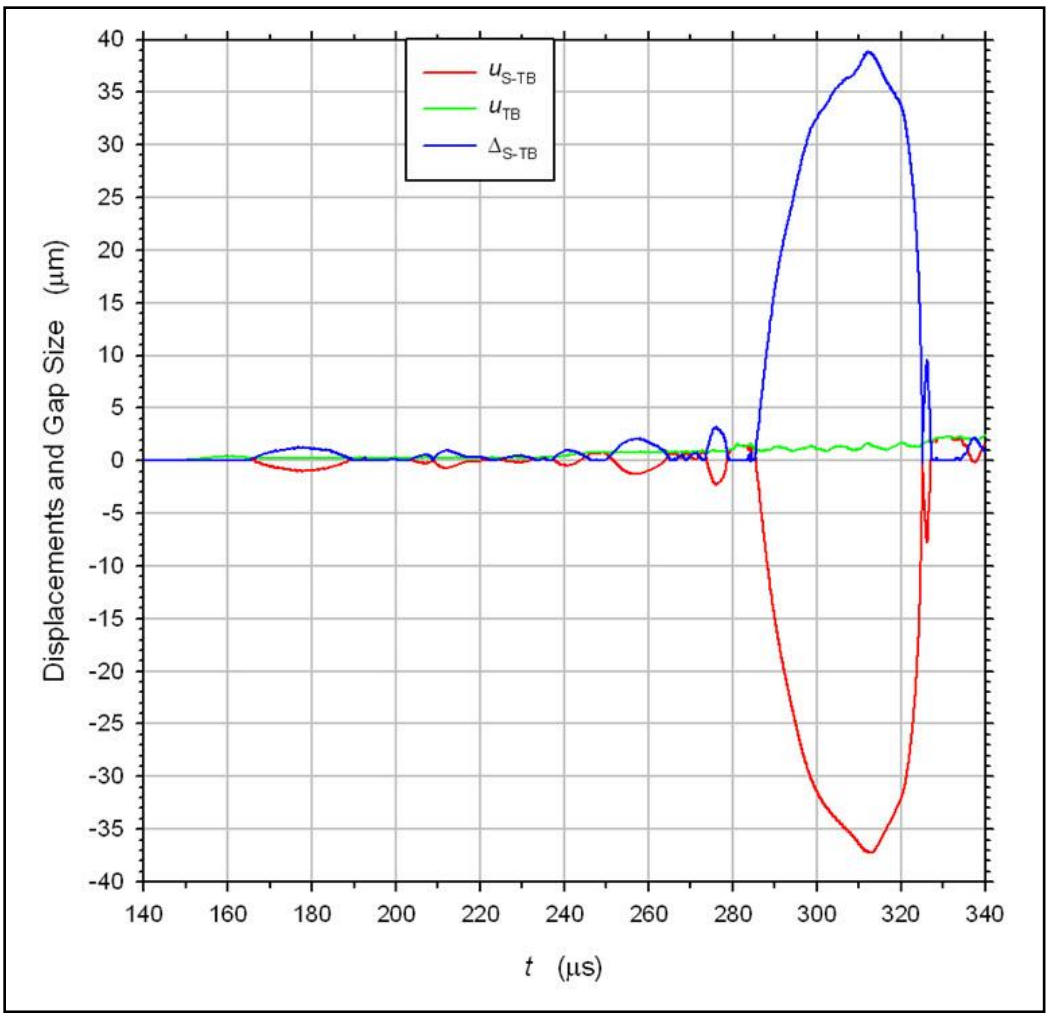

Figure 8. The histories of the axial displacement of the transmission bar and the specimen on the centerline at the S-TB interface. Also shown is the history of the corresponding gap size (blue).

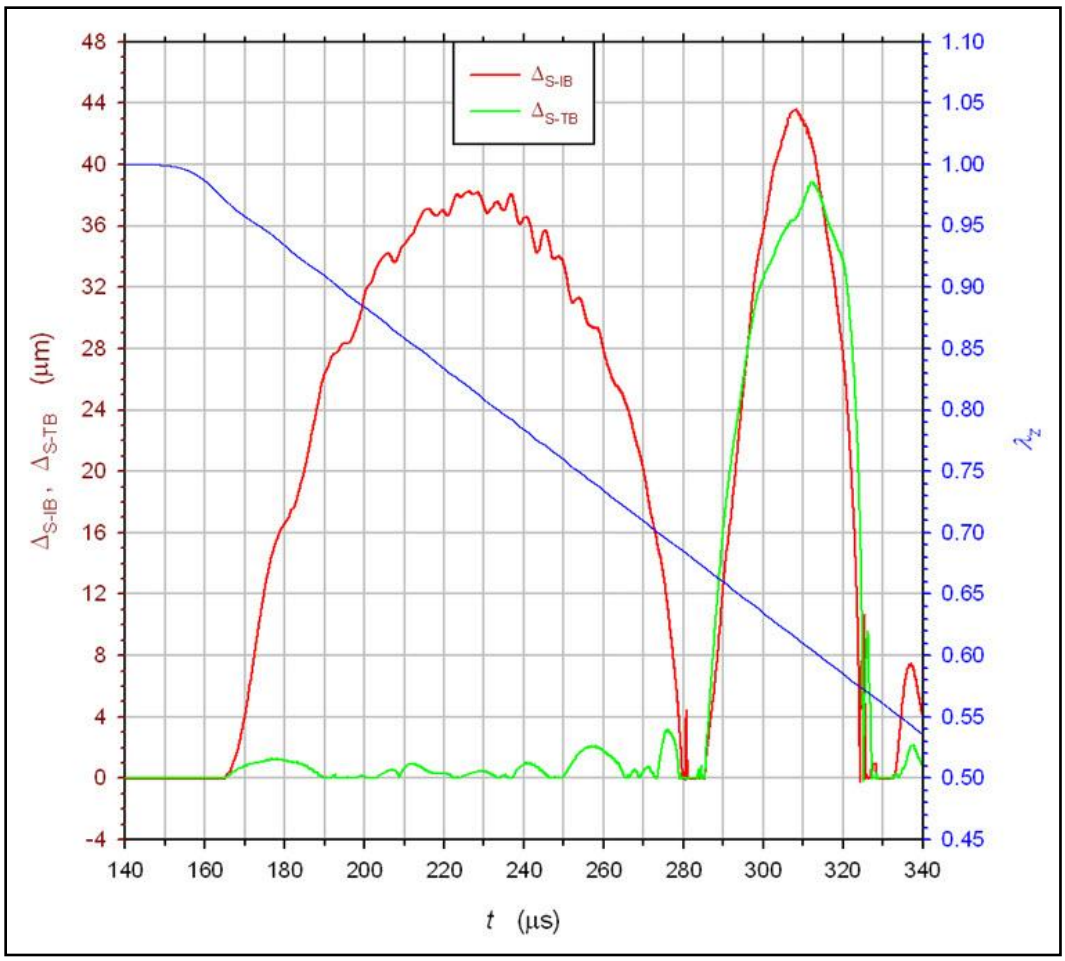

Figure 9. A comparison of the histories of the gap sizes on the centerline at the S-IB and S-TB interfaces. Also shown is the history of mean axial stretch in the specimen (blue).

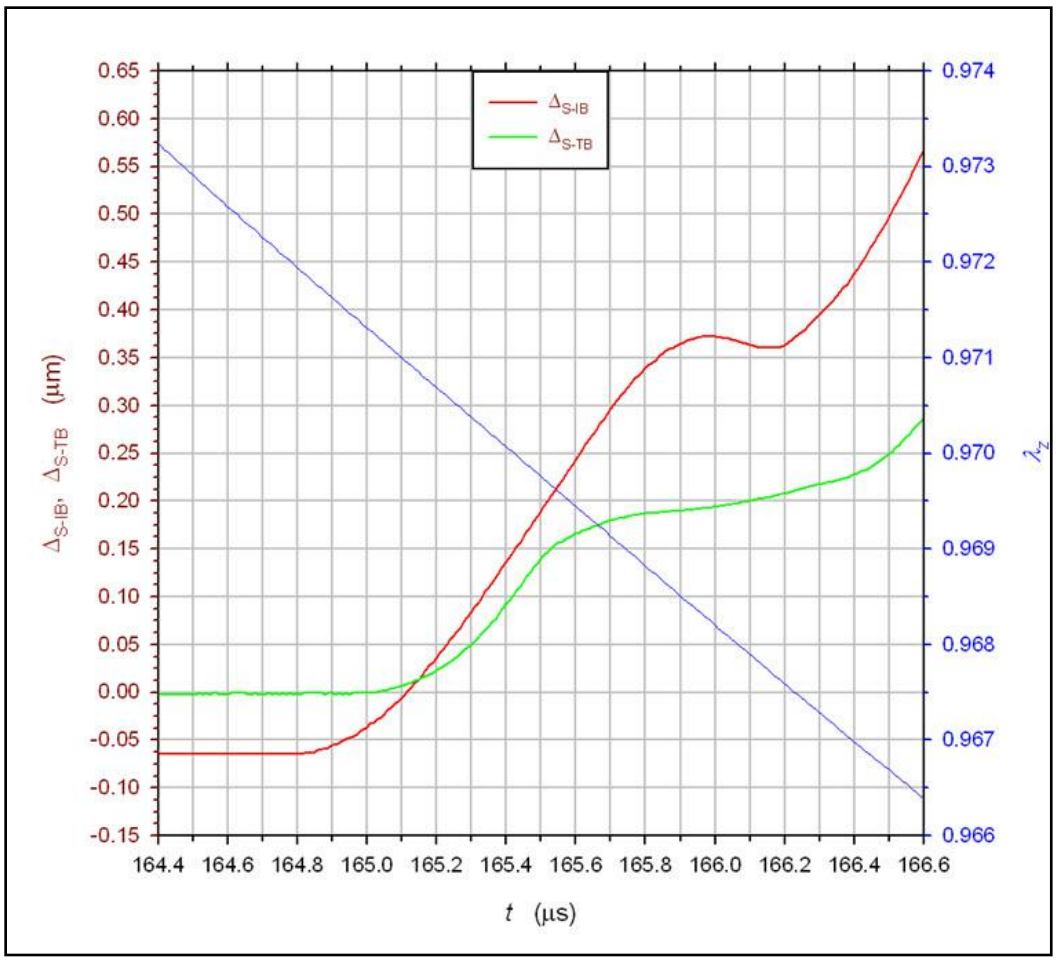

Figure 10. A comparison of the histories of the gap sizes on the centerline at the S-IB and S-TB interfaces in the vicinity of the time at which they first form. Also shown is the history of mean axial stretch in the specimen (blue).

The largest gaps observed were 43 μm at the S-IB interface and 38 μm at the S-TB interface. Since these maximum gap sizes are smaller than the initial 50-μm axial dimension of the specimen elements, the issues of mesh dependence and dependence on the contact algorithm naturally arise. These issues are addressed in appendix B. The results described there support the conclusion that the gap phenomenon is not a numerical artifact introduced by the contact algorithm or stemming from an insufficiently fine mesh. Additional support for the latter conclusion will be given in section 8 (linear elastic model for the specimen), where gap sizes are found to exceed the mesh size.

Since the loading wave in the incident bar arrives at the S-IB interface at (or slightly before) $t = 140$ μs, whereas the gaps first form about 25 μs later, gap formation does not coincide with arrival of the loading wave. Nor does gap formation coincide with the first wave reflections from either interface. Indeed, since the travel time of an axial longitudinal wave across the specimen is about 0.7 μs (see table 2), there is time for about 18 round trips of this wave before

the gaps form. In any case, an initially compressive longitudinal wave in the specimen should reflect from the transmission bar (and subsequently from the incident bar) as a compressive wave due to the higher bar impedance, so tensile stresses would not be expected to develop from these wave reflections. On the other hand, it is clear from table 3 that longitudinal unloading waves from the lateral (stress-free) surface of the specimen should arrive at the centerline at both interfaces about 3–4 μs after the loading wave in the bar first reaches the specimen, but this does not correlate with gap formation either. Finally, it is clear from table 2 that 25 μs is insufficient time for a shear wave to propagate more than a fraction of the thickness or the radius of the specimen; consequently, these waves cannot influence the formation of gaps. The possible influence of wave propagation in the bars on the formation of gaps is discussed in section 6.3.

The history of the mean axial stretch λ_z (see equation 8) is plotted on the right axis in figures 9 and 10. The slope of the axial stretch curve in figure 9 is nearly constant for $t \geq 200$ μs, and we estimate that the nominal strain rate for these times is between 2470/s and 2480/s. This is within 1% of the desired 2500/s strain rate.

Figure 11 plots the histories of the axial stress σ_{zz} in the specimen and the incident bar at points near the centerline and the specimen-bar interface; the corresponding gap size is also shown. Figure 12 is an analogous plot at the transmission bar interface. The stress is actually measured at the centroids of the specimen and bar elements adjacent to the centerline and the interface. Since the coordinates of these centroids do not coincide, slight differences in the values are not unexpected. Also, recall (section 2.6) that the axial stress is taken to be negative in compression. When a gap opens between the faces of the specimen and the bar, the axial stress should drop to zero on both faces, regardless of the size of the gap. The plots in figures 11 and 12 are consistent with this expectation, keeping in mind that these stresses are actually measured at a slight distance away from the faces.

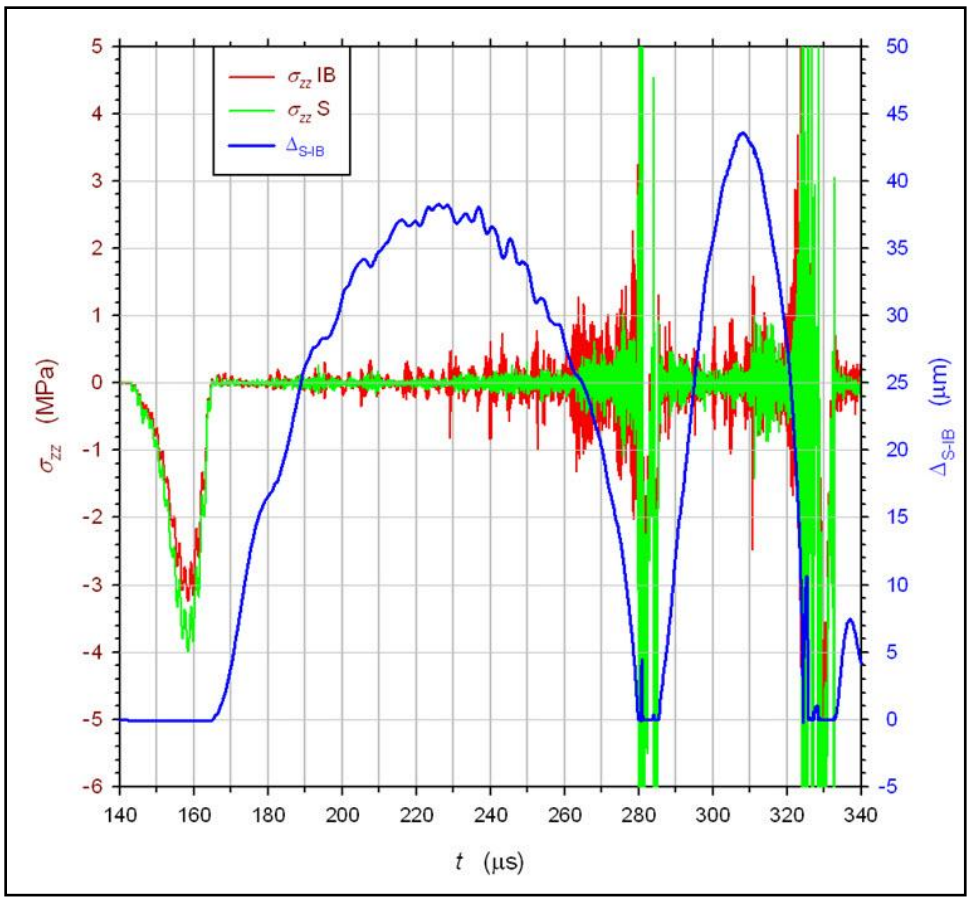

Figure 11. Histories of the axial stress (negative in compression) and the gap size on the centerline at the S-IB interface. The stress is measured at the centroids of the specimen and incident bar elements adjacent to the centerline.

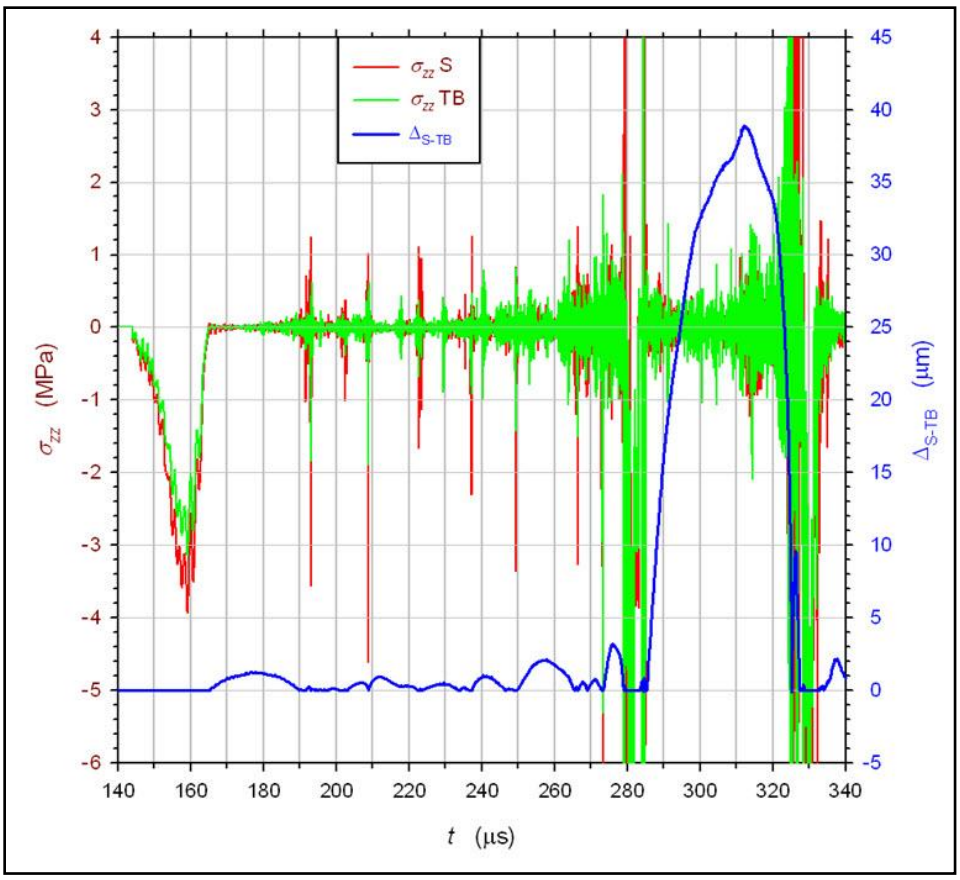

Figure 12. Histories of the axial stress (negative in compression) and the gap size on the centerline at the S-TB interface. The stress is measured at the centroids of the specimen and transmission bar elements adjacent to the centerline.

A comparison of the velocity history at the S-IB interface in figure 5 with the displacement, gap, stress and stretch histories in figures 7–12 leads to the following additional observations. For convenience of discussion we have divided the time histories into several stages.

6.1.2 The Initial Loading of the Specimen: Stage I (140–165 μs)

This first stage covers the initial loading of the specimen prior to gap formation. It begins with the first significant increase in the axial velocity of the incident bar at the S-IB interface at about 140 μs (see figure 5)[24] and ends with the onset of the gaps at 165 μs. From the axial stretch histories in figures 9 and 10, we see that the axial stretch decreases from 1 to about 0.97 over this 25-μs time interval; hence, the nominal axial strain increases from 0% to about 3%.

The first observable increase in axial stress at the S-IB interface occurs at about 143 μs (see figure 11). The stress increases in magnitude to a peak value of –4.0 MPa at around 158 μs, which is 7 μs prior to the formation of a gap at 165 μs. After this peak, the stress decreases more rapidly than it had risen and drops to zero at about 164 μs. Superimposed on this behavior are

[24] However, as observed at the end of section 5.3, the loading wave may have arrived as early as 135 μs.

smaller oscillations with a period of 1–2 μs; similar oscillations can be seen in the velocity history at the S-IB interface (figure 5). The history of the axial stress at the S-TB interface is qualitatively and quantitatively similar, with the times delayed by about 1 μs (see figure 12). In particular, the axial stresses at the two interfaces are approximately equal throughout this stage, from which we may infer that σ_{zz} is approximately uniform through the thickness of the specimen. In the experimental literature, this condition is referred to as *dynamic equilibrium*.[25]

At $t = 158$ μs (the instant of the stress peak in figure 11), the axial stretch λ_z is about 0.99, as can be inferred from figure 9. This stretch corresponds to a compressive nominal strain of 0.01, that is, 1% axial strain. A glance at the stress-stretch curve *for uniaxial stress* in figure A-1 reveals that when $\lambda_z = 0.99$, the axial stress σ_{zz} is a very small fraction of 1 MPa. Indeed, from equation A-13 and the values of A_1 and A_2 in table 3, we find that $\sigma_{zz} \approx -2.4$ kPa for a state of uniaxial stress when $\lambda_z = 0.99$.[26] This is three orders of magnitude smaller than the peak value of $\sigma_{zz} = -4.0$ MPa in figure 11, which (as previously noted) occurs at $\lambda_z = 0.99$. Consequently, the stress state at the instant of this peak ($t = 158$ μs) is nowhere close to the desired state of uniaxial stress. In fact, as established in the next paragraph, at this instant the stress state on the centerline is very nearly hydrostatic.

Recall from section 2.6 that at points on the centerline, the radial, hoop and axial directions are principal axes of stress and strain, the relations 14 hold exactly, and equation 15 holds approximately (for small volume changes, i.e., $J \approx 1$). As discussed in appendices A-2 and A-3, the stress difference $\sigma_{zz} - \sigma_{rr}$ on the centerline is given exactly by equation A-14 when $J = 1$ and approximately by that equation when $J \approx 1$. When $\lambda_z = 0.99$, equation A-14 yields the value –2.4 kPa.[27] Summarizing, we have $\sigma_{zz} - \sigma_{rr} \approx -2.4$ kPa and $\sigma_{\theta\theta} = \sigma_{rr}$ exactly, whereas $\sigma_{zz} = -4.0$ MPa. Hence, the differences between the principal stresses σ_{rr}, $\sigma_{\theta\theta}$, and σ_{zz} are either zero or at least three orders of magnitude smaller than the stresses themselves. It follows that all three principal stresses are nearly equal to each other and hence, by equation 11, nearly equal to $-p$. The volumetric strain $1-J$ at this peak pressure is approximately 0.001, that is, 0.1%.[28]

The preceding quantitative estimates apply only at the stress peak on the centerline. However, at neighboring times and at radial locations near the centerline we arrive at the same qualitative conclusion, namely, that the stress state is nearly hydrostatic for most of this stage (certainly

---

[25] It should be kept in mind that the stresses in figures 11 and 12 are measured on the centerline. On the other hand, only the mean axial stress on an interface can be inferred from experimental data, so it is the equality of the mean axial stresses at the two interfaces that is implied by the term dynamic equilibrium.

[26] As discussed in appendix A-3, equation A-13 holds approximately for uniaxial strain when $J \approx 1$ (i.e., small volume changes). Also, note that the axial strain is small enough that the exact relation in equation A-13 and the linear elastic approximation give essentially the same result.

[27] Since the right-hand side of equation A-14 equals the right-hand side of equation A-13, this value follows from the calculation in the preceding paragraph.

[28] This follows from setting p equal to $-\sigma_{zz}$ and using equation A-21 with $K = 4.0$ GPa (see section 3.2), which yields $1-J = 4.0$ MPa/4.0 GPa.

during the time interval 147–163 μs in which $|\sigma_{zz}|$ exceeds 0.4 MPa), and the axial stress exceeds that for a uniaxial stress state by several orders of magnitude.

From figure 5, we estimate that the peak slope of the velocity-time curve during Stage I also occurs around 158 μs.[29] Thus, the peak in the axial acceleration of the incident bar at the S-IB interface coincides with the peak in the axial stress on the centerline, and as that acceleration decreases towards zero so does the axial stress. The axial acceleration of the incident bar induces an axial acceleration in the specimen, which in turn induces a radial acceleration in the specimen. Therefore, it seems likely that during this stage the value of the axial stress and the nearly hydrostatic stress state in the neighborhood of the stress peak are inertial effects associated with the accelerations imposed on the specimen by the incident bar.[30] Furthermore, since the specimen is approximately in dynamic equilibrium (at least along the centerline), these would appear to be primarily radial inertia effects. Song et al. (*6*) also observed a correlation between axial acceleration and axial stress in the specimen at early times in their SHPB tests and numerical simulations on gel specimens and likewise concluded that this was a radial inertia effect. This conclusion is also consistent with various theoretical analyses of inertial effects applied to soft materials (*26–33*). We will return to these issues in section 7, where we discuss the case with a 25-μs initial rise time.

6.1.3 Gap Opening and Closure (Stages II–VI)

Stage II (165–280 μs): This stage begins with the opening of gaps at both interfaces and ends with the first closing of the gap at the S-IB interface. Over this 115-μs time interval, the nominal axial strain increases from 3% to 32% (see figure 9).

From figure 10, we see that a gap begins to form at the S-TB interface at about 165.0 μs and at the S-IB interface about 0.1 μs later. Prior to this time, $\Delta_{S\text{-}IB}$ is negative, which means that the specimen and incident bar have interpenetrated. The maximum amount of this interpenetration is 0.06 μm, which is 0.12% of the initial axial edge length of a specimen element. The penalty-based contact algorithm allowed this degree of interpenetration; it is also evident in several subsequent figures. This interpenetration begins to decrease at about 164.8 μs, which is 0.2 μs prior to the instant at which the gap forms at the S-TB interface. The axial stretch at the onset of the gaps is about 0.971. The corresponding nominal axial strain is 0.029, that is, very close to 3%.

From figure 5, we see that the peak value of the axial velocity of the incident bar occurs at about 164 μs. The axial acceleration of the bar is zero at this instant and negative for some time thereafter. The axial stress at both interfaces also reduces to zero at about 164 μs (figures 11 and 12). Hence, both the axial stress and the axial acceleration at the S-IB interface drop to zero at about the same time, and a gap forms at that interface about 1 μs later, that is, about 1 μs after

[29] Here, we disregard the smaller oscillations superimposed on the main curve.

[30] In this regard, see the comments in the next to last paragraph in section 5.3.

the incident bar begins to decelerate. That a gap forms just after the axial stress drops to zero is not surprising. The important observation here is that this occurs when the axial acceleration of the S-IB interface passes through zero. We will return to this point in section 7.

With the exception of some minor oscillations, the incident bar continues to decelerate until about 173 μs and then re-accelerates until 180 μs (figure 5). However, the S-IB gap does not close when the incident bar re-accelerates. The bar velocity goes through many oscillations about its mean value of about $2v_0$ before the S-IB gap first closes at 280 μs. The gap at the S-TB interface is also closed at 280 μs, although it has opened and closed several times prior to this. Nevertheless, a gap exists at the S-TB interface for most of this stage. Observe the minor spikes in stress at the S-TB interface when the gap closes there. Note that the magnitude of the S-TB gap never exceeds 4 μm in this stage, whereas the S-IB gap reaches a maximum of 38 μm at about 226 μs.

Stage III (280–286 μs): The gaps at both interfaces close at 280 μs and remain closed, for the most part, over this 6-μs time interval. The S-IB gap does re-open momentarily at the beginning of this stage, and sub-micron gaps re-open momentarily at both interfaces near the end of the stage. The first large spike in the velocity at the S-IB interface (figure 5) occurs at the beginning of this stage, and large spikes in the stress (figures 11 and 12) occur throughout this stage.

Stage IV (286–324 μs): The gaps re-open and remain open at both interfaces over this 30-μs time interval. The axial stresses near the interfaces again drop to nearly zero. The gaps are now roughly the same size at both interfaces. The S-IB gap reaches a peak value of 43 μm at 308 μs; the S-TB gap reaches a peak value of 38 μm about 4 μs later. These are the maximum gap sizes achieved in this simulation. During this stage, the nominal axial strain increases from about 33% to 43%.

Stage V (324–333 μs): The gaps at both interfaces close and remain closed, for the most part, over this 9-μs time interval. This gap closure results in the second large spike in the velocity at the S-IB interface (figure 5) and the second group of large spikes in the stress (figures 11 and 12) as the specimen "slaps" the bars.

Stage VI (333–340 μs): The gaps re-open and remain open at both interfaces. The axial stresses near the interface again drop to nearly zero. At 340 μs, the axial stretch is 0.535 and the nominal axial strain is 46.5%. Thus, gaps persist to large strains at both interfaces.

6.2 Results at Other Radial Locations

Figure 13 shows deformed mesh plots in the vicinity of the specimen at 236 μs (Stage II). The centerline lies along the bottom of each plot. Thus, figure 13a shows the entire (deformed) specimen mesh in the 2-D axisymmetric simulation; note the bulging at the free surface of the specimen near the S-IB interface. A close examination of figure 13a reveals that the gap at the S-IB interface extends outward from the centerline for about ¾ of the specimen radius, and that a gap does not form at any radial location along the S-TB interface at this instant. The S-IB gap is

clearly visible in figure 13b and is seen to be approximately uniform in size for much of its length.[31] From figure 9, we conclude that the gap at the S-IB interface is about 37 μm at the centerline; this is roughly the axial dimension of the deformed specimen elements. The axial stretch at this instant is about 0.79, corresponding to a nominal axial strain of 21%. Figures 8 and 9 also confirm that there is no gap on the centerline at the S-TB interface at this time.

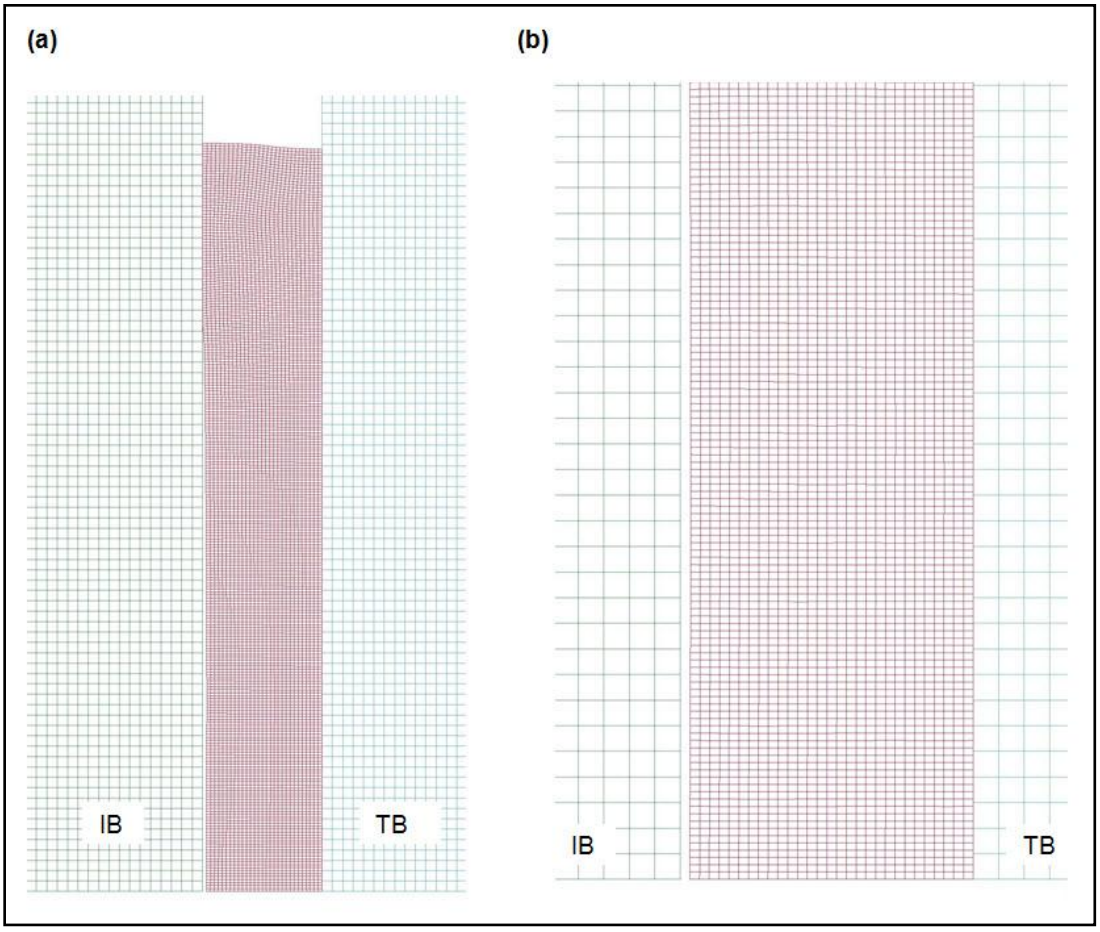

Figure 13. Deformed mesh plots in the vicinity of the specimen at $t = 236$ μs and an axial strain of 21%: (a) full specimen mesh; (b) enlargement of the mesh near the centerline, where the gap size is about 37 μm.

Figures 14 and 15 plot the gap size at the S-IB interface vs. the deformed specimen radius r at selected times. Figure 16 gives the same information at the S-TB interface.

[31] The latter observation is consistent with the results in figure 14.

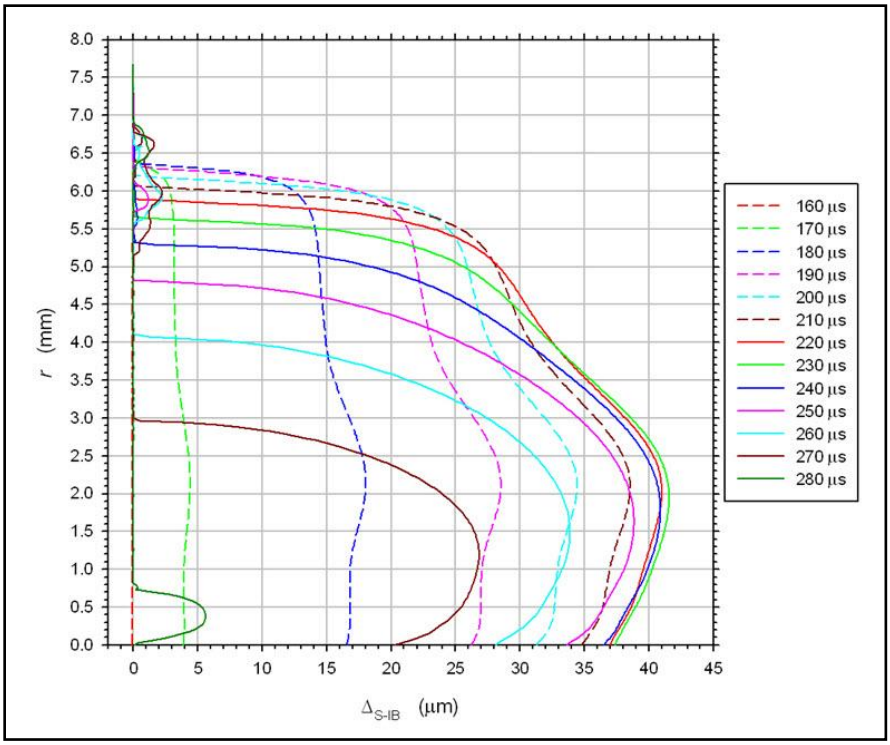

Figure 14. Gap size vs. deformed specimen radius at the S-IB interface at selected times.

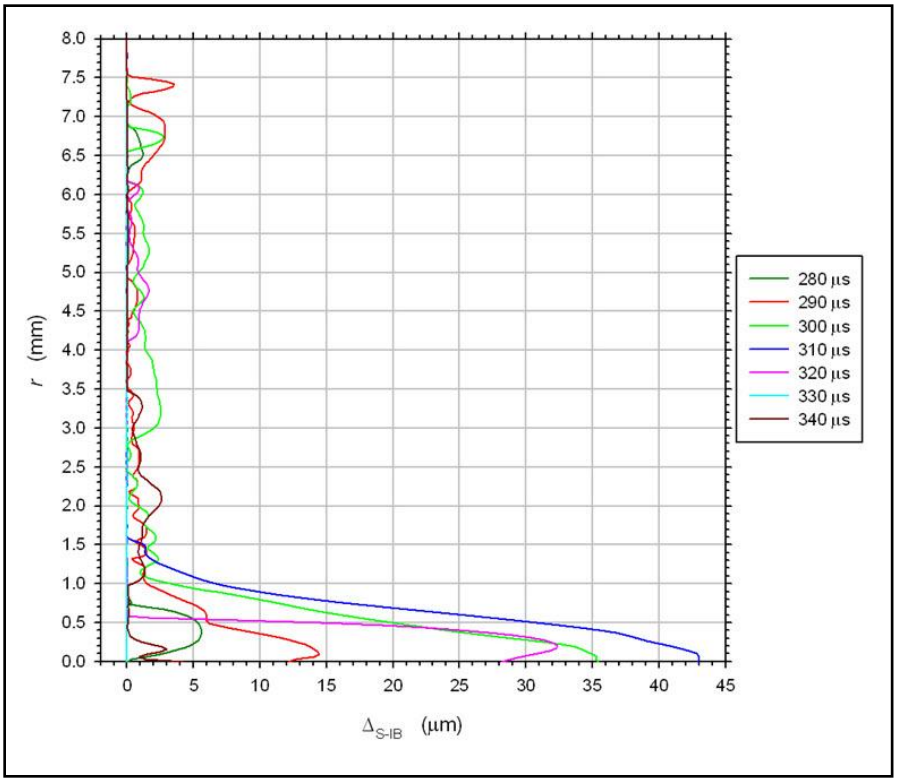

Figure 15. Gap size vs. deformed specimen radius at the S-IB interface at selected times.

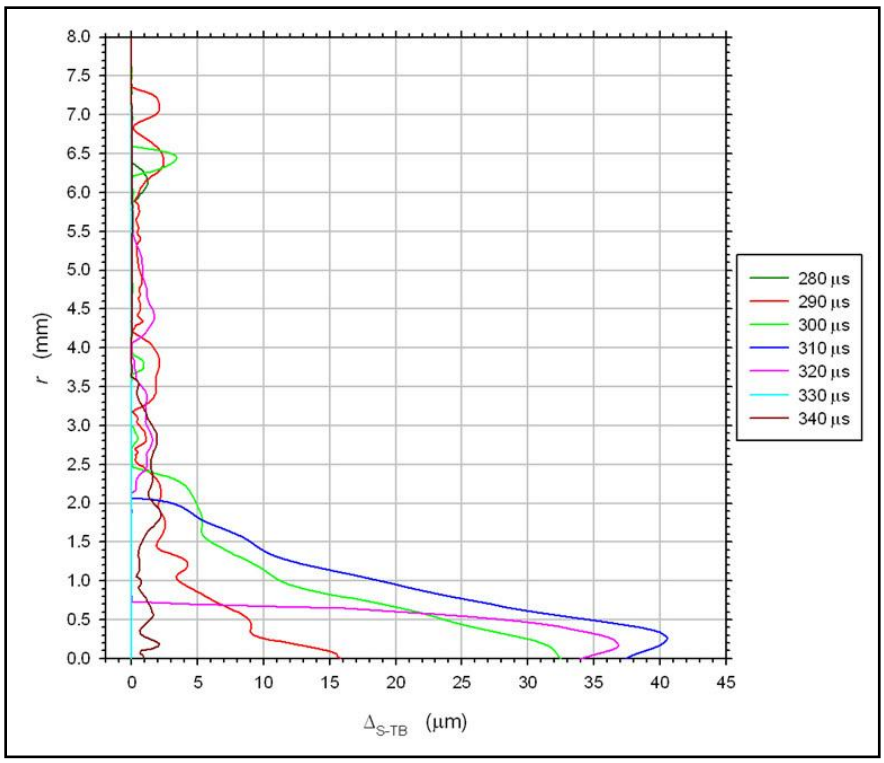

Figure 16. Gap size vs. deformed specimen radius at the S-TB interface at selected times.

The selected times in figure 14 span Stage II and also include the instant t = 160 μs, which is prior to any gap formation. Note that at each instant after 160 μs, the largest gap occurs at a non-zero radial coordinate, that is, off the centerline. The largest gap size during this stage is nearly 42 μm, which occurs at 230 μs and 2 mm from the centerline. From 170 to 230 μs, the size of the gap increases with time and the gap extends along most of the specimen radius, that is, across most of the face of the specimen. Over this time interval, the nominal axial strain increases from 4% to 19%. From 230 to 280 μs, both the radial extent of the gap and the maximum size of the gap decrease with time. Over this time interval, the nominal axial strain increases from 19% to 32%. We estimate that the gap extends over roughly half the radius of the specimen at t = 265 μs and a nominal axial strain of 28%.

The selected times in figures 15 and 16 span Stages III–VI. From these figures, we conclude that the radial locations where the S-IB and S-TB gaps in Stage IV exceed a few microns are confined to the vicinity of the centerline. The largest gap sizes during this time interval occur at 310 μs and are nearly equal: 43 μm at the S-IB interface and 41 μm at the S-TB interface.

6.3 Pressure Contours

Figures 17–23 display pressure contours in the vicinity of the specimen at specific times between 152 and 166.4 μs. Also indicated at the top of each contour plot is the mean axial stretch λ_z at the selected time. Each contour plot shows only a small portion of the length of the bars but does span the bars from the centerline (bottom) to the stress-free lateral surface (top). The incident

bar is on the left and the transmission bar is on the right. Recall that the radius of the bars is slightly more than twice the initial radius of the specimen. Hence, the large, rectangular, white region between the bars in these contour plots is just empty space above the specimen. The specimen-bar interfaces are just barely distinguishable as the thin, light lines below this region. The length scale on these figures can be inferred from the thickness of the specimen, which is initially 1.45 mm and does not change substantially over the time interval considered here.

Since there is no load on the face of a bar where it overhangs the specimen, the stress on that part of the *surface* is zero, and since the bar faces remain very nearly planar, we may conclude that σ_{zz}, σ_{rz}, and $\sigma_{\theta z}$ are essentially zero on the overhanging faces. But the stress tensor $\boldsymbol{\sigma}$ need not be identically zero at points on the overhanging surface, so the pressure need not be zero there. Indeed, the radial and hoop stresses in the bars could be nonzero at some points on the overhanging surface, which would result in a nonzero pressure there; cf. equation 11.[32] Similarly, at those places and times at which the specimen and the bars are in contact, the pressure need not be continuous across the interface. Since the contact is frictionless, the only nonzero component of the traction vector at the specimen-bar interface is the axial stress σ_{zz}, so it is this stress component that must be continuous across the interface when there is contact. Likewise, it is the axial stress (but not necessarily the pressure) that must be zero on the specimen and bar faces at points where a gap forms.

Recall that pressure is taken to be positive in compression (equation 11). The light green areas in the contour plots are regions of positive pressure, whereas the dark green areas are regions of negative pressure. The dark (and typically jagged) curves bounding these two green regions are the zero-pressure level curves. Clearly, the pressure field in the specimen and the bars is an extremely complex function of position and time. Reflection of waves from the interfaces and the free surfaces and oscillations induced in the specimen and bar by the passage of these waves make it difficult to sort out cause and effect here, particularly in view of the fact that the pressure is only part of the full stress state.

Figures 17–20 display pressure contours at specific times between 152 and 164.8 μs, which is prior to the formation of a gap. Negative (tensile) pressures develop in the bars prior to developing in the specimen. Even at the early time of 152 μs (figure 17), there are small regions of negative pressure in portions of the bars that overhang the specimen. These tensile regions are most likely generated by unloading waves from the stress-free portion of the bar faces. By 163.4 μs (figure 18), negative pressure has developed in the incident bar in a region bordering the centerline, about 6–8 specimen lengths back from the S-IB interface. From 164.2 to164.6 μs (figures 19 and 20), the pressure in the incident bar oscillates (with axial distance from the specimen) between positive and negative values.

[32] Likewise, since the low amplitude waves in the bars should induce little bulging of the stress-free lateral surface of the bars, σ_{rr}, $\sigma_{\theta r}$, and σ_{zr} are essentially zero on this surface, although the pressure need not be zero there.

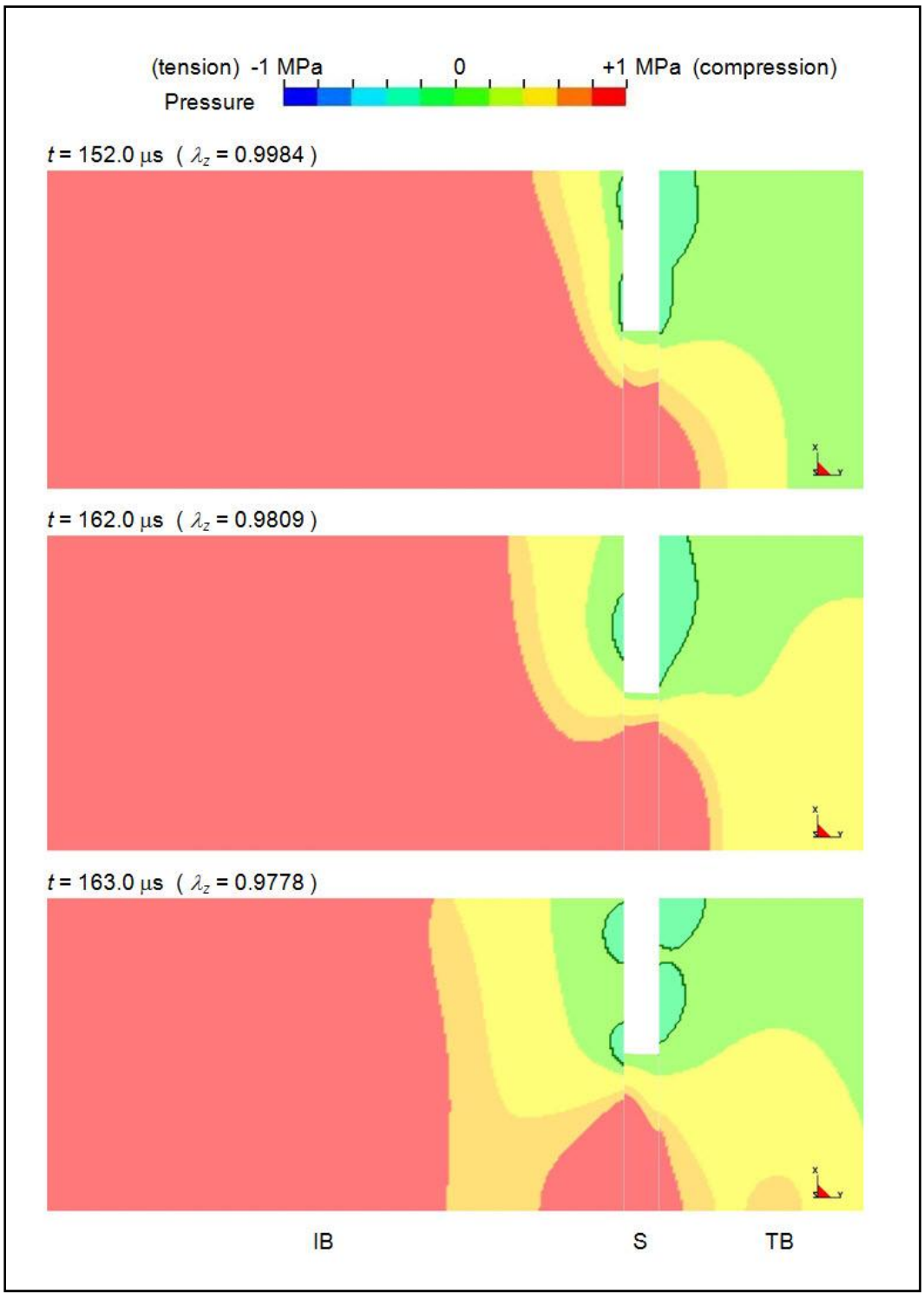

Figure 17. Pressure contours in the vicinity of the specimen at selected times.

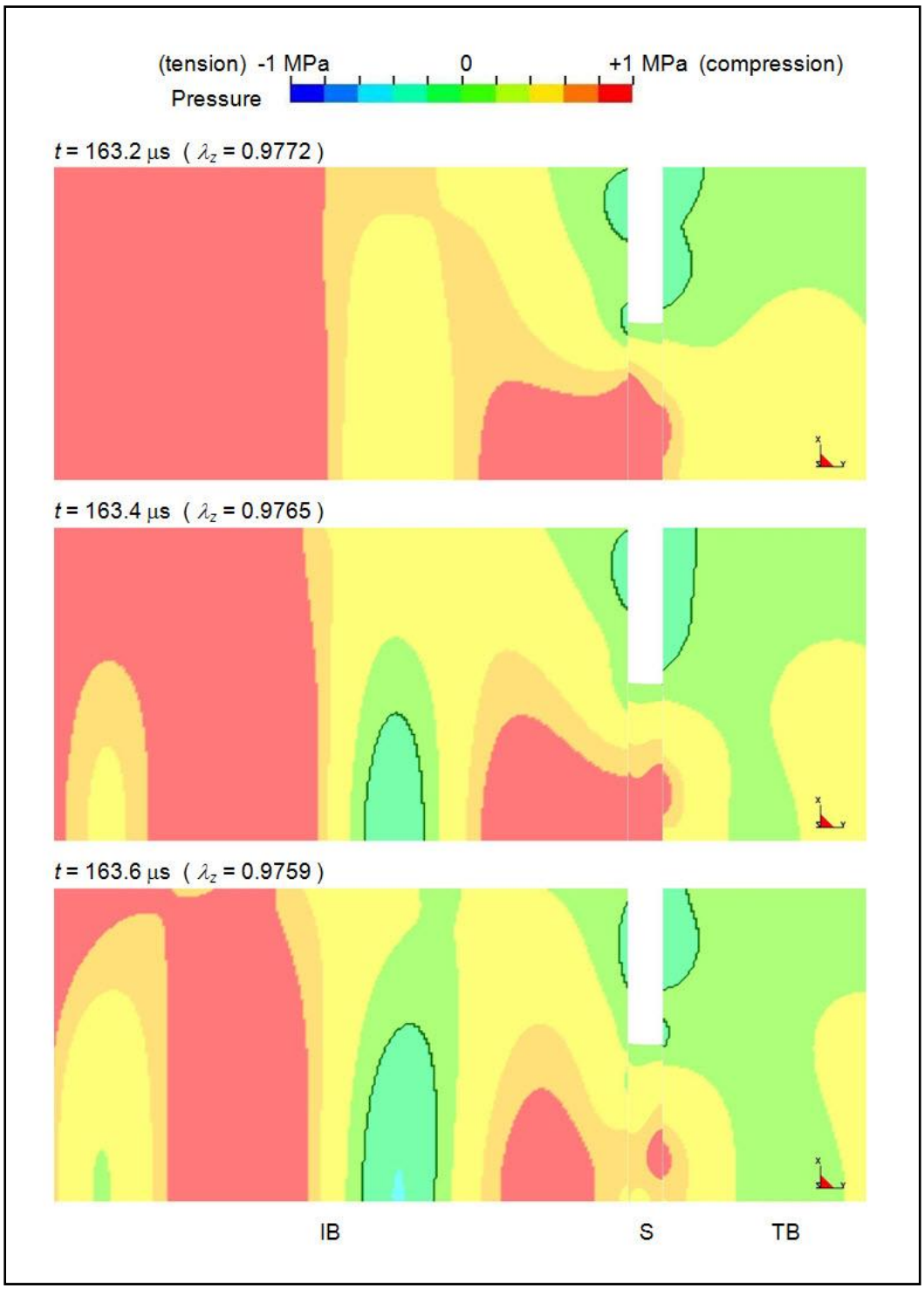

Figure 18. Pressure contours in the vicinity of the specimen at selected times.

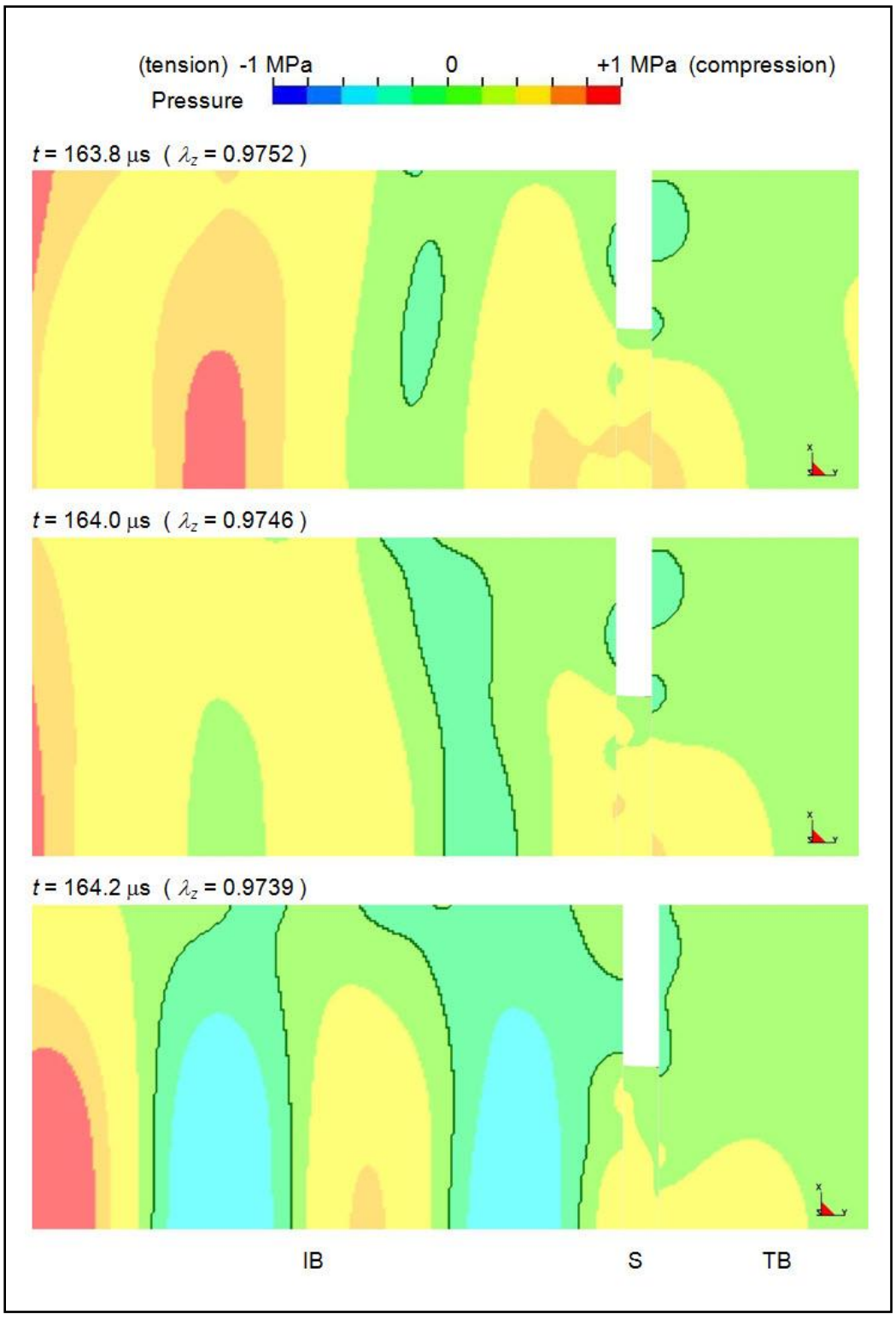

Figure 19. Pressure contours in the vicinity of the specimen at selected times.

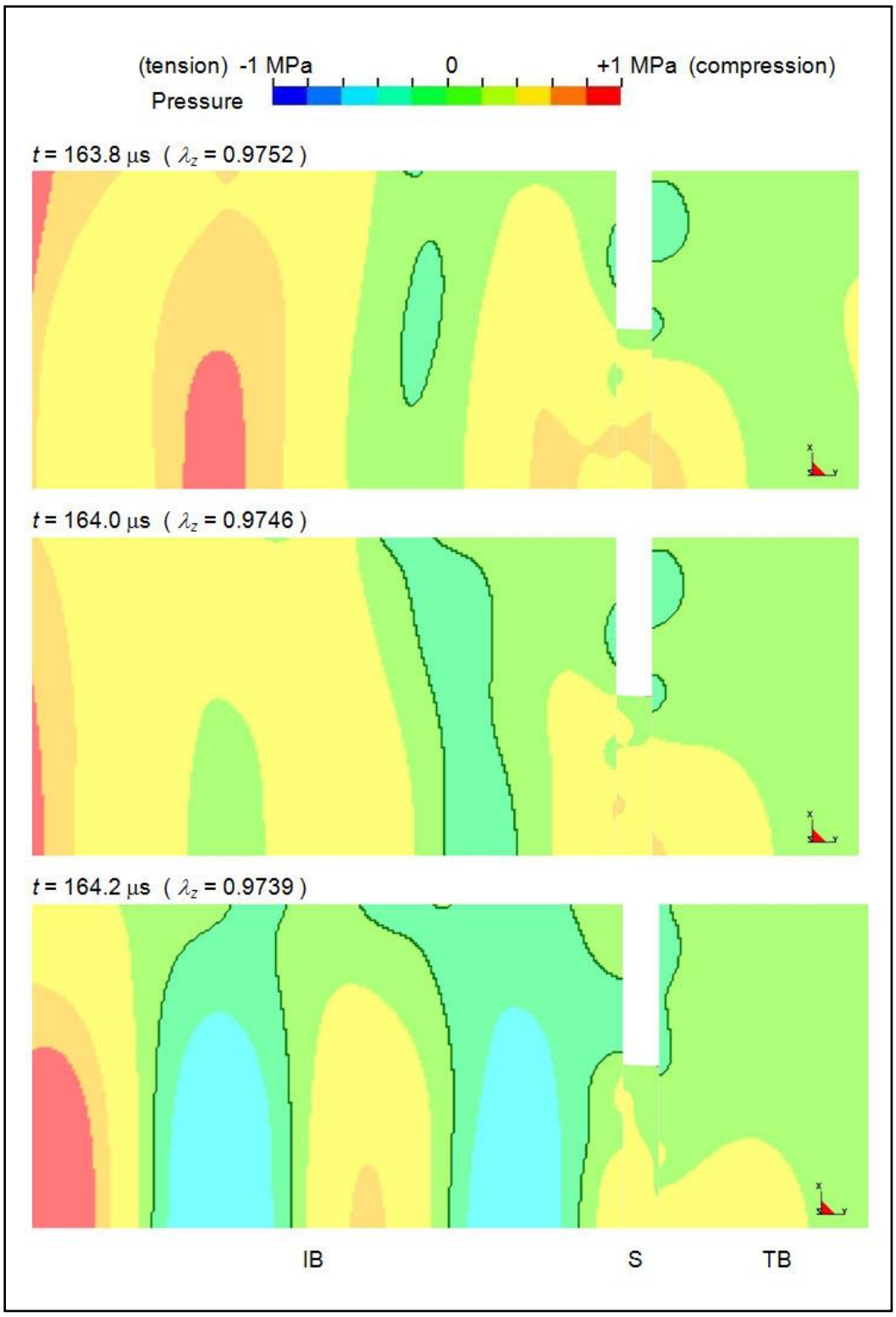

Figure 20. Pressure contours in the vicinity of the specimen at selected times.

Negative pressure does not develop in the specimen until 164.4 μs (figure 20), although it is limited to very small regions. By 164.8 μs, most of the specimen and the regions of the bars adjacent to it are in a state of negative pressure. Gap formation begins after 164.8 μs (see section 6.1.3). From 165.0 μs onward, (figures 21–23), the regions of the bars adjacent to the specimen are primarily in a state of negative pressure. However, the sign of the pressure in the specimen oscillates (with time) from primarily negative (164.8–165.2 μs) to primarily positive (165.4–165.8 μs) and back again to primarily negative (166.0–166.4 μs). In view of this oscillation in the sign of the pressure, it is possible that the axial stress also oscillates between tensile and compressive values at points in the interior of the specimen,[33] although this cannot be confirmed from the pressure contours.

[33] Recall that tensile axial stresses cannot be supported at the specimen and bar faces.

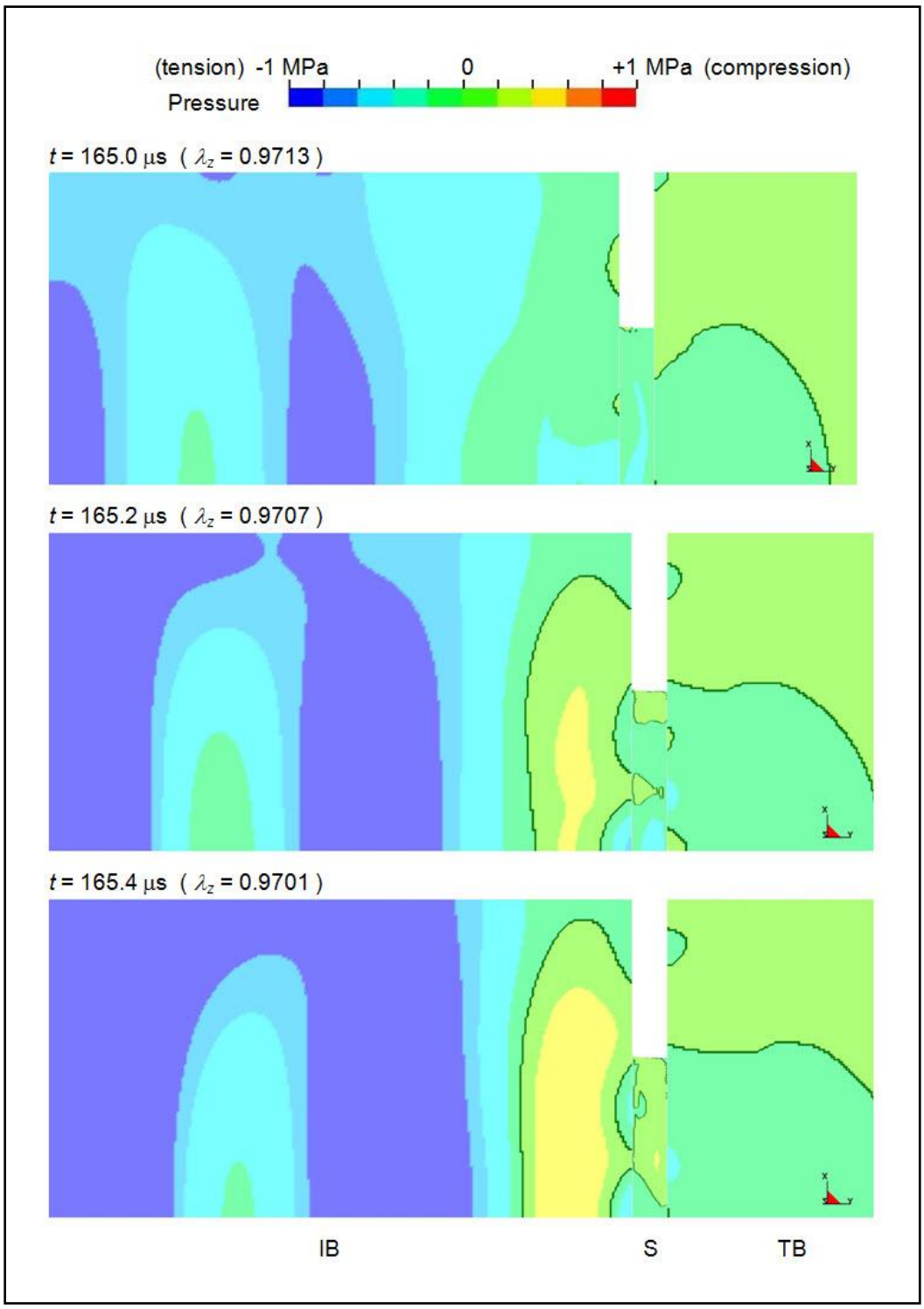

Figure 21. Pressure contours in the vicinity of the specimen at selected times.

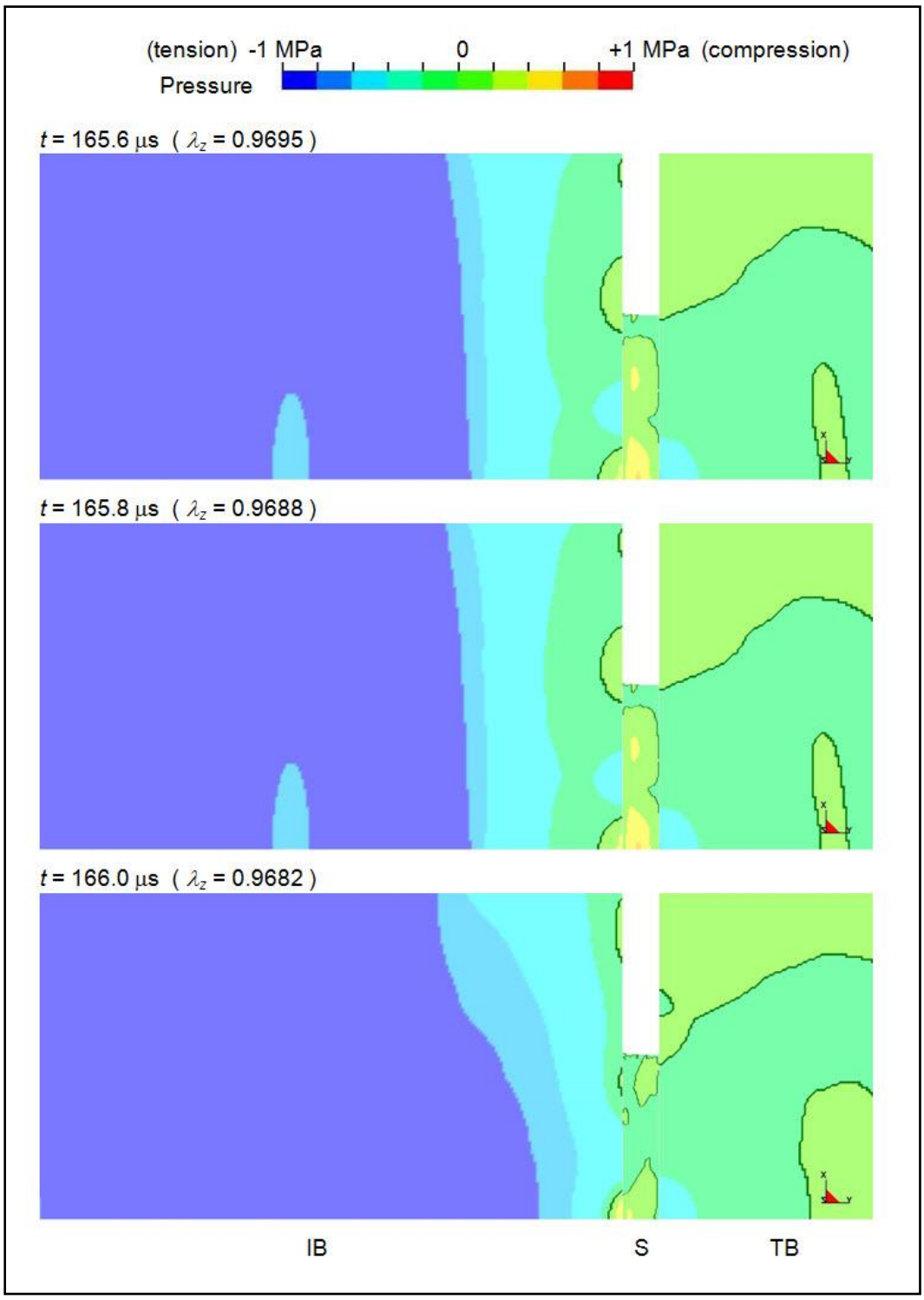

Figure 22. Pressure contours in the vicinity of the specimen at selected times.

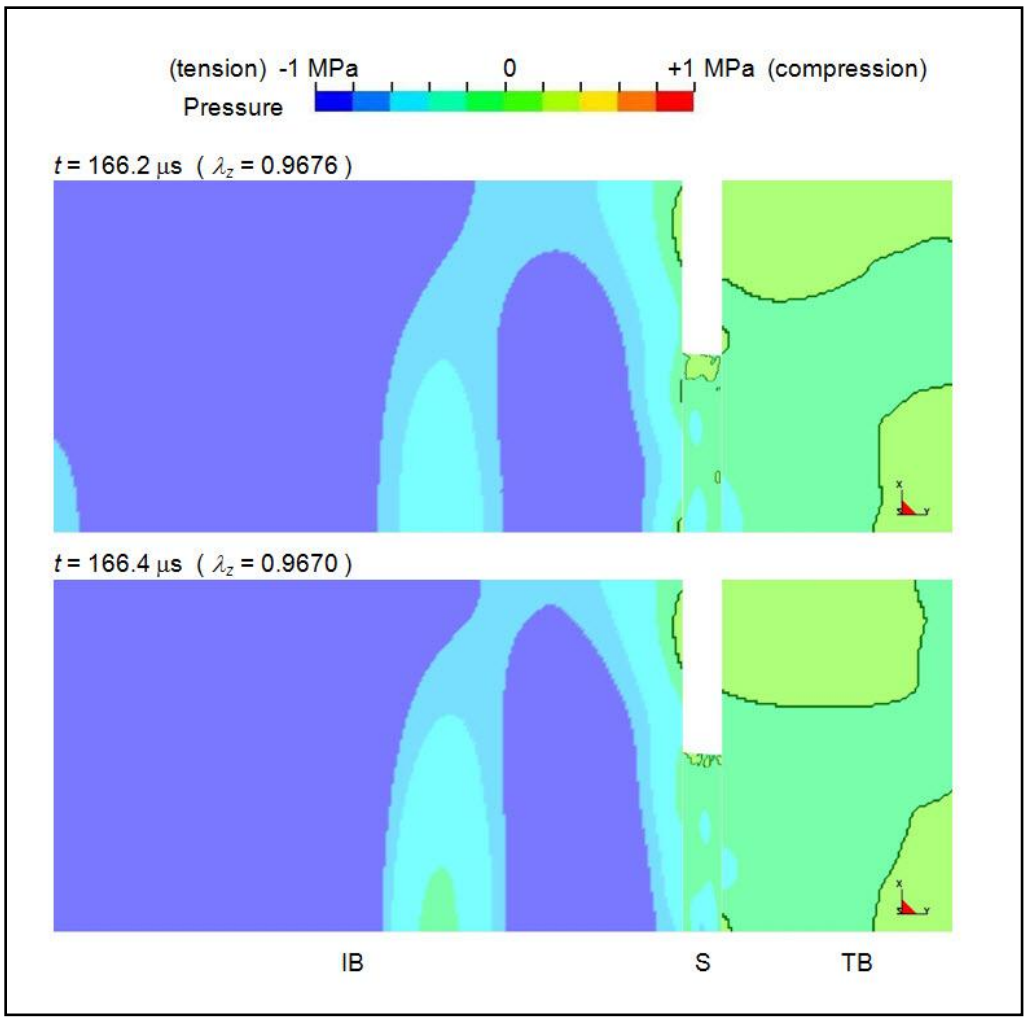

Figure 23. Pressure contours in the vicinity of the specimen at selected times.

Finally, note that at 152 and 162 μs (figure 17), the pressure on the centerline in (and near) the specimen is around 1 MPa. This is consistent with the conclusion that the stress state on the centerline at these instants is nearly hydrostatic (see section 6.1.2). Indeed, from figures 11 and 12, we see that σ_{zz} is about −1 MPa at these times.

6.4 Effects of Pressure Bar Radius on Gap Formation

The results in section 6.3 suggest that the large overhang of the bars (particularly, the incident bar) may contribute to the formation of gaps in the specimen. In order to explore this hypothesis, we reduced the bar radius R_B from 12.8 to 9.5 mm (see section 2.1). The histories of the gap size on the centerline for both cases are compared in figure 24. It is clear that the reduction in the bar radius substantially reduced the size of the gaps at both interfaces at later times.

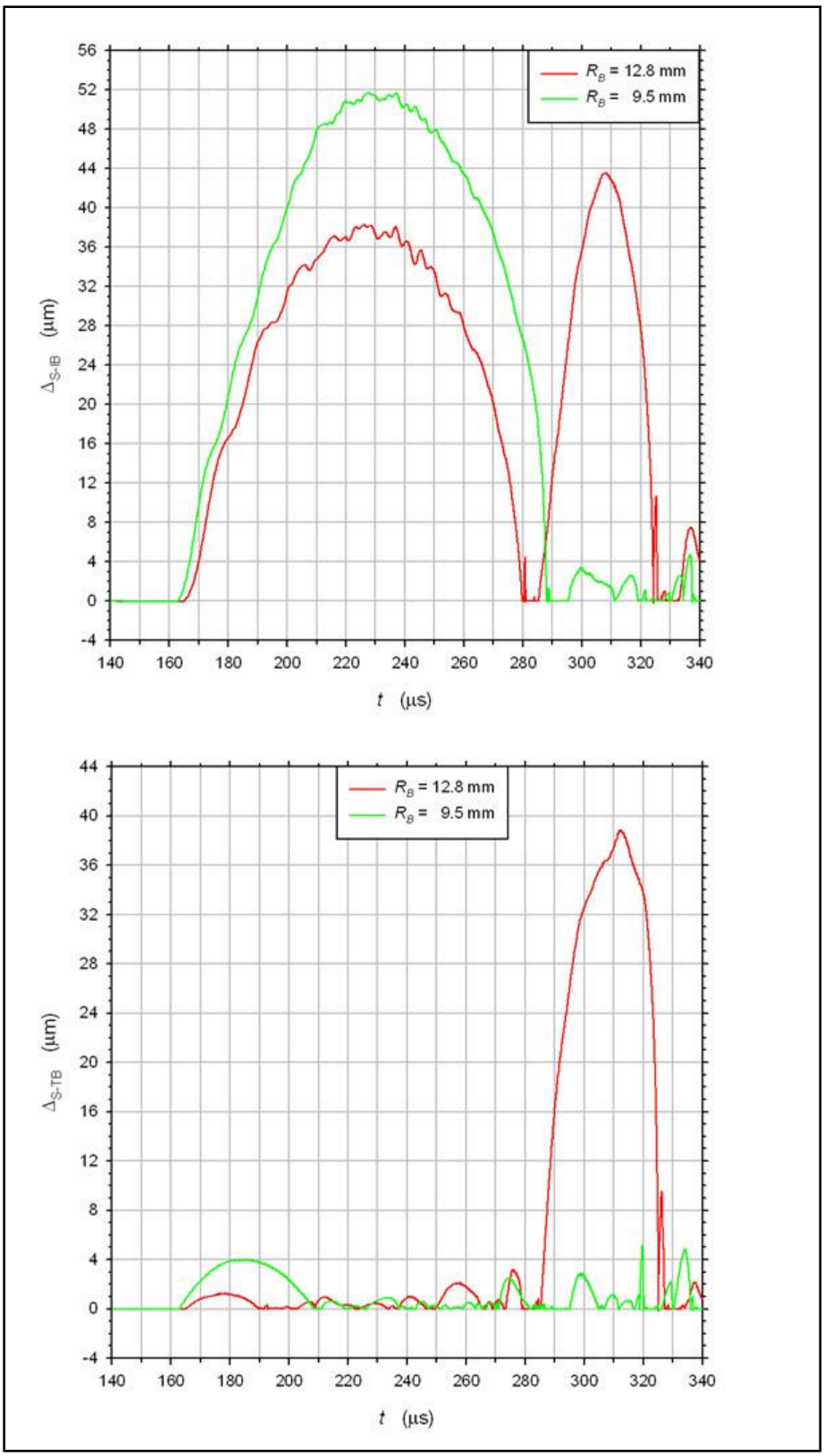

Figure 24. Histories of the gap size on the centerline at the S-IB interface (top) and S-TB interface (bottom) for two different bar radii.

Somewhat surprisingly, however, figure 24 reveals that this reduction in the bar radius increased both the size and the duration of the initial gaps at both interfaces. Also, for the smaller diameter bar, the gaps at both interfaces form about 2 μs earlier. These observations suggest a stronger interaction with the stress-free *lateral* surfaces of the bars, which are now closer to the specimen.

The effect of the bar radius on the formation of gaps for annular specimens is discussed in appendix C-2, but otherwise all results that follow are for the larger radius R_B = 12.8 mm.

---

7. Simulations with the Moony-Rivlin Model and a 25-μs Rise Time

---

All the simulations in this section are for the loading wave with a 25-μs initial rise time and the compressible Mooney-Rivlin model for the specimen. For this case, the axial velocity histories at four locations on the centerline of the incident bar are given in figures 4 and 6. As observed in section 5.3, the velocity history at the S-IB interface for this case (figure 6) is substantially smoother than the corresponding velocity history for the 1-μs initial rise time (figure 5). Recall that the final rise time for the 1-μs case is 24 μs. For the 25-μs initial rise time, the final rise time has increased to about 41 μs. The purpose of this section is to examine the effects of this "pulse shaping" on the formation of gaps.

7.1 Results on the Centerline

All results in this subsection pertain to points on the centerline at the S-IB or S-TB interface. We begin with some remarks about the figures and a few observations, and then proceed to discuss the details of gap formation on the centerline.

7.1.1 General Remarks

Figure 25 compares the gap size histories on the centerline at the S-IB interface for the 1- and 25-μs initial rise times; figure 26 does the same at the S-TB interface. Clearly, the pulse shaping has substantially reduced the size and the duration of the gaps at both interfaces.

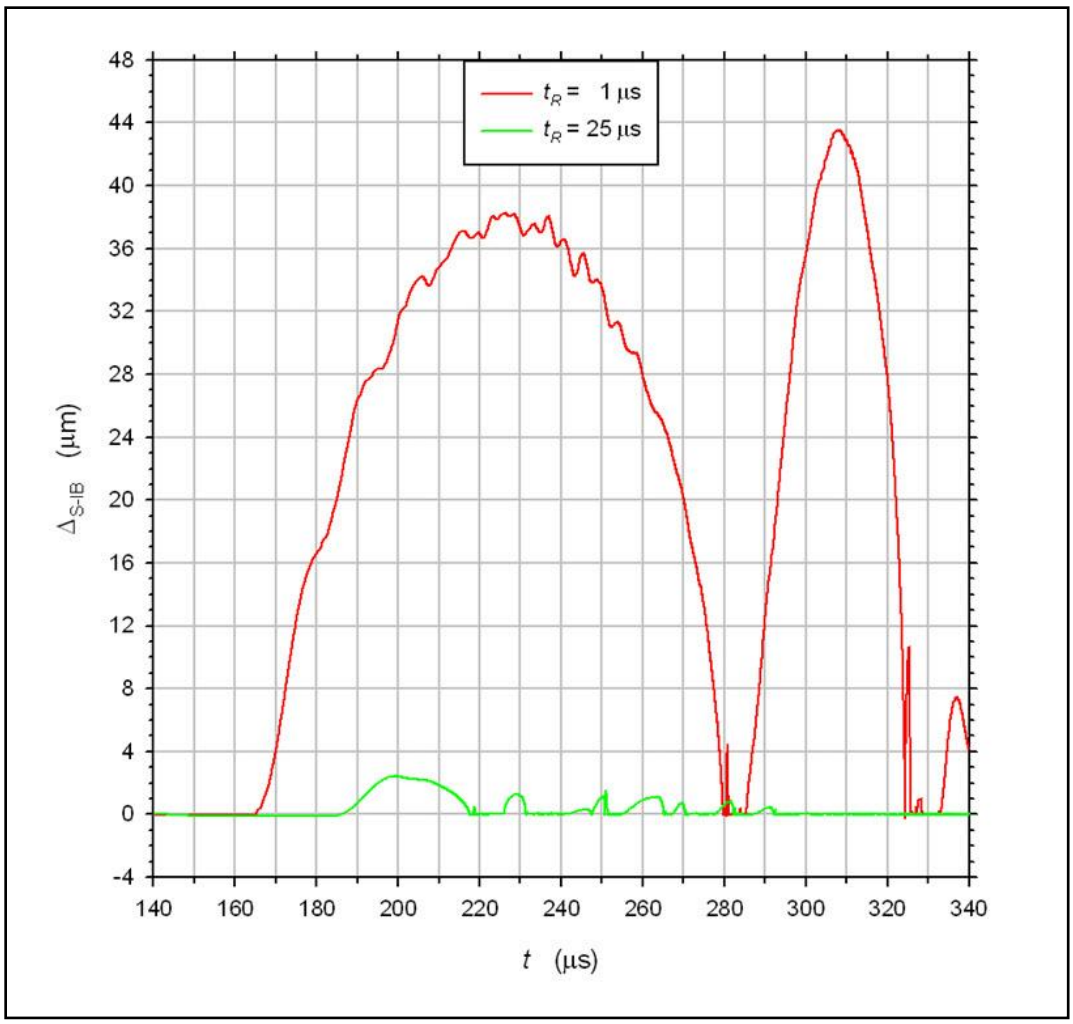

Figure 25. Histories of the gap size on the centerline at the S-IB interface for two loading waves with different initial rise times.

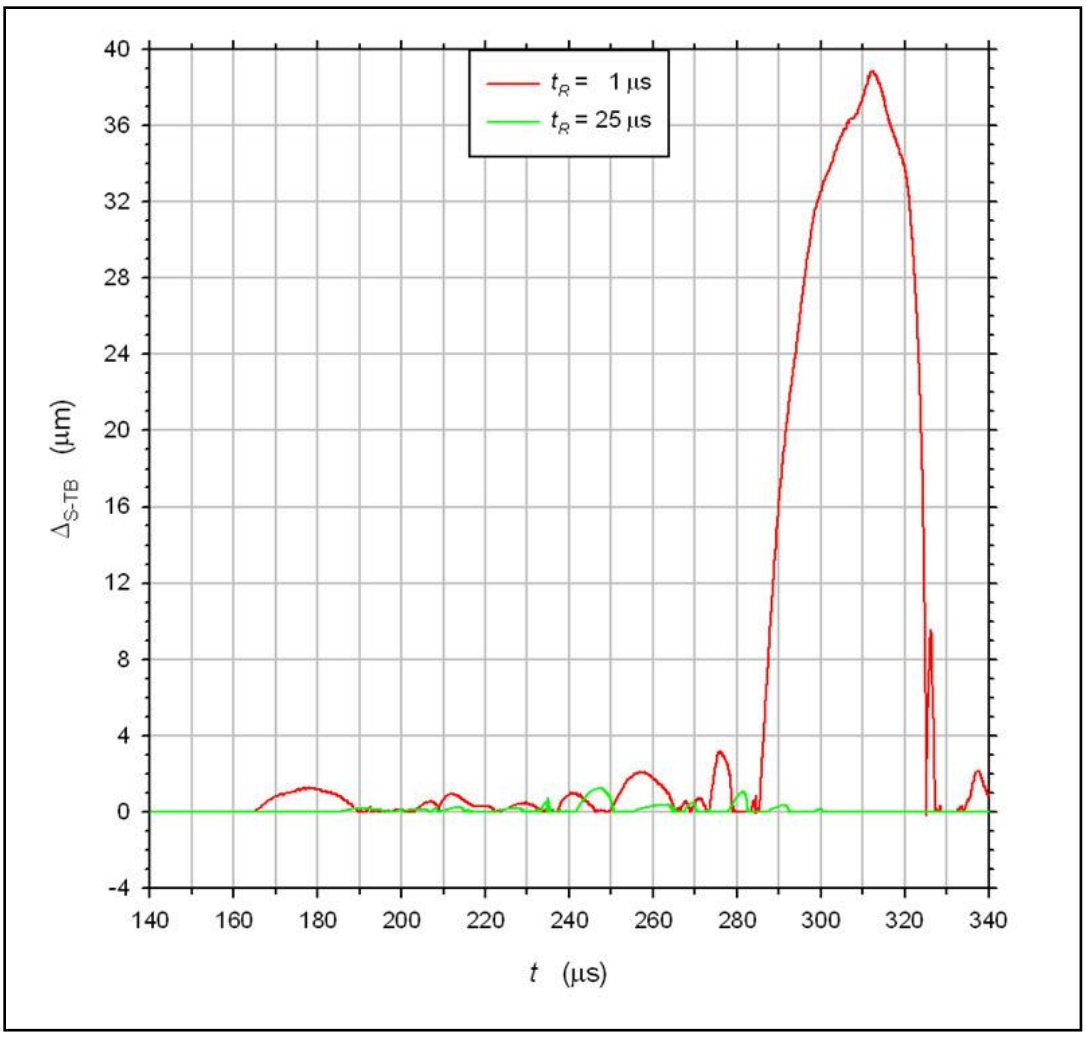

Figure 26. Histories of the gap size on the centerline at the S-TB interface for two loading waves with different initial rise times.

The gap size histories for the 25-μs initial rise time are more easily discernable as the blue curves in figure 27 (S-IB interface) and figure 28 (S-TB interface). The largest gap at the S-IB interface is now only 2.45 μm, while the largest gap at the S-TB interface is now only 1.27 μm. The sensitivity of the gap size histories to the mesh size and the contact algorithm parameters is examined in appendix B. The results described there support the conclusion that the gap phenomenon is not a numerical artifact introduced by the contact algorithm or stemming from an insufficiently fine mesh.

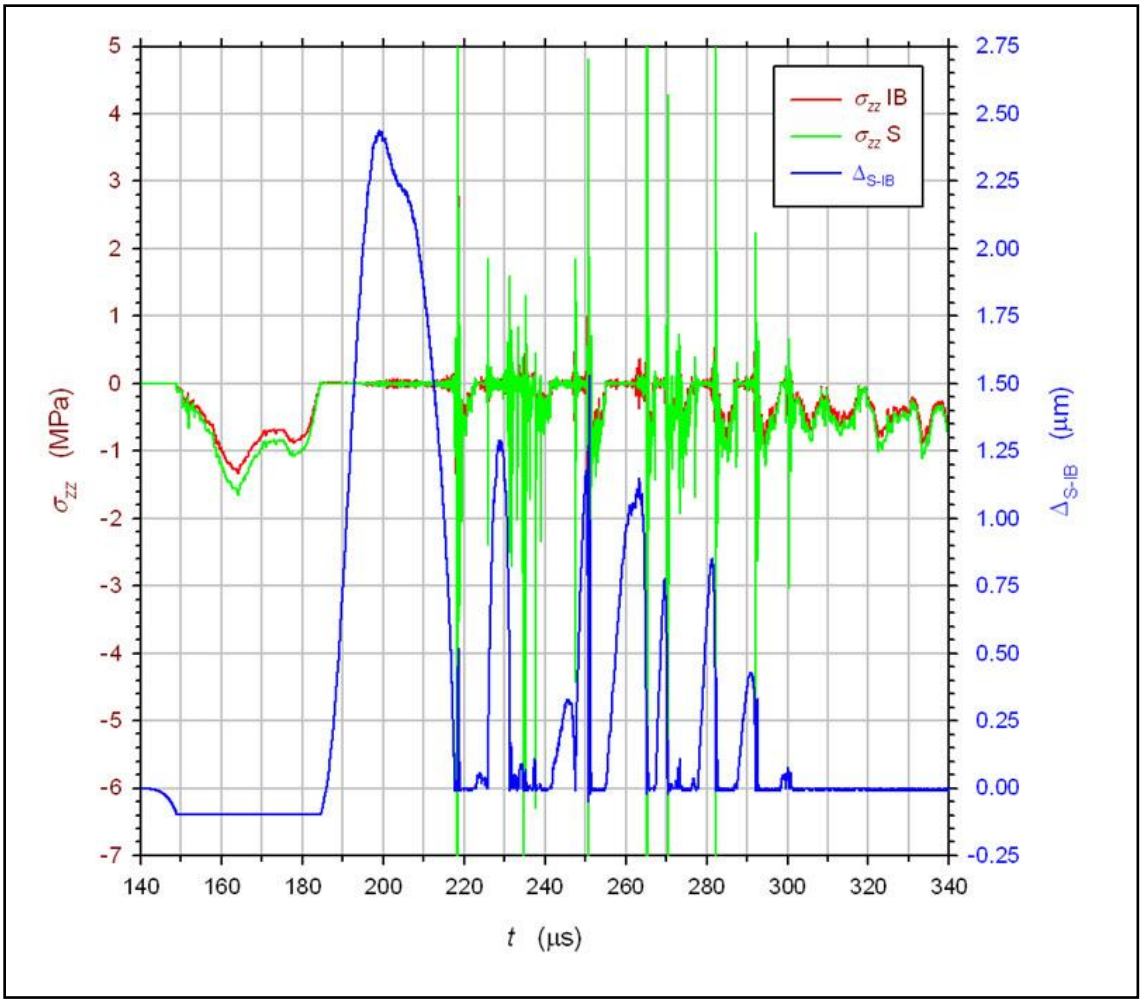

Figure 27. Histories of the axial stress (negative in compression) and the gap size on the centerline at the S-IB interface. The stress is measured at the centroids of the specimen and incident bar elements adjacent to the centerline.

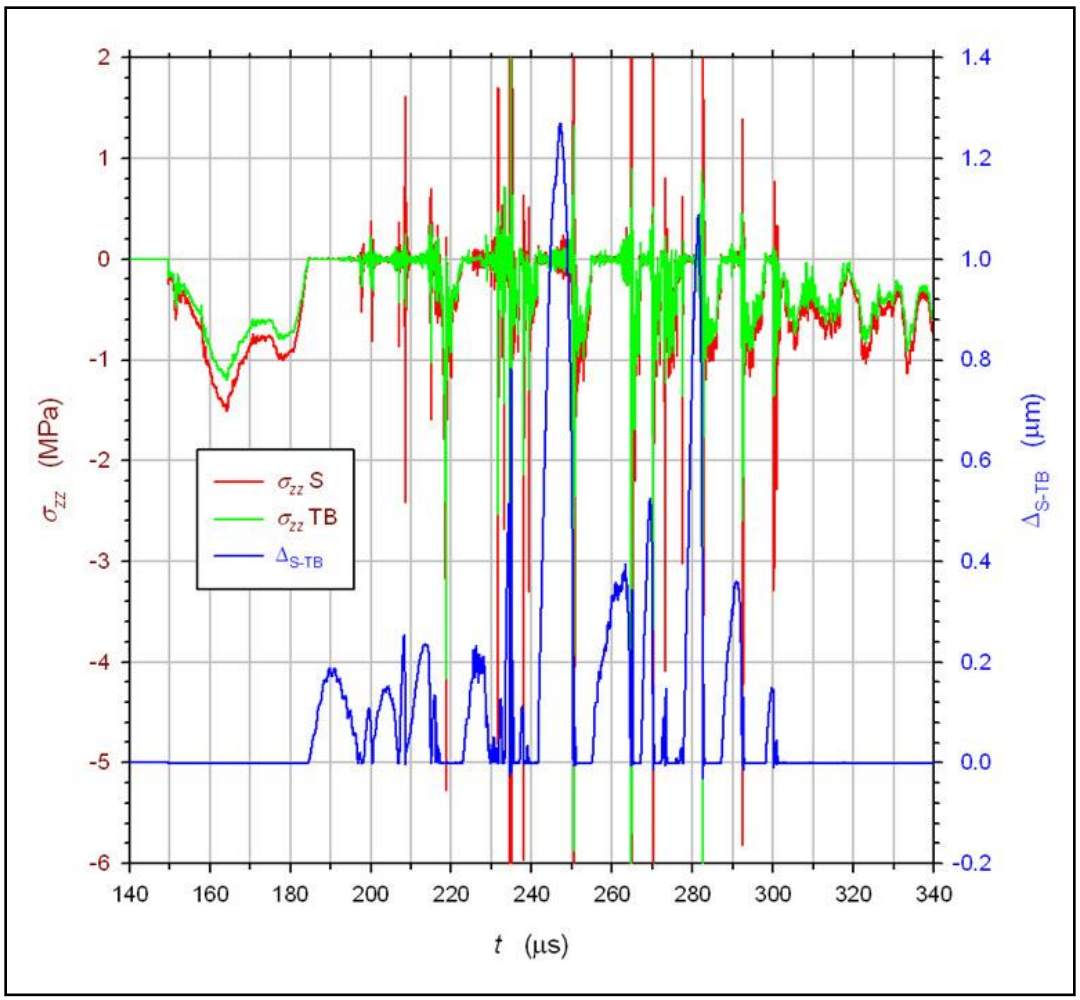

Figure 28. Histories of the axial stress (negative in compression) and the gap size on the centerline at the S-TB interface. The stress is measured at the centroids of the specimen and incident bar elements adjacent to the centerline.

Figure 27 also plots the histories of the axial stress σ_{zz} in the specimen and the incident bar at points near the centerline and the specimen-bar interface. Figure 28 contains an analogous plot at the transmission bar interface. Recall that the stress is actually measured at the centroids of the specimen and bar elements adjacent to the centerline and the interface. Since the coordinates of these centroids do not coincide, slight differences in the values are possible. Also, recall that the axial stress is taken to be negative in compression. As expected, the axial stress is zero or nearly zero[34] when a gap exists, even when the gap is submicron in size. Sharp stress spikes occur when the gap closes and the specimen "slaps" the bar.

We did not plot the mean axial stretch history for the case considered in this section. All stretch (and corresponding strain) values cited below were estimated from the axial stretch history for a

[34] Since the element centroids do not lie on the interface, the axial stress may have a small but nonzero value at the centroid even if it is zero on the face of the element due to the formation of a gap.

linear elastic specimen with a 25-μs initial rise time;[35] see figure 36 in section 8.2. The slope of the axial stretch curve in that figure is constant for $t \geq 190$ μs, and we estimate that the nominal strain rate for these times is about 2490/s.[36] This is within 0.5% of the desired 2500/s strain rate.

A comparison of the velocity history at the S-IB interface in figure 6 with the gap and stress histories in figures 27 and 28 leads to the following additional observations. For convenience of discussion we have divided the time histories into four stages. The first two stages are analogous to those for the 1-μs initial rise time (see sections 6.1.2 and 6.1.3).

7.1.2 The Initial Loading of the Specimen: Stage I (143–184 μs)

This first stage covers the initial loading of the specimen prior to gap formation. It begins with the first significant increase in the axial velocity of the incident bar at the S-IB interface at about 143 μs (see figure 6) and ends with the onset of the first gap at 184 μs. The axial stretch decreases from 1 to about 0.95 over this time 41-μs interval; hence, the nominal axial strain increases from 0% to about 5%.

The first observable increase in axial stress occurs at about 149 μs at the S-IB interface and 150 μs at the S-TB interface. The stress in the specimen increases to a sharp peak of −1.6 and −1.5 MPa at the S-IB and S-TB interfaces, respectively, at about 164 μs. Thereafter, the stress at both interfaces decreases to a broad local minimum centered at about 173 μs, then increases again to a local maximum around 177–178 μs, and finally decreases to zero at 184 μs. The axial stress at this second (minor) peak is −1.1 and −1.0 MPa at the S-IB and S-TB interfaces, respectively. Smaller oscillations are superimposed on this general behavior.

The axial stretch at 164 μs, the time of the first (major) peak in stress, is about 0.99. Since this is the same value of the stretch at the stress peak for the 1-μs initial rise time (section 6.1.2), we conclude that at this instant, $\sigma_{zz} - \sigma_{rr} \approx -2.4$ kPa and $\sigma_{\theta\theta} = \sigma_{rr}$. However, as noted above, $\sigma_{zz} \approx -1.5$ MPa. Hence, the differences between the principal stresses σ_{rr}, $\sigma_{\theta\theta}$, and σ_{zz} are either zero or nearly three orders of magnitude smaller than the stresses themselves. It follows that all three principal stresses are nearly equal to each other and, hence, to $-p$. That is, the stress state is nearly hydrostatic.

While the preceding quantitative estimates apply only at the stress peak, similar calculations at neighboring times lead to the same qualitative conclusion: the stress state is nearly hydrostatic for most of this stage, as opposed to the desired state of uniaxial stress.

A close examination of the axial velocity history of the incident bar at the specimen interface (figure 6) reveals that the extrema in the axial stress in the specimen at 164, 173, and 177–178 μs coincide (at least approximately) with inflection points in the velocity vs. time curve, that is, with

[35] Recall that the mean axial stretch is computed from equation 8. Because of the low impedance of the specimen for both models, the displacements and hence the mean stretches for these two cases should be close.

[36] We get essentially the same value using the approximation for the nominal strain rate in equation 10, together with $v_{IB} = 1.99\ v_0$, which is the mean value for the velocity of the incident bar at later times, estimated from figure 6.

extrema in the axial acceleration vs. time curve. Similarly, as the acceleration decreases towards zero after 178 μs, so does the axial stress. Thus, just as for the case of the 1-μs initial rise time (section 6.1.2), it seems likely that during this stage, the value of the axial stress and the nearly hydrostatic stress state in the neighborhood of the stress peak are inertial effects associated with the accelerations imposed on the specimen by the incident bar.[37] Furthermore, since the axial stresses at either face are nearly equal, we may conclude that the axial stress is approximately uniform through the thickness of the specimen (at least on the centerline), so these would appear to be primarily radial inertia effects.

The preceding conclusion is reinforced by comparing the peak stresses and accelerations for the two different rise times. The peak axial stress at the S-IB interface for the 1-μs case (−4.0 MPa) is about 2½ times the peak stress (−1.6 MPa) for the 25-μs case. From the velocity histories in figures 5 and 6, we can obtain rough estimates for the axial accelerations of the incident bar at the time of these peak stresses. We find that the acceleration for the 1-μs case is between 2½ to 3 times that for the 25-μs case. Thus the peak axial stress in this early stage increases in (rough) proportion to the peak axial acceleration. Song et al. (*6*) reached a similar conclusion from their numerical simulations of SHPB tests on gel rubber specimens. This conclusion is also consistent with various theoretical analyses of inertial effects for soft materials (*26–33*).

7.1.3 Gap Opening and Closure (Stages II–IV)

Stage II (184–218 μs): This stage begins with the opening of the first gap, which occurs at the S-TB interface, and ends with the first closing of the gap at the S-IB interface. During this 34-μs time interval, the axial strain increases from 5% to about 14%. Note that the duration of this stage is about a third of the duration of Stage II for the case of a 1-μs initial rise time, and gap formation occurs about 20 μs later than it did for the 1-μs case.

The axial stress at both interfaces drops to zero at about 184 μs. The gap at the S-TB interface forms at this time, whereas the gap at the S-IB interface forms about 2 μs later. Analogous to the case for the 1-μs initial rise time, the contact algorithm allowed a 0.10-μm interpenetration at the S-IB interface prior to gap formation. This interpenetration begins to decrease at about 184 μs. From figure 6, we see that the peak in the axial velocity of the incident bar at the S-IB interface also occurs at 184 μs. The axial acceleration of the bar is zero at this instant and then becomes negative for some time thereafter.

This stage ends with the first closing of the gap at the S-IB interface at about 218 μs. The gap at the S-TB interface is also closed at this instant, although it has opened and closed several times previously. Nevertheless, it is open for most of this stage. The largest gap size at the S-IB interface (but not at the S-TB interface) is attained during this stage: about 2.45 μm at 200 μs.

[37] In this regard, see the comments in the next to last paragraph in section 5.3.

Stage III (218–302 μs): This stage begins with the first closing of the gap at the S-IB interface, which produces large spikes in the axial stress at both interfaces (figures 27 and 28) and a large spike in the axial velocity at the S-IB interface (figure 6). Subsequently, the gaps at both interfaces open and close many times, again with large spikes in stress and velocity corresponding to gap closure. This stage ends with the permanent closing of the gaps at both interfaces at about 302 μs. During this 84 μs time interval, the nominal axial strain increases from 14% to 34%. The largest gap at the S-TB interface occurs during this stage: 1.27 μm at $t = 247$ μs.

Stage IV (302–340 μs): The gaps at both interfaces close and remain closed during this final stage. The axial stress oscillates (without spikes) about a steadily increasing mean value. There is no analog of this stage for the case of a 1-μs initial rise time, at least for times less than 340 μs.

During Stage IV, the axial stretch λ_z decreases monotonically from 0.66 to 0.57, and hence the nominal axial strain increases from 34% to 43%. From equation A-3 and the values of A_1 and A_2 in table 3, we find that for this range of λ_z, $-\sigma_{zz}$ would increase monotonically from about 117 kPa to 175 kPa *if the stress state were uniaxial* (see also figure A-1). However, from figures 27 and 28 we see that in fact $-\sigma_{zz}$ oscillates between 0 and 1.1 MPa during this stage, with an average value around 0.5 MPa = 500 kPa. Hence, the specimen is not in a state of uniaxial stress during this stage. Indeed, using equation A-14 and arguing as in section 6.1.2, we conclude that for most Stage IV, the stress state is closer to hydrostatic than it is to uniaxial.

7.2 Gap Size vs. Radius at Selected Times

Figure 29 plots the gap size vs. deformed specimen radius at the S-IB interface at selected times. There is no gap at any radial location for times less than or equal to 185 μs. Also, note the 0.10 μm interpenetration allowed by the contact algorithm at the S-IB interface prior to gap formation.

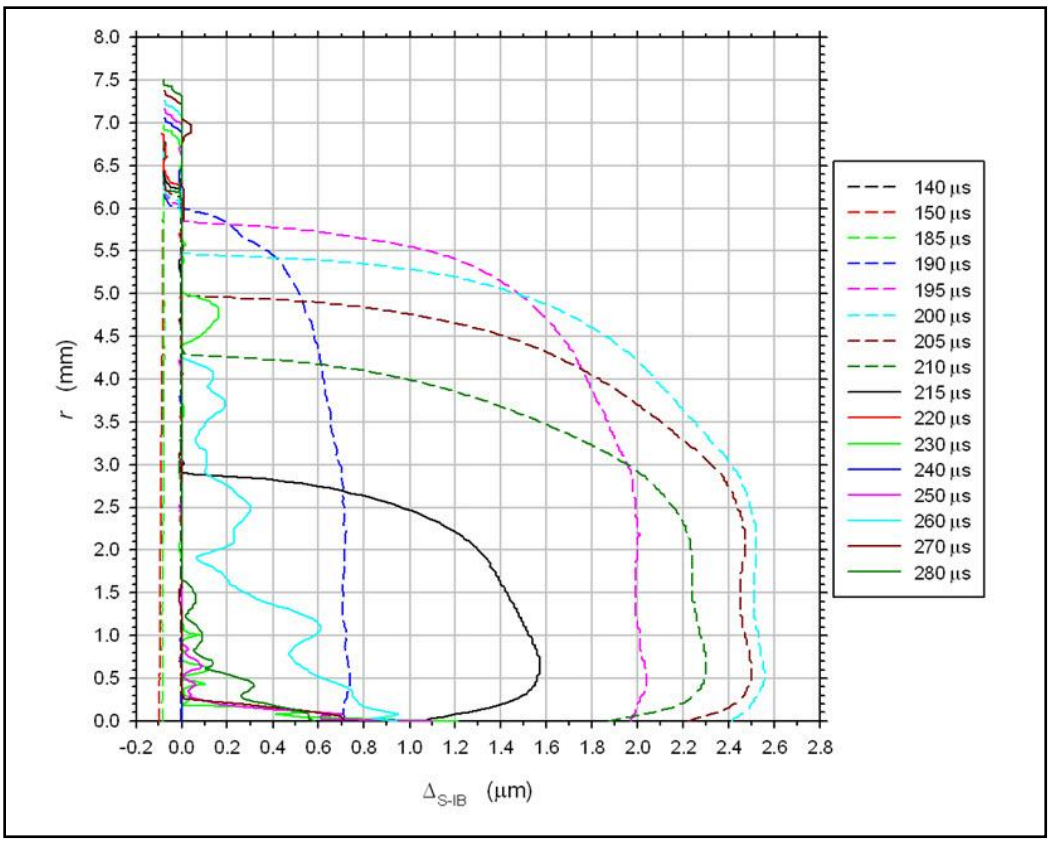

Figure 29. Gap size vs. deformed specimen radius at the S-IB interface at selected times.

At 190 μs, the gap extends along most of the face of the specimen. Thereafter, the radial extent of the gap decreases with time. By 215 μs, the gap extends only 3 mm out from the centerline, which is slightly less than half the radius. The maximum gap size increases with time up to 200 μs and then decreases with time until about 220 μs, when the gap appears to close temporarily. Also, note that at each instant from 190–215 μs, the maximum size of the gap occurs off the centerline. From 230 μs onward, gap opening and closing exhibits a more complicated radial and temporal behavior. The results in figure 29 are consistent with the those on the centerline in figures 25 and 27.

7.3 Force History in the Transmission Bar

Figure 30 is somewhat similar to figure 28; in particular, the history of the gap size on the centerline at the S-TB interface is repeated in figure 30. But instead of plotting the axial stress in the transmission bar at a point very near the S-TB interface, figure 30 plots the total axial force F_z acting on the cross-section of the transmission bar at an axial location 2.52 mm from the specimen-bar interface. This is about 25 bar elements back from the interface. Also, note that F_z has been taken positive in compression, whereas σ_{zz} in figure 28 is positive in tension.[38]

[38] When comparing figures 28 and 30, keep in mind that the colors of the stress-force curves and the gap size curves have been switched, as have the left-right locations of the vertical axes.

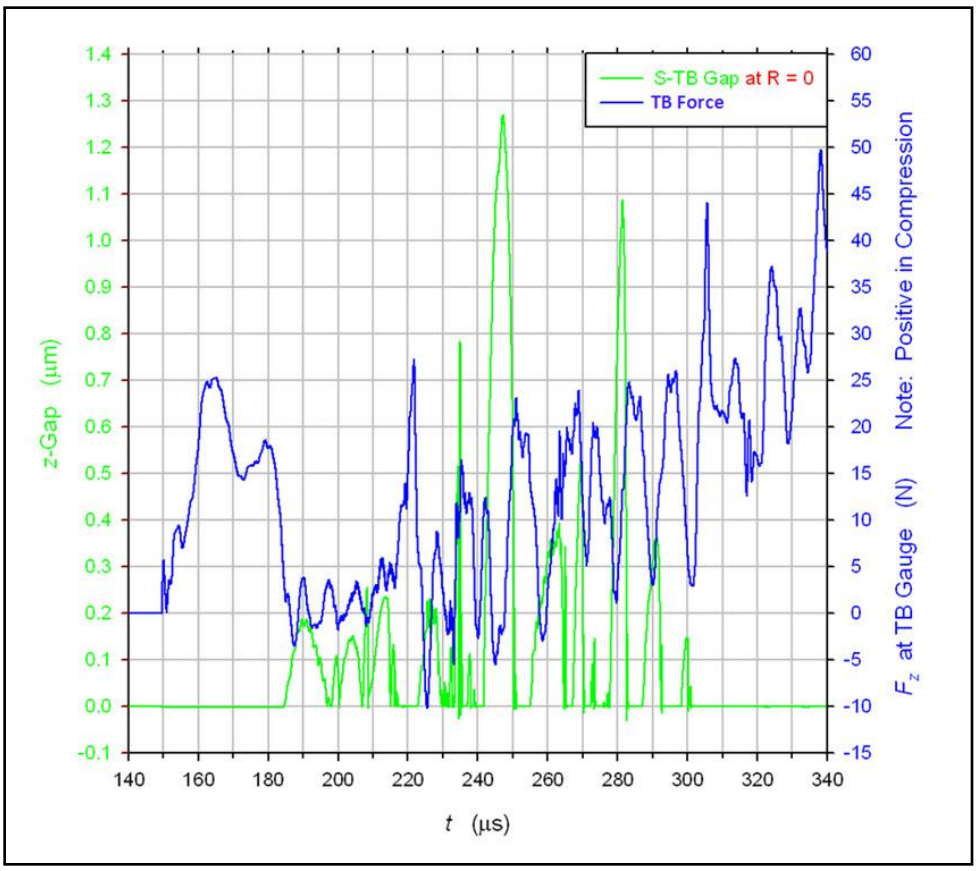

Figure 30. History of the total force (positive in compression) at the stress gage location in the transmission bar (2.52 mm from the specimen interface) compared with the history of the gap size on the centerline at the S-TB interface.

On taking the difference in the sign conventions into account, we see (not unexpectedly) that the force history in figure 30 is qualitatively similar to the stress history in figure 28. In particular, the force is positive from 150 to 186 μs, corresponding to the Stage I loading discussed in section 7.1.2, and the timing of the local maximum and minimum values of F_z and σ_{zz} coincide during this stage. A gap opens and closes repeatedly at the centerline starting at 184 μs; subsequently, the total force oscillates with repeated dips below zero (i.e., a tensile force). This continues until about 260 μs, after which the force remains positive and oscillates about a steadily increasing mean value.

When comparing the force and gap histories in figure 30, it should be kept in mind that the total force is the cumulative effect of the stress at all radial locations in the transmission bar, whereas the gap has been measured only on the centerline. Nevertheless, from 184 to 302 μs (Stages II and III in section 7.1.3), the local maximum and minimum values of the total force coincide, for the most part, with the closure and opening, respectively, of a gap on the centerline. In particular, the times at which the total force becomes tensile coincide with gaps, for the most part. It seems reasonable to conclude that when a gap exists on the centerline at the S-TB

interface, it extends over a significant portion of the specimen face, although we do not have any plots (analogous to figure 29) to verify this.

The force in the transmission bar in figure 30 is measured at an axial location 2.52 mm from the specimen-bar interface. This location was selected because it is typical for the placement of a quartz stress gage in the bar in SHPB tests (Casem et al. [*25*]). Hence, we refer to this axial location as the gage location, even though a stress gage was not included in the simulation. The signal from a quartz gage is proportional to the total force applied to it, regardless of whether or not the axial stress in the transmission bar is radially uniform (*25*). With appropriate calibrations, the force measured by a quartz gage should also coincide with the force inferred from semi-conductor strain gage measurements midway down the bar; see Moy et al. (*5*) for the case of a ballistic gelatin specimen.

In view of the proximity of the gage location to the S-TB interface, we expect that the force on the transmission bar at the specimen interface may be approximated by the force at the gage location, with some qualifications (see below). Hence, keeping in mind the sign conventions and letting A_0 denote the *original* cross-sectional area of the specimen, we see that $-F_z/A_0$ provides an estimate for the average or mean value of the axial component of the nominal stress in the specimen.[39] Similarly, $\bar{\sigma}_{zz}$, the mean value of the true axial stress σ_{zz} in the specimen, is estimated by dividing $-F_z$ by the deformed cross-sectional area of the specimen, which in turn is approximated by A_0/λ_z,[40] so that $\bar{\sigma}_{zz} \approx -\lambda_z F_z/A_0$. These estimates for the mean value of the nominal and true axial stress in the specimen are consistent with those used in reporting data in the SHPB literature.

Let us apply this estimate for $\bar{\sigma}_{zz}$ to the first peak in F_z at 164-165 μs, which is prior to gap formation. The force at this instant is 25 N, λ_z is about 0.99 (see section 7.1.2), and the undeformed specimen radius is 6.35 mm, which gives $\bar{\sigma}_{zz} \approx -0.20$ MPa = –200 kPa. This is almost two orders of magnitude above the value of –2.4 kPa that would correspond to a state of uniaxial stress at this axial stretch. On the other hand, the axial stress σ_{zz} on the centerline at the S-TB interface at this instant is –1.5 MPa (section 7.1.2), which is 7–8 times the estimated mean stress. Hence, if this estimate for the mean stress is valid (at least approximately), then the axial stress must be radially non-uniform, with higher values near the centerline. This qualitative behavior is consistent with theoretical analyses of radial inertia effects for soft materials (*7, 26, 27, 32, 33*) and with the results of other numerical simulations of SHPB tests (*6, 34*).

For early times, the force history in figure 30 is qualitatively similar to the mean nominal stress histories on solid specimens in figure 3 of Moy et al. (*5*) and figure 5 of Song et al. (*6*). The latter two figures report experimental SHPB data on a ballistic gelatin specimen and a gel rubber specimen, respectively. All three figures show a large "inertial spike" at small strains and early

[39] This is also referred to as the engineering stress. It is the *zz*-component of the 1st Piola-Kirchhoff stress tensor.

[40] This approximate relation is exact when the axial stretch in the specimen is uniform and there is no volume change.

times (165 μs in figure 30). In Moy et al. (*5*) and Song et al. (*6*) it is demonstrated that this inertial spike can be substantially reduced by hollowing out the specimen, the rational being that radial inertia contributions to the axial stress are largest in the center of the specimen (cf. the preceding paragraph). Unlike figure 30, the experimental data in Moy et al. (*5*) does not exhibit the large oscillations or any evidence of gap formation after the inertial spike. This is not surprising in view of the fact that the pulse shaping in those tests resulted in a much smoother loading wave than the one used in our simulation. On the other hand, the entire force history in figure 30 is qualitatively similar to nominal stress history for the solid specimen in figure 5 of Song et al. (*6*), for which no pulse shaping was used. These similarities include the oscillations and the dips to negative (i.e., tensile) forces following the inertial spike. Thus the data in Song et al. (*6*) may be exhibiting indirect evidence of gap formation at the S-TB interface, although the possibility of gaps was not discussed in that paper.[41]

Based on the discussion above and on the previous discussion of the histories of the stress, velocity, and gap size on the centerline for both the 25- and 1-μs initial rise times, the following conclusions seem plausible. Not only is the inertial spike a radial inertia effect, but so also is the reduction from this large compressive stress to zero axial stress, even though the specimen is subject to compressive axial strain. This reduction to zero axial stress is driven by the rapid drop in the axial acceleration of the incident bar to (and below) zero. Once the axial stress at the interface drops to zero,[42] a gap can form there. For cases with more gradual deceleration via better pulse shaping, as in Moy et al. (*5*), there is a less severe drop in stress that never reaches zero before the stress begins to increase again.

Finally, it should be kept in mind that when a gap exists over a substantial portion of the face of the specimen, the contact area between the specimen and the bar is reduced, so the local value of the axial stress in the specimen is magnified at those points in contact with the bar, whereas it is zero at points on the specimen face where a gap has formed. Consequently, in this case the mean axial stress computed as above does not provide a meaningful estimate of the highly non-uniform stress state in the specimen. Furthermore, differences between the force at the gage location and the force at the S-TB interface could arise due to axial acceleration of the transmission bar near the interface (*25*). This acceleration is often regarded as negligible (based the assumption that the transmitted pulses are weak), but it must be significant at least part of the time in the present

---

[41] The stress history at the S-TB interface in Song et al. (*6*) was inferred from strain gages mounted on the transmission bar. Similarly, the stress history at the S-IB interface in a SHPB test can be inferred from strain gages mounted on the incident bar. Large stress oscillations and tensile stresses are also seen in some incident bar strain gage data on soft materials; cf. figure 6 (lead) in Gray (*1*) and figure 2 (estane-based polymer binder) in Gray and Blumenthal (*3*). This could be indicative of gap formation at the S-IB interface. However, the estimate for the stress at the S-IB interface based on 2-wave calculations from strain gage data is subject to larger uncertainty than the estimate for the stress at the S-TB interface; cf. Gray (*1*), Gray and Blumenthal (*3*), and Chen et al. (*35*). Quartz gages were used to measure force histories in the incident and transmission bars in SHPB tests on RTV 630 silicone rubber in Chen et al. (*35*). Large stress oscillations and tensile stresses are seen in the incident bar data here as well (figures 6 and 8); and some of the transmission bar data shows less frequent and smaller amplitude dips to tensile stress. These results could be indicative of gap formation at both interfaces. However, the authors point out that the specimen may have failed in some of these tests, and this possibility complicates the interpretation of the data.

[42] Note that tensile axial stresses cannot be transmitted across the specimen-bar interface.

case. Indeed, the tensile forces at the gage location at various times between 186 and 260 μs cannot possibly represent the force at the S-TB interface, since tensile forces cannot be transmitted across the interface: the force on exerted on the transmission bar by the specimen (and hence, on the specimen by the transmission bar) must be compressive (positive) or zero.

8. Simulations with a Linear Elastic Model for the Specimen

For all of the results presented up to this point, the compressible Mooney-Rivlin model was used for the specimen. Recall that this is a nonlinear elastic constitutive model that was calibrated to yield a nearly incompressible material (see section 3 and appendix A). The question naturally arises as to whether the nonlinearity in the material response and the near incompressibility of the material are necessary for the formation of gaps or for the persistence of the gaps once they form. The simulations in this section address these issues by replacing the Mooney-Rivlin model for the specimen with an isotropic, linear elastic model and by varying the Poisson's ratio for that model.[43]

We used LS-DYNA's Orthotropic Elastic model (Material Model 2 in LS-DYNA [*8*] and Hallquist [*9*]) for the specimen, with the material constants chosen in such a way as to yield an isotropic, linear elastic model. For all of the simulations in this section, the Young's modulus E was fixed at 0.43 MPa, which is slightly less than twice the initial value of the Young's modulus used for the Mooney-Rivlin model (see table 1). The density of the specimen remained the same (1 g/cm^3). Six different values of the Poisson's ratio ν were used in the simulations, ranging from 0.49999 to 0.48. The largest value, $\nu = 0.49999$, is the same value used for the compressible Mooney-Rivlin model. The six values for Poisson's ratio as well as the corresponding values of the other elastic constants determined from E and ν are listed in table 1. Note that as Poisson's ratio decreases from 0.49999 to 0.48, the bulk modulus K and the longitudinal modulus L (which are nearly identical) decrease by a factor of 2000, whereas the changes in the shear modulus G are insignificant; the ratio of the shear to bulk modulus, G/K, which is a measure of incompressibility (see section 2.3), increases from 0.0002 to 0.04.

8.1 The 1-μs Initial Rise Time

Figures 31–35 present results for the loading wave with a 1-μs initial rise time. Figure 31 compares the histories of the gap size on the centerline at the two interfaces for the case $\nu = 0.49999$. Also plotted in that figure (right axis) is the history of the axial stretch λ_z; see equation 8. Clearly, nonlinearity in the constitutive model is not required for the formation of a gap or for the persistence of the gap out to large strains. The gap forms at about 165 μs (3% nominal strain). The gap at the S-IB interface remains open for a substantial time interval,

[43] The elastic constants used in these simulations are not necessarily those appropriate for the small strain response of ballistic gelatin.

eventually closing at about 263 μs (27% nominal strain). The S-TB gap is also closed at this time, but has opened and closed several times prior to that, and the size of the gap at the S-TB interface during this first stage is substantially less than at the S-IB interface. All of these features are qualitatively similar to those observed for the nonlinear model (see section 6.1).

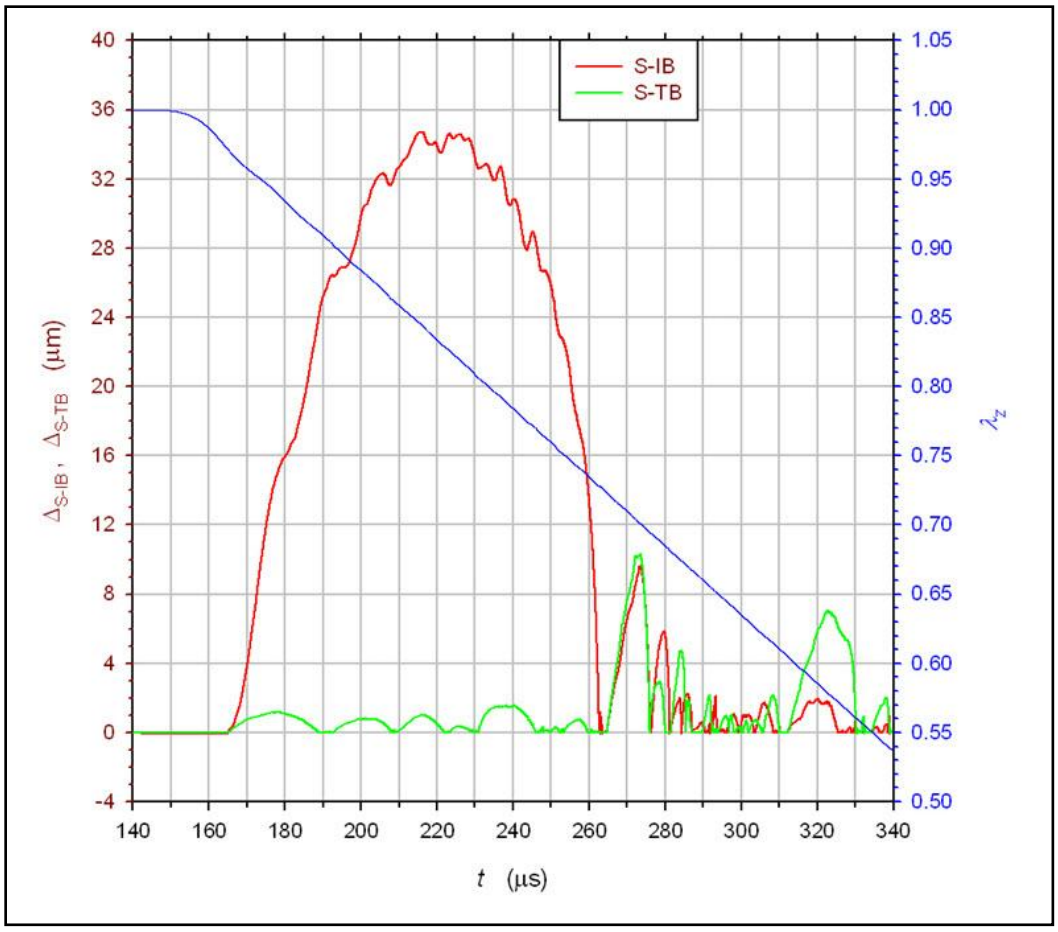

Figure 31. A comparison of the histories of the gap sizes on the centerline at the S-IB and S-TB interfaces for a 1-μs rise time and $\nu = 0.49999$ (linear elastic model). Also shown is the history of mean axial stretch in the specimen (blue).

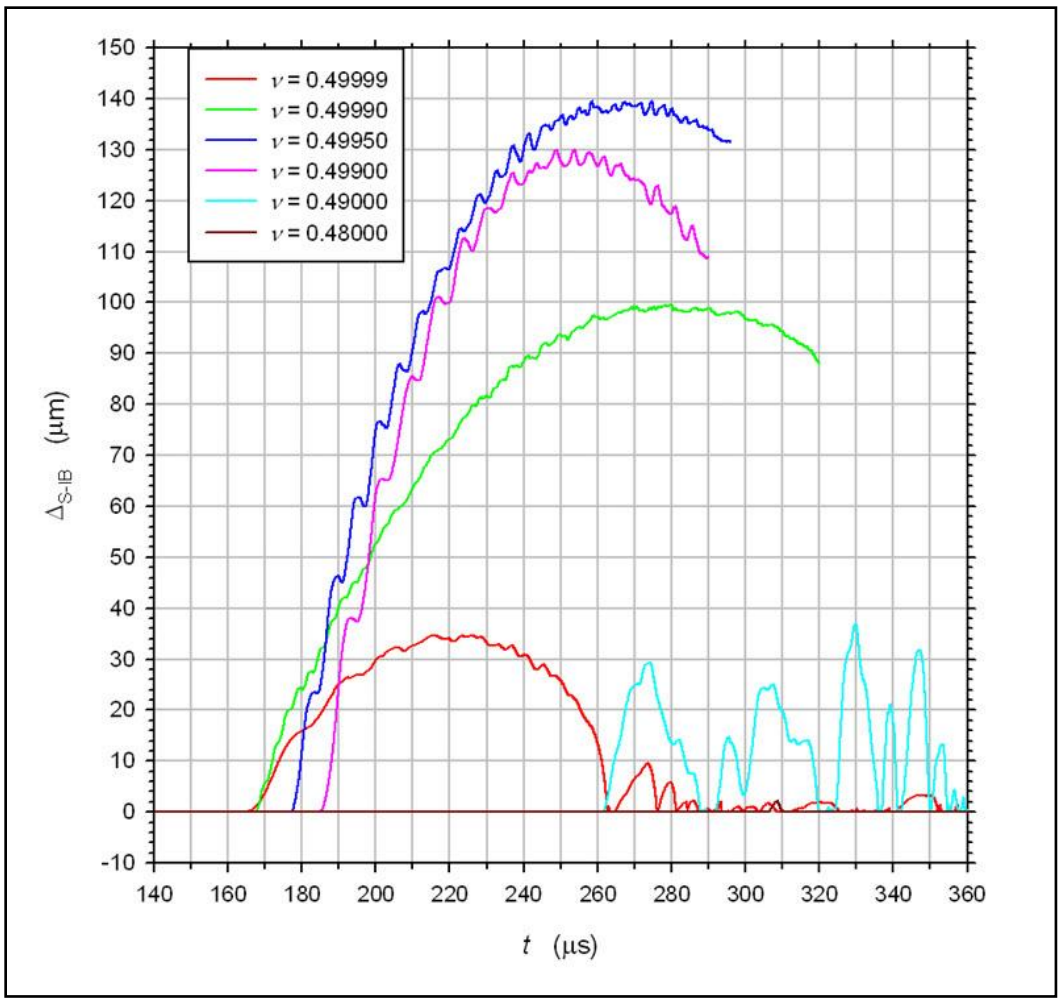

Figure 32. A comparison of the histories of the gap sizes on the centerline at the S-IB interface for a 1-μs rise time and selected values of Poisson's ratio (linear elastic model).

Figure 32 compares the histories of the gap size on the centerline at the S-IB interface for the six values of Poisson's ratio. Figure 33 does the same at the S-TB interface. Gaps form at both interfaces for $\nu \geq 0.49$, that is, for $G/K \leq 0.02$. But they do not form at either interface for the lowest value of Poisson's ration, $\nu = 0.48$, that is, for $G/K = 0.04$. Thus it appears that the specimen must be nearly incompressible in order for gaps to form.

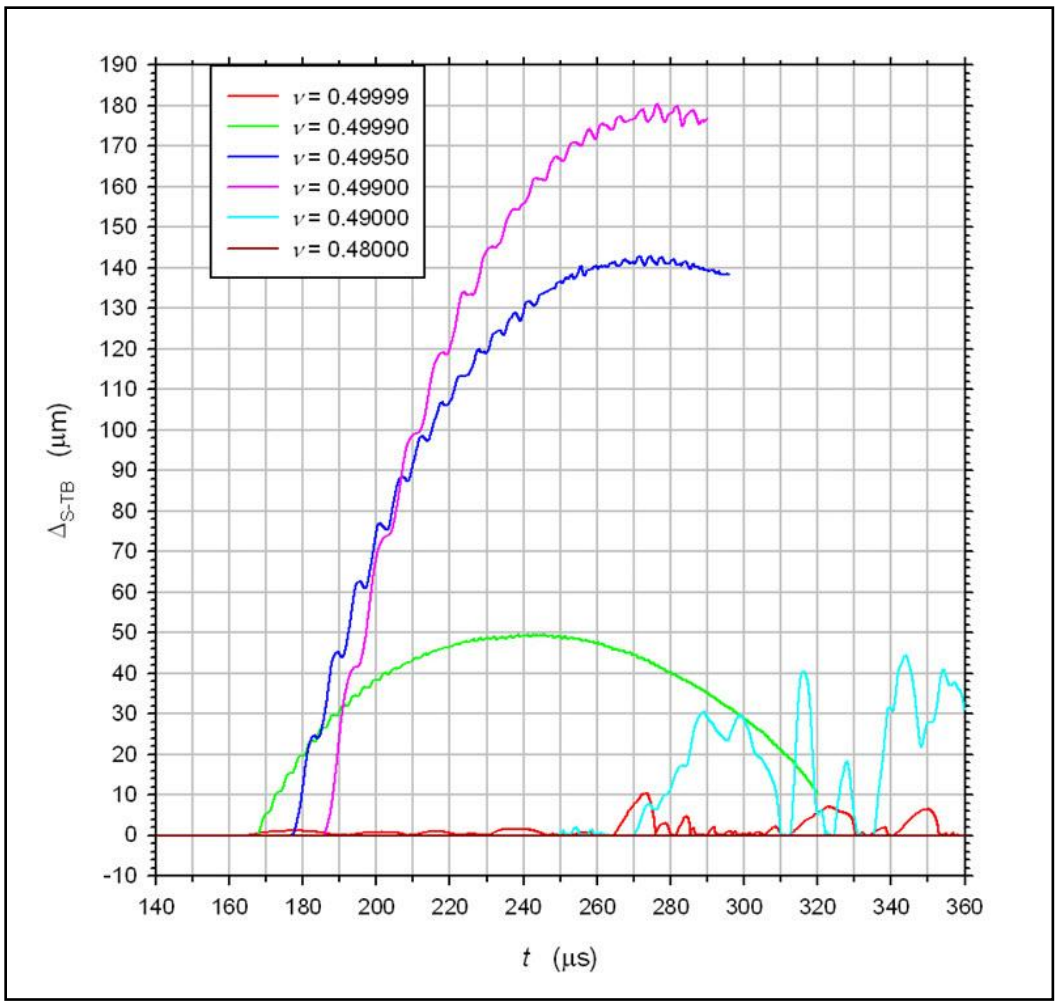

Figure 33. A comparison of the histories of the gap sizes on the centerline at the S-TB interface for a 1-μs rise time and selected values of Poisson's ratio (linear elastic model).

The three values of Poisson's ratio that resulted in the largest gap sizes at both interfaces were 0.499, 0.4995, and 0.4999. Note that the corresponding gap histories in figures 32 and 33 do not extend all the way to 360 μs. We terminated these histories prior to that time because the specimen elements in direct contact with the bar exhibited hourglassing. The gap size curves in the figures were terminated well before this occurred.

It is interesting to note that the maximum value (over the duration of the simulation) of the size of the gap at the centerline does not vary monotonically with Poisson's ratio. Figure 34 plots this maximum gap size at each interface as a function of Poisson's ratio ν. At the S-IB interface, the maximum gap size increases with ν up to a maximum of 140 μm for ν = 0.4995, and decreases with ν thereafter. At the S-TB interface, the maximum gap size increases with ν up to a maximum of 180 μm for ν = 0.4990, and decreases with ν thereafter. For ν = 0.4995, the maximum gap size at both interfaces is essentially the same (about 140 μm). For smaller values of ν, the largest gap occurs at the S-TB interface; for larger values of ν, the largest gap occurs at the S-IB interface.

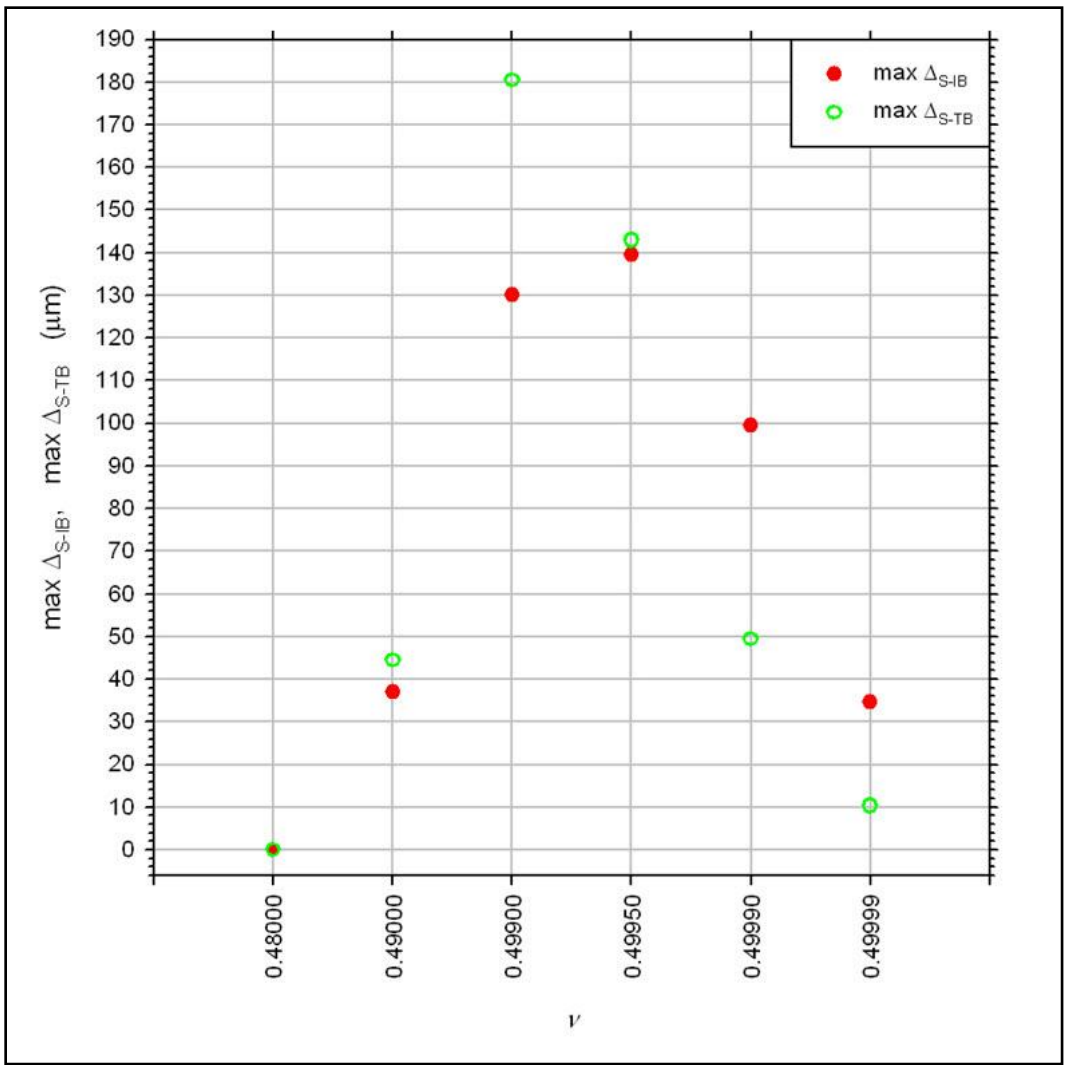

Figure 34. The maximum gap size at the centerline for each interface as a function of Poisson's ratio (linear elastic model, 1-μs rise time).

The gap of 180 μm on the centerline at the S-TB interface for the case $\nu = 0.4990$ is the largest gap size observed in all of the simulations in this report. This occurred at 276 μs, which is about 110 μs after the loading wave arrived at the specimen. Figure 35 plots the deformed mesh in the vicinity of the specimen at this instant for this value of Poisson's ratio. The centerline lies along the bottom of the plot, so the figure shows the entire deformed specimen mesh in the 2-D axisymmetric simulation. It is clear that at this instant the gaps at either interface are largest on the centerline. Also, the gap extends further outward radially at the S-TB interface. Along most of the radial extent of the gap at the S-TB interface and along half of the radial extent of the gap at the S-IB interface, the gap size exceeds the 100-μm length of bar elements and hence is several times larger than the 50-μm initial length of the undeformed specimen elements, which in turn is much larger than the deformed element length at this instant. This observation supports the assessment that the gap phenomenon cannot be attributed to numerical artifact associated

with an insufficiently fine mesh. Finally, note that according to figure 31, the estimated axial stretch at this instant is about 0.69; the corresponding nominal strain is 31%. However, these estimates are based on equations 8 and 9, that is, on the distance between the two bars. It is clear from figure 35 that for radial locations near the centerline, the axial strain in the specimen is substantially higher than this estimated value.

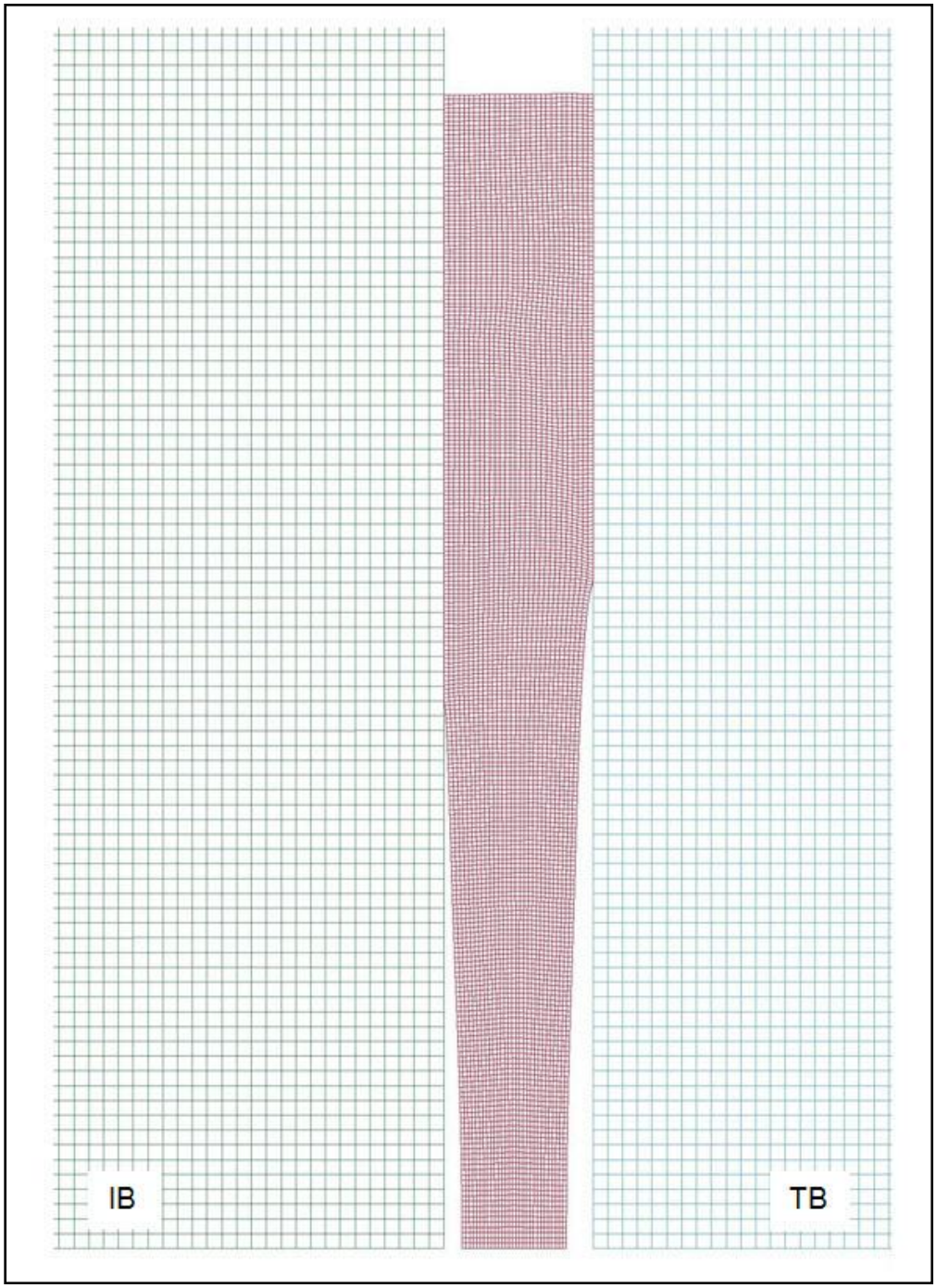

Figure 35. Deformed mesh in the vicinity of the specimen at $t = 276$ μs for Poisson's ratio $\nu = 0.4990$ (linear elastic model, 1-μs rise time).

8.2 The 25-μs Initial Rise Time

Figures 36–40 present results for the loading wave with a 25-μs initial rise time. Figure 36 compares the histories of the gap size on the centerline at the two interfaces for the case $\nu = 0.49999$. Also plotted in that figure (right axis) is the history of the axial stretch λ_z. The gap forms at about 185 μs (5% nominal strain). The pulse shaping has delayed the onset of gap formation, has substantially reduced the gap size at both interfaces (the largest value is now about 2.6 μm), and has also substantially reduced the duration over which the gap first remains open at the S-IB interface. These features are similar to those observed for the nonlinear model (see section 7).

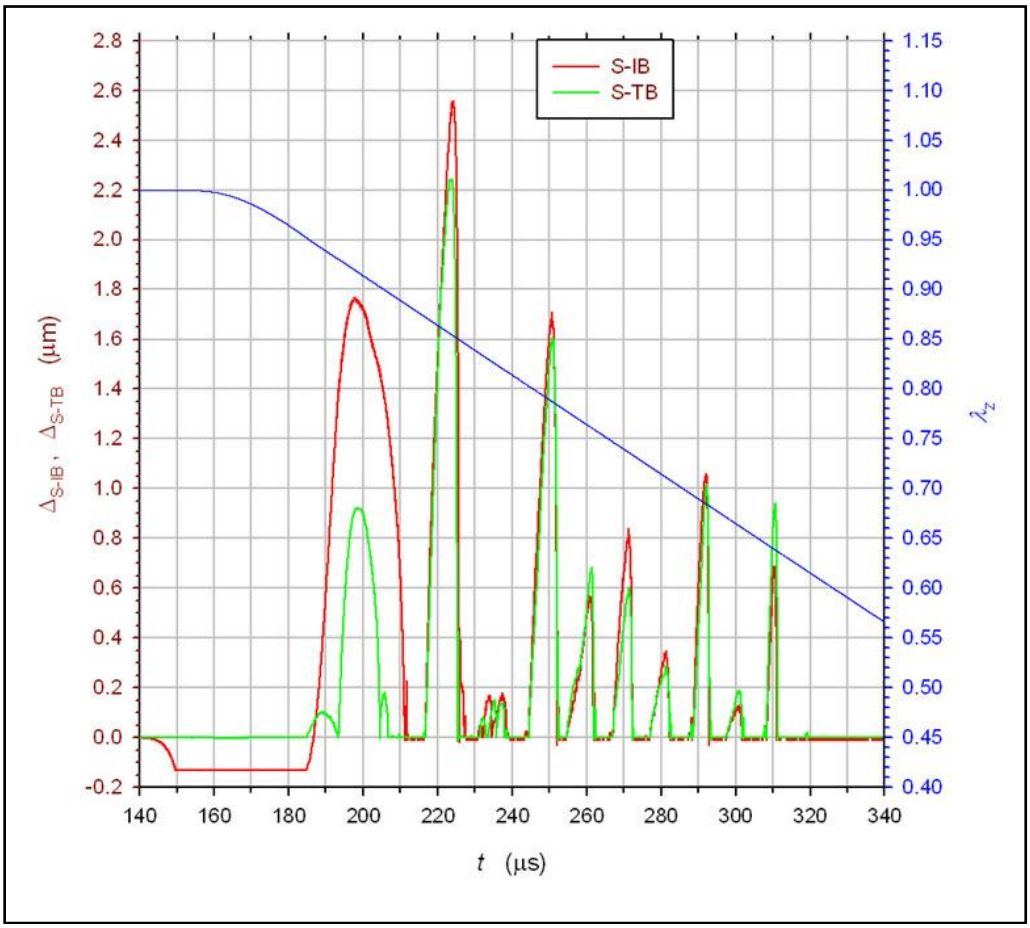

Figure 36. A comparison of the histories of the gap sizes on the centerline at the S-IB and S-TB interfaces for a 25-μs rise time and $\nu = 0.49999$ (linear elastic model). Also shown is the history of mean axial stretch in the specimen (blue).

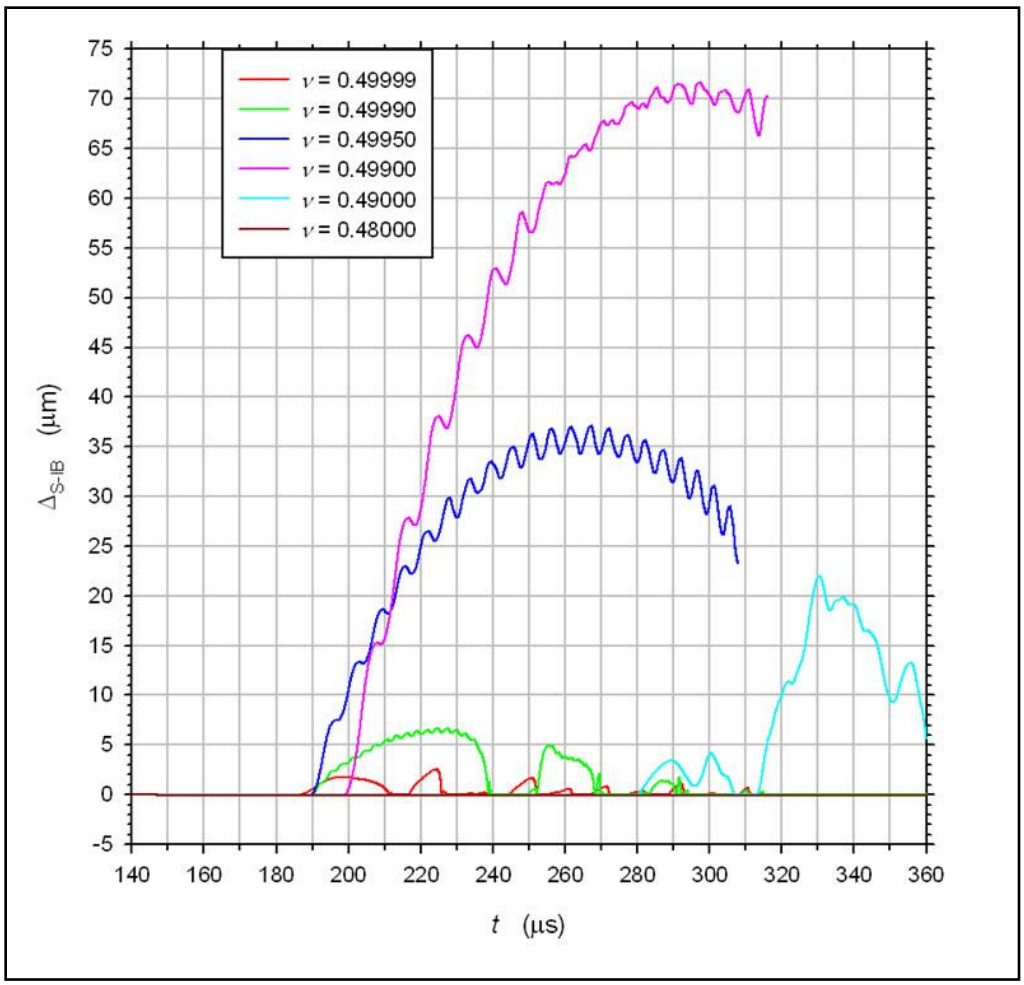

Figure 37. A comparison of the histories of the gap sizes on the centerline at the S-IB interface for a 25-μs rise time and selected values of Poisson's ratio (linear elastic model).

Figures 37 compares the histories of the gap size on the centerline at the S-IB interface for the six values of Poisson's ratio. Figure 38 does the same at the S-TB interface. Just as for the 1-μs initial rise time, gaps form at both interfaces for $\nu \geq 0.49$, but they do not form at either interface for the lowest value of Poisson's ration, $\nu = 0.48$. For simulations that exhibited hourglassing, the gap history curves were terminated well before hourglassing occurred.

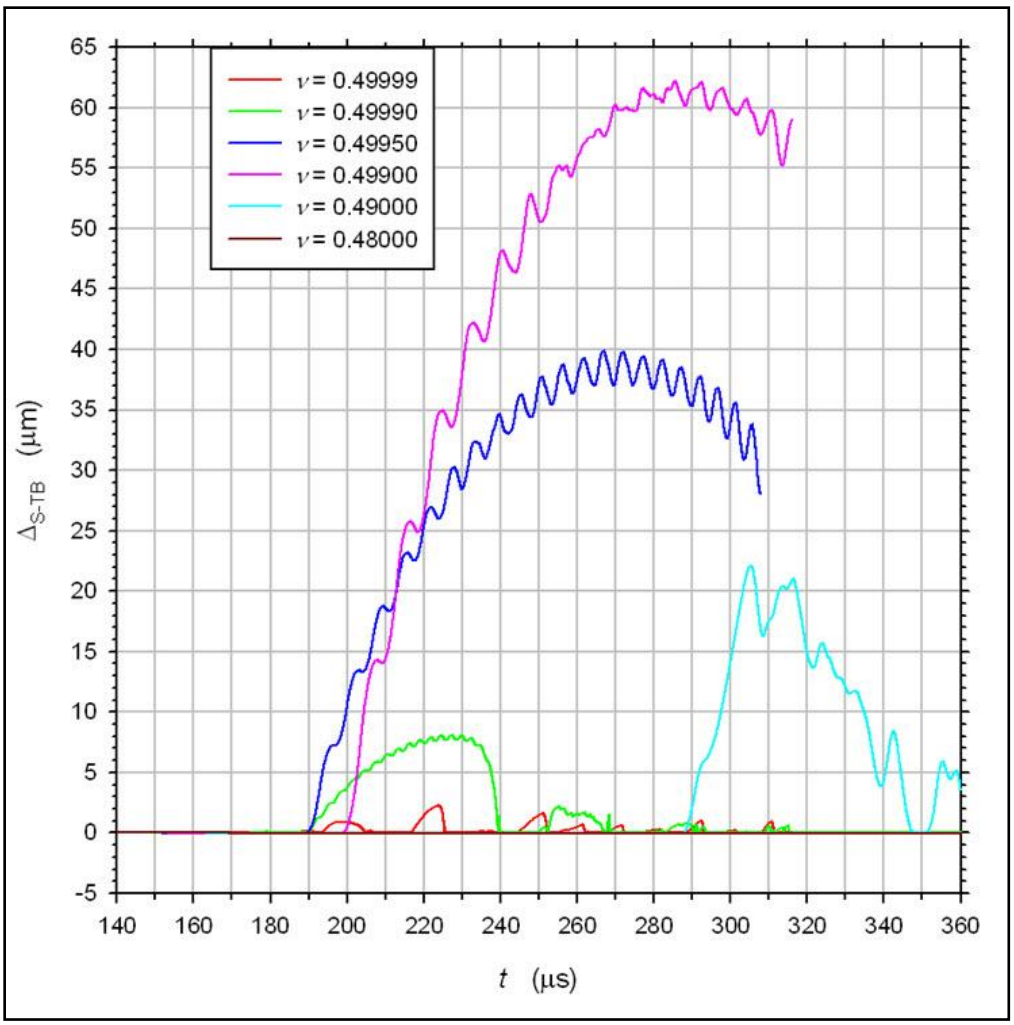

Figure 38. A comparison of the histories of the gap sizes on the centerline at the S-TB interface for a 25-μs rise time and selected values of Poisson's ratio (linear elastic model).

Just as for the 1-μs initial rise time, the maximum value (over the duration of the simulation) of the size of the gap at the centerline does not vary monotonically with Poisson's ratio. Figure 39 plots this maximum gap size at each interface as a function of Poisson's ratio ν. At both interfaces the maximum gap size increases with ν up to ν = 0.499, and decreases with ν thereafter. The maximum gap sizes for each value of Poisson's ratio are roughly the same at both interfaces, with the largest differences occurring for ν = 0.499.

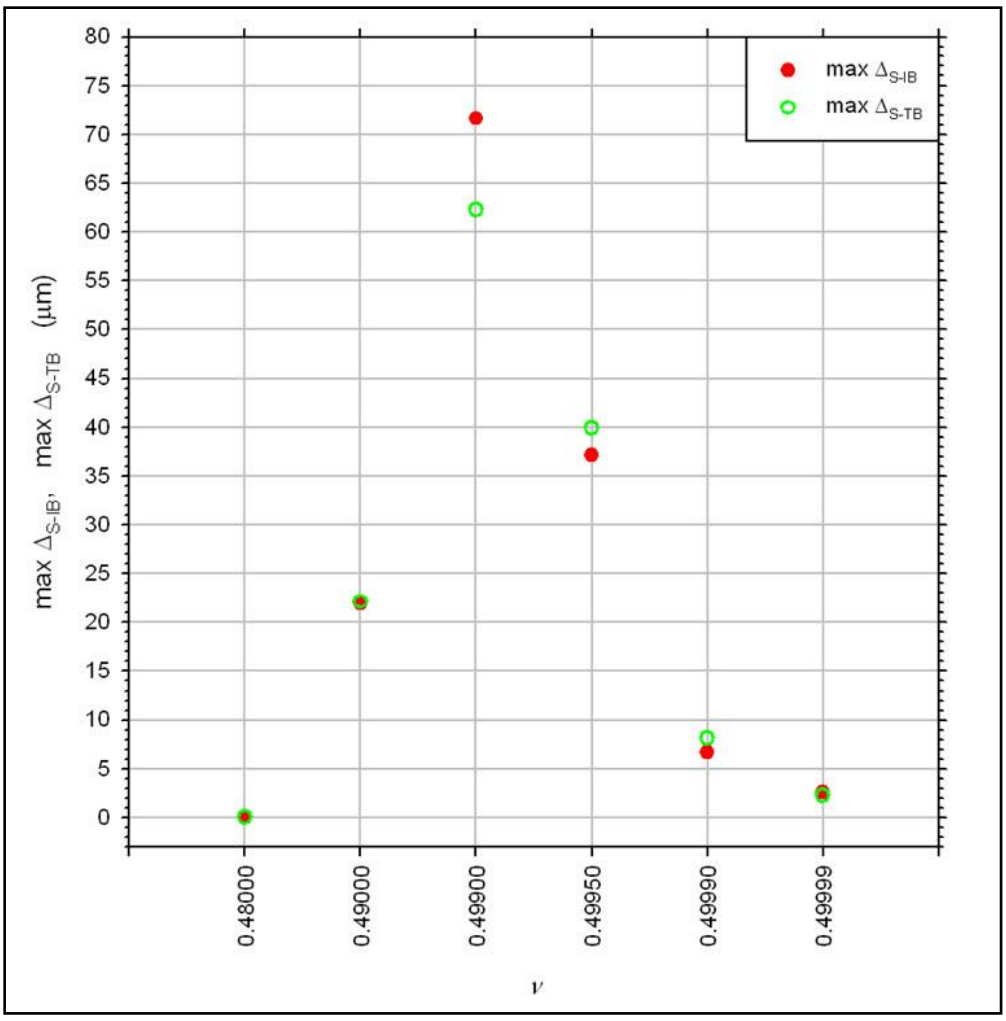

Figure 39. The maximum gap size at the centerline for each interface as a function of Poisson's ratio (linear elastic model, 25-μs rise time).

Figure 40 plots the deformed mesh in the vicinity of the specimen at 286 μs for the case $\nu = 0.499$. For this value of ν and this instant, the gap size at the S-TB interface achieves its largest value of 62 μm, and the gap at the S-IB interface is 71 μm, which is nearly equal to its largest value of 72 μm (see figures 38 and 39). From figure 36, we see that the estimated axial stretch at this time is about 0.70, which implies a nominal strain of 30%. The centerline lies along the bottom of the plot, so the figure shows the entire (deformed) specimen mesh in the 2-D axisymmetric simulation. Both gaps extend to about half the radius of the specimen. Along most of the radial extent of the gap at either interface, the size of the gap exceeds the initial length of the specimen elements and is about twice the deformed length of the elements.

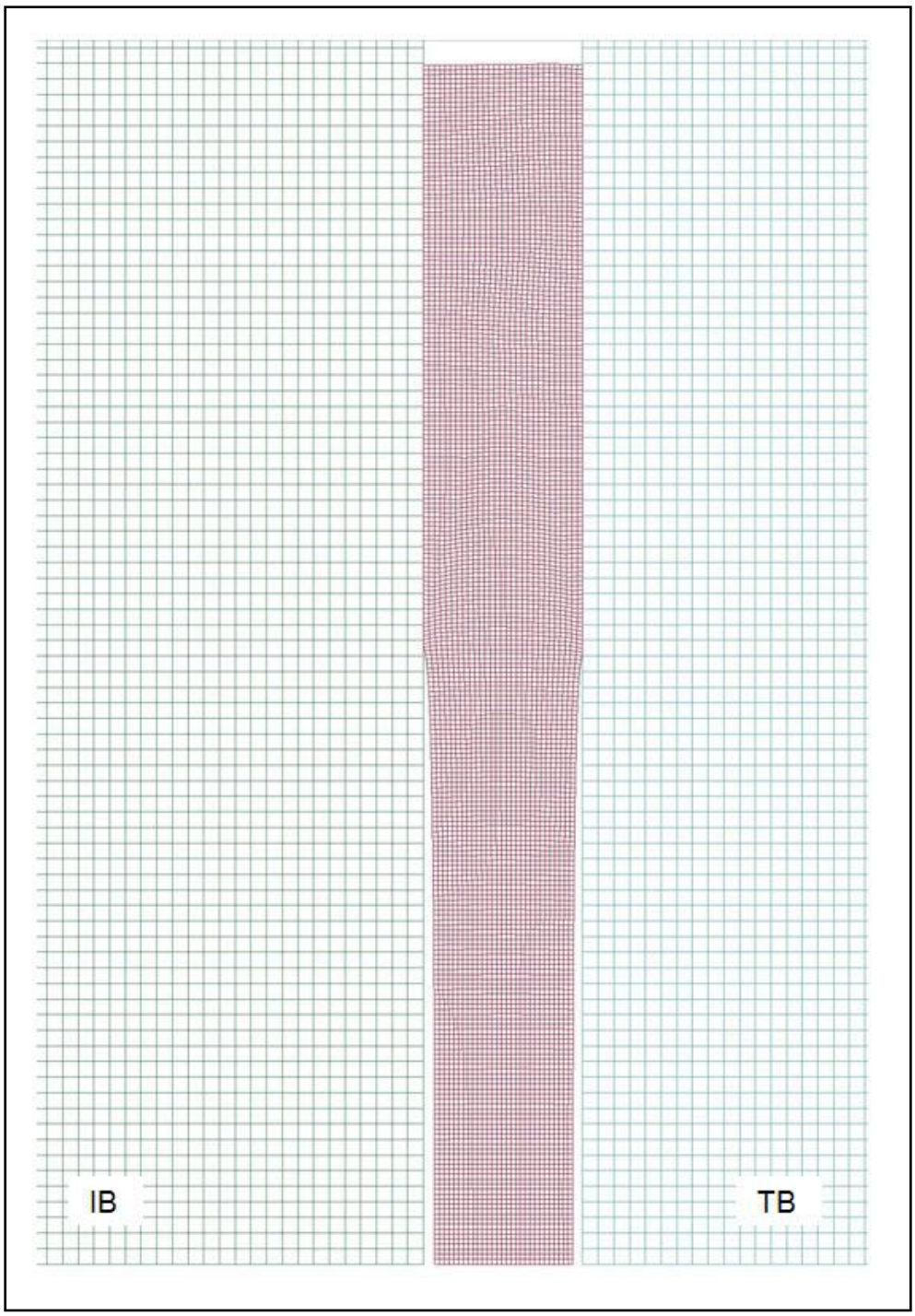

Figure 40. Deformed mesh in the vicinity of the specimen at t = 286 μs for Poisson's ratio ν = 0.4990 (linear elastic model, 25-μs rise time).

9. Discussion and Concluding Remarks

The SHPB test is designed to impose a state of *compressive* uniaxial stress on the specimen, at least after an initial ringing-up period. Even during the ring-up, one expects that the specimen is in a (generally non-uniform) state of compression, since the initial compressive longitudinal wave in the specimen reflects from the higher impedance pressure bars as a compressive wave. Thus the implicit assumption that the specimen and pressure bars remain in contact would appear to be reasonable.

Nevertheless, in this report we have presented conclusive numerical evidence that gaps may open between the specimen and the bars under certain conditions. These gaps formed at small strains but existed out to large strains, closing and re-opening multiple times. In some cases the gaps persisted for over 100 μs and extended over much of a face of the specimen for most of that time. The results in the appendix support the conclusion that this gap phenomenon is not an artifact of an insufficiently fine mesh (appendix B-1) or of the contact algorithm (appendix B-2) or of the particular code used for the simulations (appendix C-3). If a gap does exist over a substantial portion of the specimen face in a SHPB test, then that test is invalid for the purposes of material property characterization since the estimates for the axial stress, strain, and strain rate are no longer representative of the non-uniform conditions in the specimen.

The results of this study indicate that for soft specimens, gaps are most likely to form under a combination of two conditions, one pertaining to the specimen properties and the other to the loading conditions. For a given loading condition, gaps seem more likely to form in specimens which are nearly incompressible. This condition was satisfied in the two simulations with the nonlinear elastic (Mooney-Rivlin) model for the specimen, and gaps formed in both cases (sections 6 and 7). When a linear elastic model was used for the specimen, gaps formed for five of the six sets of elastic moduli considered (section 8). The case where no gaps formed corresponded to the lowest Poisson's ratio (0.48) and hence to the highest ratio of shear to bulk modulus (0.04).

The loading condition that seems to promote gap formation is axial deceleration of the specimen. As the time rate of change of the velocity imposed by the incident bar on the specimen decreases from peak positive values (acceleration) through zero to negatives values (deceleration), the axial stress at the specimen-bar interfaces drops to zero, allowing the specimen to separate from the bars. It appears that the driving mechanism behind this inertial effect is the corresponding radial deceleration induced by the axial deceleration. This conclusion is not inconsistent with existing literature on radial inertial effects for soft specimens (*26–33*). Furthermore, we found that constraining the lateral surface of the specimen (to eliminate the radial motion) suppresses gap formation, at least in direct impact tests (appendix C-1.1).

On the other hand, the simple qualitative conclusions above belie the extremely complex stress states in the specimen and pressure bars (particularly the incident bar) at times in the vicinity of gap formation, as illustrated by the pressure contour plots in section 6.3.[44] Starting about 1.6 μs prior to the opening of gaps at both interfaces and at least 1 μs prior to the onset of negative pressure in the specimen, the pressure in the incident bar oscillates (with axial distance from the specimen) between positive and negative values, eventually becoming negative in the entire vicinity of the specimen immediately before the gaps form (section 6.3).

To the best of our knowledge, the gap phenomenon documented here has not been reported in either the experimental or the computational literature. However, certain features of previously reported experimental data appear to be consistent with the opening and closing of gaps, namely, axial stress histories (inferred from strain or stress gage measurements in the bars) which oscillate between positive and negative values (see section 7.3). Since our initial concern was to determine whether or not these gaps were a numerical artifact, we focused on examining a few cases in detail rather than simulating a broad range of loading conditions and constitutive models for the specimen. Consequently, our study is by no means exhaustive. We conclude by listing some of the limitations of this work, which in turn suggest areas for further study:

1) We certainly expect that gaps will no longer form if the strain rate in the specimen is sufficiently small, but only one axial strain rate was considered here, a nominal rate of 2500/s (after the initial ring-up). The imposed strain rate can be reduced either by decreasing the plateau velocity imposed at the far end of the incident bar or by increasing the thickness of the specimen.

2) We considered only a linear ramp to a plateau velocity in the main body of the report (and more severe loadings in the appendices C-1 and C-3). It would be of interest to consider smoother loading histories at the far end of the incident bar, since experimental evidence indicates that gaps do not form with better pulse shaping.

3) We considered only one specimen diameter (12.7 mm). Theories on radial inertial effects in SHPB tests predict that the inertial stresses are proportional to the square of the specimen diameter. Thus if radial inertia is a mechanism for gap formation, we would expect that gaps would no longer form if the specimen diameter is sufficiently small.

4) All the simulations in this report involved specimens that were "soft" relative to the bars (particularly in shear), so we cannot draw any conclusions about gap formation in stiffer specimens.

[44] Recall that these pressure contours were for the loading wave with a 1-μs initial rise time.

5) Only elastic (linear or nonlinear) constitutive models were considered for the specimen, since absence of strain rate effects in the model allowed for easier interpretation of the results. It is not clear how the incorporation of viscoelasticity in the model would affect the formation of gaps, although we have no reason to believe that this would suppress gap formation altogether.

6) For the nonlinear elastic specimen model (the compressible Mooney-Rivlin model), we considered only one set of material parameters. It would be instructive to fix the bulk modulus and increase the shear modulus until gap formation is suppressed. Note that in the simulations with a linear elastic specimen, we essentially fixed the shear modulus and decreased the bulk modulus until gap formation was suppressed.

7) As an approximation to a well lubricated specimen, the specimen-bar interfaces were treated as frictionless in the simulations. It is not clear what effect (if any) a small amount of friction would have on the formation of gaps.

10. References

1. Gray III, G. T. Classic Split-Hopkinson Pressure Bar Testing, *ASM Handbook Vol. 8, Mechanical Testing and Evaluation*; American Society for Metals: Materials Park, Ohio, 462–476, 2000.
2. Gama, B. G.; Lopatnikov, S. L.; Gillespie Jr., J. W. Hopkinson bar experimental technique: a critical review. *Applied Mechanics Reviews* **2004**, *57*, 223–250.
3. Gray III, G. T.; Blumenthal, W. R. Split-Hopkinson Pressure Bar Testing of Soft Materials, *ASM Handbook Vol. 8, Mechanical Testing and Evaluation*; American Society for Metals: Materials Park, Ohio, 488–496, 2000.
4. Song, B.; Chen, W. Split Hopkinson pressure bar techniques for characterizing soft materials. *Latin American Journal of Solids and Structures* **2005**, *2*, 113–152.
5. Moy, P.; Weerasooriya, T.; Juliano, T. F.; VanLandingham, M. R.; Chen, W. *Dynamic Response of an Alternative Tissue Simulant, Physically Associating Gels (PAG)*; ARL-RP-136; U.S. Army Research Laboratory: Aberdeen Proving Ground, MD, September 2006.
6. Song, B.; Ge, Y.; Chen, W. W.; Weerasooriya, T. Radial Inertia Effects in Kolsky Bar Testing of Extra-soft Specimens. *Experimental Mechanics* **2007**, 47, 659–670.
7. Scheidler, M. Inertial Effects in the Characterization of Incompressible Soft Materials in Hopkinson Bar Tests. presented at the *44th Annual Meeting of the Society of Engineering Science*, Texas A&M University, October 21–24, 2007.
8. Livermore Software Technology Corporation, *LS-DYNA Keyword User's Manual*, Volume II, Version 971, May 2007.
9. Hallquist, J. O. *LS-DYNA Theory Manual*, March 2006.
10. Aihaiti, M.; Hemley, R. J. *Equation of state of ballistic gelatin*; Report No. 50533-EG.1; U.S. Army Research Office, June 2008.
11. Raftenberg, M. N.; Scheidler, M. Gap Formation in Simulations of SHPB Tests on Elastic Materials Soft in Shear, Shock Compression of Condensed Matter–2009. *AIP Conference Proceedings*, American Institute of Physics; Melville, New York, 2009; Vol. 1195: pp 715–718.
12. Eringen, A. C.; Suhubi, E. S. *Elastodynamics vol. II: Linear Theory*; Academic Press: New York, 1975.

13. Mooney, M. A Theory of Large Elastic Deformation. *Journal of Applied Physics* **1940**, *11*, 582–592.

14. Rivlin, R. S. Torsion of a Rubber Cylinder. *Journal of Applied Physics* **1947**, *18*, 444–449.

15. Treloar, L.R.G. *The Physics of Rubber Elasticity, 3rd Ed.*; Clarendon Press: Oxford, 1975.

16. Batra, R. C. *Elements of Continuum Mechanics*, AIAA, Reston, VA, 2005.

17. Ogden, R. *Non-Linear Elastic Deformations*; Dover Publications: Mineola, NY, 1997.

18. Truesdell, C.; Noll, W. *The Non-Linear Field Theories of Mechanics, 2nd Ed.*; Springer: New York, 1992.

19. Holzapfel, G. A. *Nonlinear Solid Mechanics*; John Wiley & Sons: New York, 2000.

20. Winter, J.; Shifler, D. *The Material Properties of Gelatin Gels*, BRL Contractor Report No. 217, March, 1975.

21. Rapacki, E. Private communication, ARL, 2009.

22. Juliano, T. F.; Forster, A. M.; Drzal, P. L.; Weerasooriya, T.; Moy, P.; VanLandingham, M. R. Multiscale Mechanical Characterization of Biomimetic Physically Associating Gels. *J. Mater. Res.* **2006**, *21*, 2084–2092.

23. Steinberg, D. J. *Equation of State and Strength Properties of Selected Materials*; UCRL-MA-106439; Lawrence Livermore National Laboratory Report, Feburary 1996.

24. Graff, K. F. *Wave Motion in Elastic Solids*; Dover Publications: New York, 1991.

25. Casem, D.; Weerasooriya, T.; Moy, P. Inertial Effects of Quartz Force Transducers Embedded in a Split Hopkinson Pressure Bar. *Experimental Mechanics* **2005**, *45*, 368–376.

26. Forrestal, M. J.; Wright, T. W.; Chen, W. The Effect of Radial Inertia on Brittle Samples During the Split Hopkinson Pressure Bar Test. *International Journal of Impact Engineering* **2007**, *34*, 405–411.

27. Dharan, C.K.H.; Hauser, F. E. Determination of Stress-Strain Characteristics at Very High Strain Rates. *Experimental Mechanics* **1970**, *10*, 370–376.

28. Gorham, D.A.P.; Pope, P. H.; Cox, O. Sources of Error in Very High Strain Rate Compression Tests. *Institute of Physics Conference Series No. 70*, **1984**, 151–158.

29. Walley, S. M.; Field, J. E.; Pope, P. H; Safford, N. A. The Rapid Deformation Behaviour of Various Polymers. *J. Phys. III France* 1, **1991**, 1889-1925.

30. Maliowski, J. Z.; Klepaczko, J. R.; Kowalewski, Z. L. Miniaturized Compression Test at Very High Strain Rates by Direct Impact. *Experimental Mechanics* **2007**, *47*, 451–463.

31. Jia, D.; Ramesh, K. T. A Rigorous Assessment of the Benefits of Miniaturization in the Kolsky Bar System. *Experimental Mechanics* **2004**, *44*, 445–454.

32. Scheidler, M.; Kraft, R. Inertial Effects in Compression Hopkinson Bar Tests on Soft Materials. to appear in the *Proceedings of the 1st Annual ARL Ballistic Technologies Workshop*, 2010.

33. Warren, T. L.; Forrestal, M. J. Comments on the Effect of Radial Inertia in the Kolsky Bar Test for an Incompressible Material, *Experimental Mechanics,* published online 29 December 2009, DOI 10.1007/s11340-009-9322-x.

34. Chung, D.-T. The Effect of Specimen Shape on Dynamic Flow Stress, Shock Compression of Condensed Matter–1995, *AIP Conference Proceedings*, American Institute of Physics: Woodbury, New York, 1996; Vol. 370: pp 483–486.

35. Chen, W.; Lu, F.; Frew, D.; Forrestal, M. Dynamic Compression Testing of Soft Materials. *Journal of Applied Mechanics* **2002**, 69, 214–223.

36. Scheidler, M.; Raftenberg, M.; Love, B.; Kraft, R. Inertial Effects in Numerical Simulations of Hopkinson Bar Tests on Nearly Incompressible Soft Materials, presented at *The Joint ASCE-ASME-SES Conference on Mechanics and Materials*, Virginia Tech, June 24–28, 2009.

37. Love, B. Unpublished results, ARL, 2008.

INTENTIONALLY LEFT BLANK.

Appendix A. The Mooney-Rivlin Constitutive Model

A-1 Theoretical Background

This subsection contains a brief discussion of the concepts and notation needed to describe the two nonlinear elastic models considered below; for additional background the reader may refer to the books (*16–19*).

Let λ_1, λ_2, λ_3 denote the principal stretches, that is, the ratios of the deformed to undeformed length along the principal axes of strain. Each stretch λ_i is unity in the undeformed state, with $\lambda_i > 1$ in tension, and $0 < \lambda_i < 1$ in compression. The principal nominal (engineering) strains are $\lambda_i - 1$ when taken positive in tension, or $1 - \lambda_i$ when taken positive in compression. The left Cauchy-Green deformation tensor $\boldsymbol{B}$ is defined in terms of the deformation gradient $\boldsymbol{F}$ by $\boldsymbol{B} = \boldsymbol{F}\boldsymbol{F}^T$, where the superscript T denotes the transpose. The principal axes of $\boldsymbol{B}$ are the principal axes of strain in the deformed state. The principal values (or eigenvalues) of $\boldsymbol{B}$ are λ_1^2, λ_2^2, λ_3^2, the squares of the principal stretches. The three principal invariants of $\boldsymbol{B}$ are

$$I_1 = \operatorname{tr} \boldsymbol{B} = \lambda_1^2 + \lambda_2^2 + \lambda_3^2 , \tag{A-1}$$

$$I_2 = \frac{1}{2}[(\operatorname{tr} \boldsymbol{B})^2 - \operatorname{tr} \boldsymbol{B}^2] = \lambda_1^2\lambda_2^2 + \lambda_2^2\lambda_3^2 + \lambda_3^2\lambda_1^2 , \tag{A-2}$$

$$I_3 = \det \boldsymbol{B} = \lambda_1^2\lambda_2^2\lambda_3^2 = J^2 . \tag{A-3}$$

Here "tr" denotes the trace, "det" denotes the determinant, and

$$J = \det \boldsymbol{F} = \lambda_1\lambda_2\lambda_3 \tag{A-4}$$

is the Jacobian of the deformation, that is, the local ratio of deformed to undeformed volume. Thus, $J = 1$ at points where there is no volume change. A useful alternative expression for I_2 is

$$I_2 = I_3 \operatorname{tr} \boldsymbol{B}^{-1} = I_3\left(\frac{1}{\lambda_1^2} + \frac{1}{\lambda_2^2} + \frac{1}{\lambda_3^2}\right) . \tag{A-5}$$

The principal stresses (i.e., the eigenvalues) of the Cauchy stress tensor $\boldsymbol{\sigma}$ are denoted by σ_1, σ_2, σ_3, and the pressure p is given by

$$p = -\frac{1}{3}\operatorname{tr} \boldsymbol{\sigma} = -\frac{1}{3}(\sigma_1 + \sigma_2 + \sigma_3) . \tag{A-6}$$

For any (not necessarily linear) isotropic elastic material, the principal axes of stress coincide with the principal axes of $\boldsymbol{B}$.

A-2 The Mooney-Rivlin Model for Incompressible Elastic Materials

The classical Mooney-Rivlin model is a nonlinear elastic constitutive model for isotropic, incompressible solids; cf. the original papers by Mooney (*13*) and Rivlin (*14*), as well as the books (*15–19*). Since the material is assumed to be incompressible, there is no change in volume, so equations A-3 and A-4 reduce to

$$I_3 = J = \lambda_1\lambda_2\lambda_3 = 1. \tag{A-7}$$

The strain energy function W for the Mooney-Rivlin model has the simple form

$$W = A_1\left(I_1 - 3\right) + A_2\left(I_2 - 3\right), \tag{A-8}$$

The coefficients $A_1 > 0$ and $A_2 \geq 0$ are constants with the units of stress (i.e., elastic moduli); the inequalities are required for physically realistic behavior. The Cauchy stress tensor corresponding to this strain energy function is

$$\boldsymbol{\sigma} = -\bar{p}\,\boldsymbol{I} + 2A_1\boldsymbol{B} - 2A_2\boldsymbol{B}^{-1}, \tag{A-9}$$

where $\boldsymbol{I}$ denotes the identity tensor. The shear modulus G in the small strain, linear elastic approximation to the constitutive relation A-9 is given by $G = 2(A_1 + A_2)$. The special case of equation A-9 with $A_2 = 0$ (and hence $2A_1 = G$) is called a neo-Hookean material.

The coefficient $\bar{p}$ in equation A-9 denotes an indeterminate scalar related to the pressure. The indeterminacy of $\bar{p}$ is a consequence of the incompressibility constraint: $\bar{p}$ is not determined by $\boldsymbol{B}$, but the value of $\bar{p}$ at each place and time must be such that the momentum balance equations and the boundary conditions are satisfied. Although $\bar{p}$ in equation A-9 is often referred to as a "pressure", it is generally not equal to the pressure p as defined in equation A-6, since the other terms in equation A-9 contribute to the trace of $\boldsymbol{\sigma}$.

The relation A-9 implies that the principal stresses are given by

$$\sigma_i = -\bar{p} + 2A_1\lambda_i^2 - 2A_2\frac{1}{\lambda_i^2} \qquad (i = 1,2,3). \tag{A-10}$$

The difference of any two principal stresses is independent of $\bar{p}$:

$$\sigma_i - \sigma_j = 2A_1\left(\lambda_i^2 - \lambda_j^2\right) - 2A_2\left(\frac{1}{\lambda_i^2} - \frac{1}{\lambda_j^2}\right). \tag{A-11}$$

Uniaxial Stress: The general relation A-11 may be used to obtain the stress-stretch relation in a uniaxial stress test. Consider a cylindrical coordinate system with the direction of applied stress parallel to the z-axis. Then σ_{zz} is the only non-zero stress component. If $\sigma_{zz} > 0$, this is a simple tension test; if $\sigma_{zz} < 0$, it is a simple compression test. Since the material is isotropic, the principal axes of strain lie along the coordinate axes in this case and the strains (and hence stretches) in the radial and hoop directions are equal. Thus, in the relations above, we may set

$\lambda_1 = \lambda_r = \lambda_\theta = \lambda_2$ and $\lambda_3 = \lambda_z$, as well as $\sigma_1 = \sigma_{rr} = \sigma_{\theta\theta} = \sigma_2 = 0$ and $\sigma_3 = \sigma_{zz}$. Then by equations A-6 and A-7, we see that $p = -\sigma_{zz}/3$ and

$$\lambda_r = \lambda_\theta = \frac{1}{\sqrt{\lambda_z}}. \tag{A-12}$$

Then on setting $i = 3$ and $j = 1$ in equation A-11 and using the relations above, we obtain the following expression for the axial stress σ_{zz} in terms of the axial stretch λ_z:

$$\sigma_{zz} = 2A_1\left(\lambda_z^2 - \frac{1}{\lambda_z}\right) - 2A_2\left(\frac{1}{\lambda_z^2} - \lambda_z\right) \approx 3G(\lambda_z - 1). \tag{A-13}$$

The expression on the right is the linearly elastic approximation, which is valid for small strains only, that is, λ_z close to 1. For an incompressible material, $3G = E$, where E is the Young's modulus, so we recover the well-known result that in the linear elastic approximation, the axial stress is the Young's modulus times the axial strain.

Stress Difference on the Centerline: Consider an axisymmetric (but possibly non-uniform) deformation of a solid cylindrical specimen. As discussed at the end of section 2.6, at points on the centerline (i.e., the z-axis), the radial, hoop and axial directions are principal axes of stress and strain, and the relations 14 in section 2.6 hold exactly. Thus, the principal stress difference $\sigma_{zz} - \sigma_{rr}$ is given by equation A-11 with the indices i and j set to z and r, respectively; and since $J = 1$, equation A-12 holds. Therefore,

$$\sigma_{zz} - \sigma_{rr} = 2A_1\left(\lambda_z^2 - \frac{1}{\lambda_z}\right) - 2A_2\left(\frac{1}{\lambda_z^2} - \lambda_z\right) \approx 3G(\lambda_z - 1)\ , \tag{A-14}$$

where the linearly elastic approximation on the right holds for small strains.

Note that the right-hand side of this equation is the same as that of equation A-13. In particular, for a uniaxial stress test, equation A-14 reduces to equation A-13 since $\sigma_{rr} = 0$ in that case. However, for the more general case considered here, σ_{rr} need not be zero, and equation A-14 is only valid on the centerline.

A-3 The Compressible Version of the Mooney-Rivlin Model in LS-DYNA

The simulations described in sections 6 and 7 used LS-DYNA's compressible version of the Mooney-Rivlin model for the specimen; this is Material Type 27 in (*8*, *9*). The model has three material constants (aside from the density): the elastic moduli[45] A_1 and A_2 and the Poisson's ratio ν. The strain energy (per unit undeformed volume) is given by

$$W = A_1(I_1 - 3) + A_2(I_2 - 3) + C\left(I_3^{-2} - 1\right) + D(I_3 - 1)^2, \tag{A-15}$$

[45] The LS-DYNA manuals (*8*, *9*) use the symbols A and B for the constants A_1 and A_2, respectively.

which differs from the incompressible model by the addition of the terms with coefficients C and D. The constant C is determined from A_1 and A_2 by

$$C = \frac{A_1}{2} + A_2 \,. \tag{A-16}$$

The constant D is determined from A_1, A_2, and ν by

$$D = \frac{A_1(5\nu - 2) + A_2(11\nu - 5)}{2(1 - 2\nu)} \,. \tag{A-17}$$

We refer to this as the "compressible Mooney-Rivlin model".

The Cauchy stress tensor corresponding to this strain energy function is[46]

$$\boldsymbol{\sigma} = -\bar{p}\,\boldsymbol{I} + 2\frac{A_1}{J}\boldsymbol{B} - 2A_2 J\boldsymbol{B}^{-1}, \tag{A-18}$$

where

$$\bar{p} = 4D\left(J - J^3\right) + \frac{4C}{J^5} - \frac{2A_2}{J} I_2 \,. \tag{A-19}$$

When $J = 1$, equation 18 yields the relations A.10 and A.11 for the principal stresses, which were obtained previously for the incompressible model. If J is close to 1, then these relations hold as approximations. Similarly, when $J = 1$, we recover the relation A-13 for the axial stress σ_{zz} in a uniaxial stress test and the relation A-14 for the stress difference $\sigma_{zz} - \sigma_{rr}$ on the centerline for a general axisymmetric deformation. If J is close to 1, then[47] $\lambda_r \approx 1/\sqrt{\lambda_z}$, and we find that A-13 and A-14 hold as approximations. In this regard, note that $3G \approx E$ for a nearly incompressible material; indeed, for the ballistic gelatin specimen they agree to at least three significant figures (see table 1).

Note that the scalar $\bar{p}$ in equations A-18–A-19 is generally not equal to the pressure p, since the other terms in equation A-18 contribute to the trace of $\boldsymbol{\sigma}$. Indeed, from equations A-6, A-18, A-5, and A-19, we obtain

$$p = \bar{p} - \frac{2}{3}\frac{A_1}{J} I_1 + \frac{2}{3}\frac{A_2}{J} I_2 \,. \tag{A-20}$$

---

[46] None of the relations in this paragraph appear in the LS-DYNA User's Manual (*8*) or in the Theory Manual by Hallquist (*9*). However, equation A-18 is equivalent to the relation for the second Piola-Kirchhoff stress tensor given in (*9*), and equations A-19–A-20 imply the relation for the pressure in a state of pure dilation given in (*9*).

[47] See equation 15 in section 2.6.

Thus the pressure p is a complicated function of both the volumetric strain and the shear strain. In particular, p does not necessarily reduce to zero when there is no volume change (i.e., when $J = 1$). However, p does equal zero in the undeformed state, as expected. This follows from equations A-20, A-19, A-16, and the fact that $J = 1$ and $I_1 = I_2 = 3$ when the material is undeformed.

For nearly incompressible materials (ν close to ½), A_1 and A_2 (and hence C) are small compared to D, so for small volume changes (J close to but not equal to 1), equations A-19 and A-20 yield the simple approximations

$$\bar{p} \approx p \approx K(1-J), \qquad K \approx 8D, \tag{A-21}$$

where the constant K is the initial (or linear elastic) bulk modulus. It is easily verified that the approximation for K in equation A-21 is consistent with equations 2_1, 16, and A-17 when ν is close to ½.

The LS-DYNA manuals do not provide any explanation or references for the unconventional form of the two compressibility terms in the strain energy function in equation A-15, that is, the terms with coefficients C and D, although the term involving C appears to have been added so that the pressure reduces to zero in the undeformed state. However, the relation for the pressure obtained from this strain energy function (equations A-19–A-20) is inappropriate for large volumetric strains, since the $J - J^3$ term in equation A-19 has an absolute maximum at

$$J = \frac{1}{\sqrt{3}} \approx 0.58 \ . \tag{A-22}$$

If ν is sufficiently close to ½ (e.g., $\nu \geq 0.4999$), the $J - J^3$ term dominates except at very large compressions (i.e., $J < 0.5$).[48] This physically unrealistic behavior was not an issue for the SHPB simulations reported here. For the parameters used in our calibration of the model (see table 3), the value of the pressure at the maximum described above is about 770 MPa, whereas the peak pressures in our simulations were around 4 MPa, with the exception of the sharp spikes on the centerline which did not exceed 10 MPa.[49] In other words, the volume changes were small enough that the approximation A-21 was valid.

A-4 Verification of the Compressible Mooney-Rivlin Model

Prior to our simulations of SHPB tests, we performed a partial verification of the implementation of the compressible version of the Mooney-Rivlin model in LS-DYNA. We used the fact that for a quasi-static uniaxial stress test, the stress predicted by the compressible model should approach that predicted by the incompressible model as Poisson's ratio ν approaches ½ with A_1 and A_2 fixed. The constants A_1 and A_2 were chosen as in table 3. We used a single 8-node

[48] This unrealistic behavior is caused by the last term in equation A.15; it could be eliminated by replacing I_3 there by its square root, that is, by J, but then the term with coefficient C would also need to be modified to guarantee that the pressure is zero in the undeformed state.

[49] Refer to figures 11, 12, 17–23, 27, and 28, and recall that in the axial stress history plots, the stress state at the stress peaks prior to the formation of gaps is nearly hydrostatic.

hexagon element that was initially cubic with a 100 μm edge length. In order to diminish any inertial effects, the initial density was reduced from 1 to 0.001 g/cm^3 for these simulations only. There were no discernable differences in the results for nominal axial strain rates of 100/s, 1000/s, and 10,000/s.

For various values of Poisson's ratio ν between 0.495 and 0.49999, the stress components were computed for axial stretches λ_z ranging from 0.2 (large compression) to 4.0 (large extension). These results were compared with the theoretical relation A-13 for the incompressible model. The results for ν = 0.495 are shown in figure A-1. The stress-stretch curves for the axial stress σ_{zz} for the compressible model (red) and incompressible model (dashed line) are indistinguishable except for a slight difference when λ_z is below 0.35. This difference decreased for higher values of Poisson's ratio; in particular, for the value ν = 0.49999 used in the SHPB simulations, the stress-stretch curves were indistinguishable for all values of λ_z. As expected, the other stress components[50] (the blue line in the figure) were indistinguishable from zero on this scale.

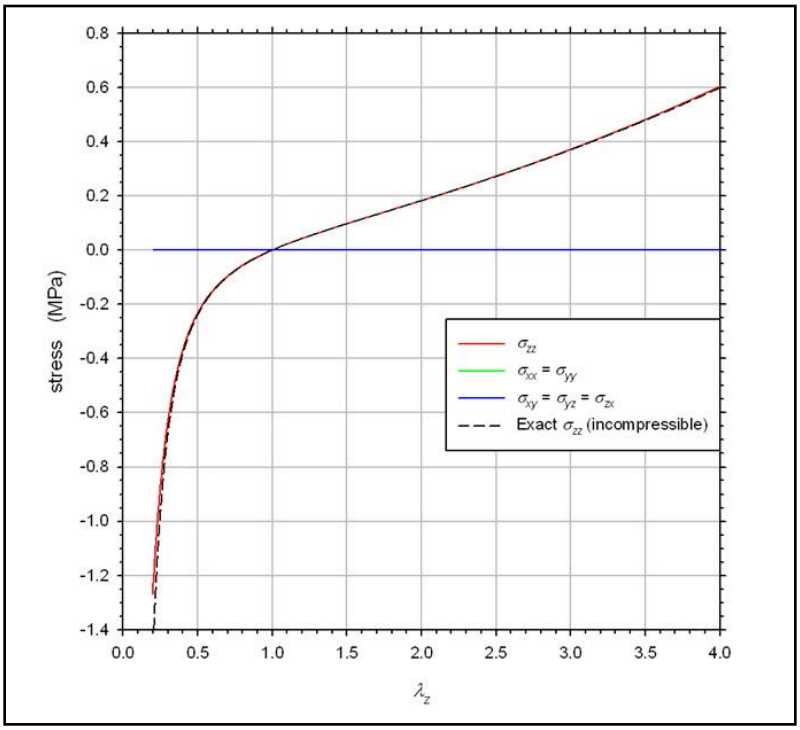

Figure A-1. Stress components as a function of axial stretch λ_z for a uniaxial stress test on a single element using the compressible Mooney-Rivlin model with ν = 0.495 (colored curves). Comparison with axial stress σ_{zz} for the incompressible model (dashed curve).

Finally, note that for small volume changes ($J \approx 1$), the curve in figure A-1 also represents the stress difference $\sigma_{zz} - \sigma_{rr}$ on the centerline for a general axisymmetric deformation.[51]

[50] These components are taken relative to a Cartesian coordinate system aligned with the (initially cubic) specimen.

[51] See equation A-14 and the discussion following equation A-19.

Appendix B. Sensitivity Studies

All of the results presented in the main body of this report were obtained with the baseline 25×50-μm mesh in the specimen; see section 4.1 and figure 2a. All of the results presented in the main body were obtained with the LS-DYNA default values of the contact algorithm parameters (SFAC = 1, VDC = 10); see section 4.2. Here we examine the sensitivity of the gap size on the centerline to the size of the specimen mesh (appendix B-1) and the contact algorithm parameters (appendix B-2).

For the mesh sensitivity study the default values of the contact algorithm parameters are used. Likewise, for the contact algorithm sensitivity study, the baseline mesh is used. For all of the results in this appendix we used the compressible Mooney-Rivlin constitutive model for the specimen and the larger (12.8-mm) bar radius. Both the 1- and 25-μs initial rise times for the loading wave are considered.

B-1 Mesh Sensitivity

Refer to section 4.1 for a discussion of the specimen and bar meshes. Figures B-1–B-4 compare the histories of the gap size on the centerline for three specimen meshes: the baseline 25×50 μm mesh (figure 2a), the coarser 50×100μm mesh (figure 2b), and the finer 12.3×12.5 μm mesh (figure 2c). The mesh size in the bars is 100×100 μm for all simulations. Figures B-1 and B-2 are for the 1-μs initial rise time for the loading wave; figures B-3 and B-4 are for the 25-μs initial rise time. Figures B-1 and B-3 give the gap size at the S-IB interface; figures B-2 and B-4 give the gap size at the S-TB interface.

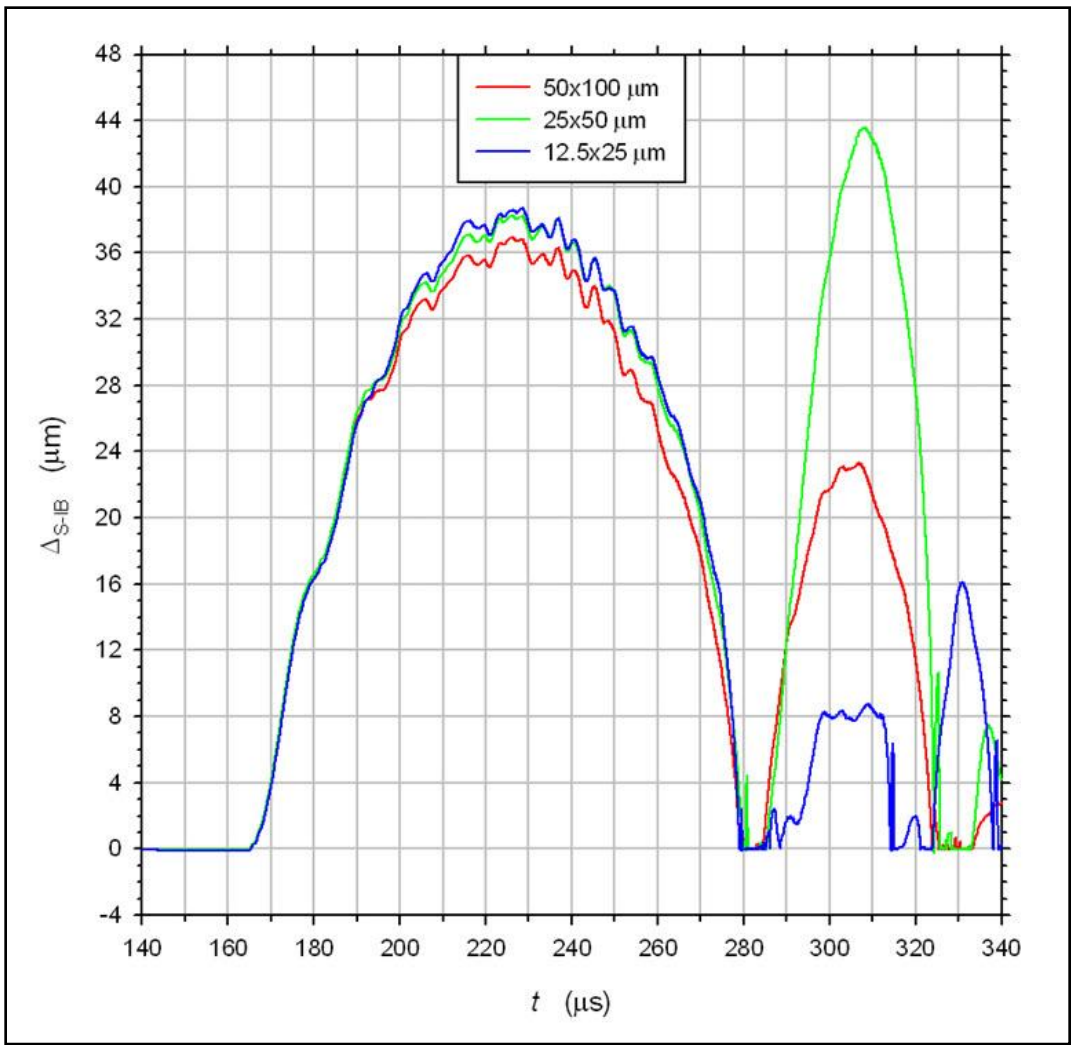

Figure B-1. Histories of the gap sizes on the centerline at the S-IB interface for three specimen meshes and a 1-μs initial rise time for the loading wave.

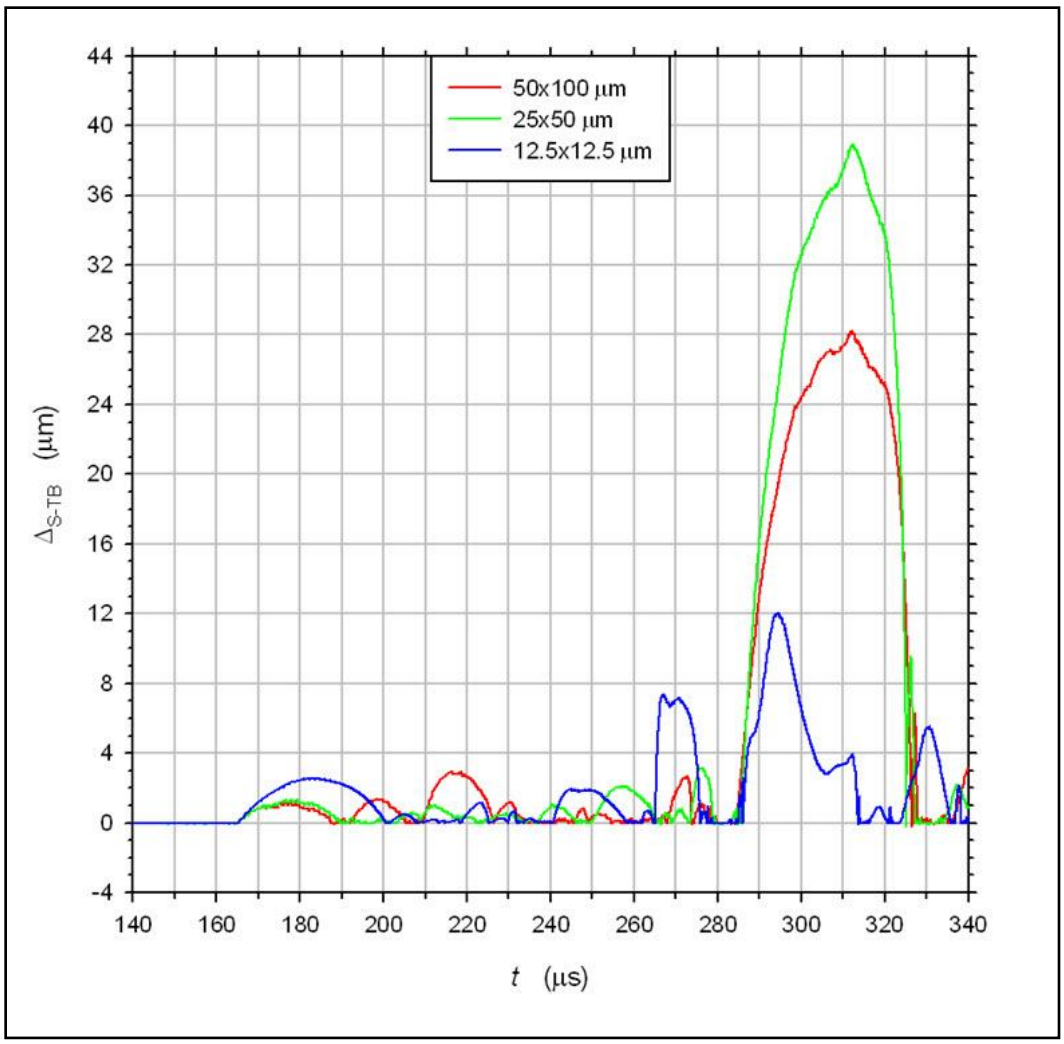

Figure B-2. Histories of the gap sizes on the centerline at the S-TB interface for three specimen meshes and a 1-μs initial rise time for the loading wave.

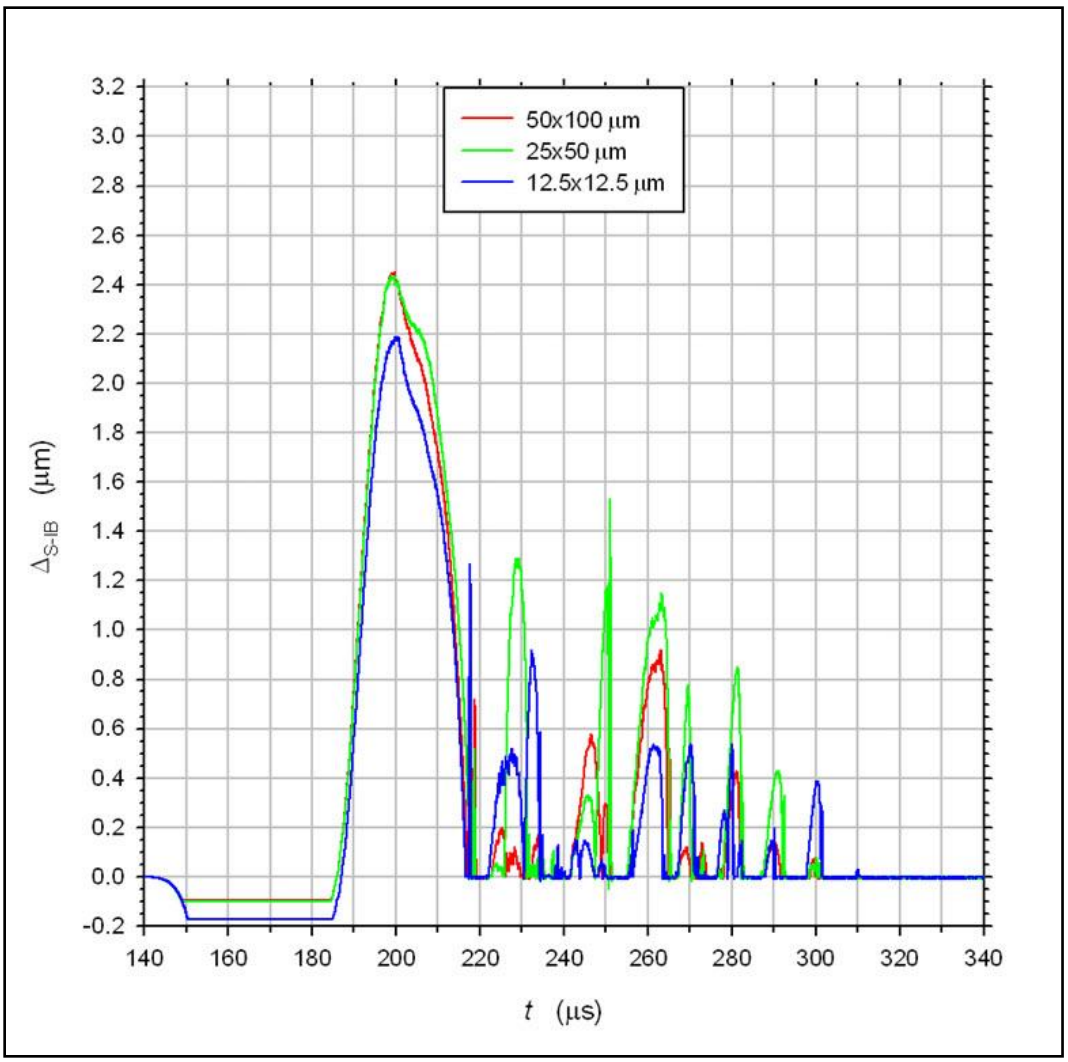

Figure B-3. Histories of the gap sizes on the centerline at the S-IB interface for three specimen meshes and a 25-μs initial rise time for the loading wave.

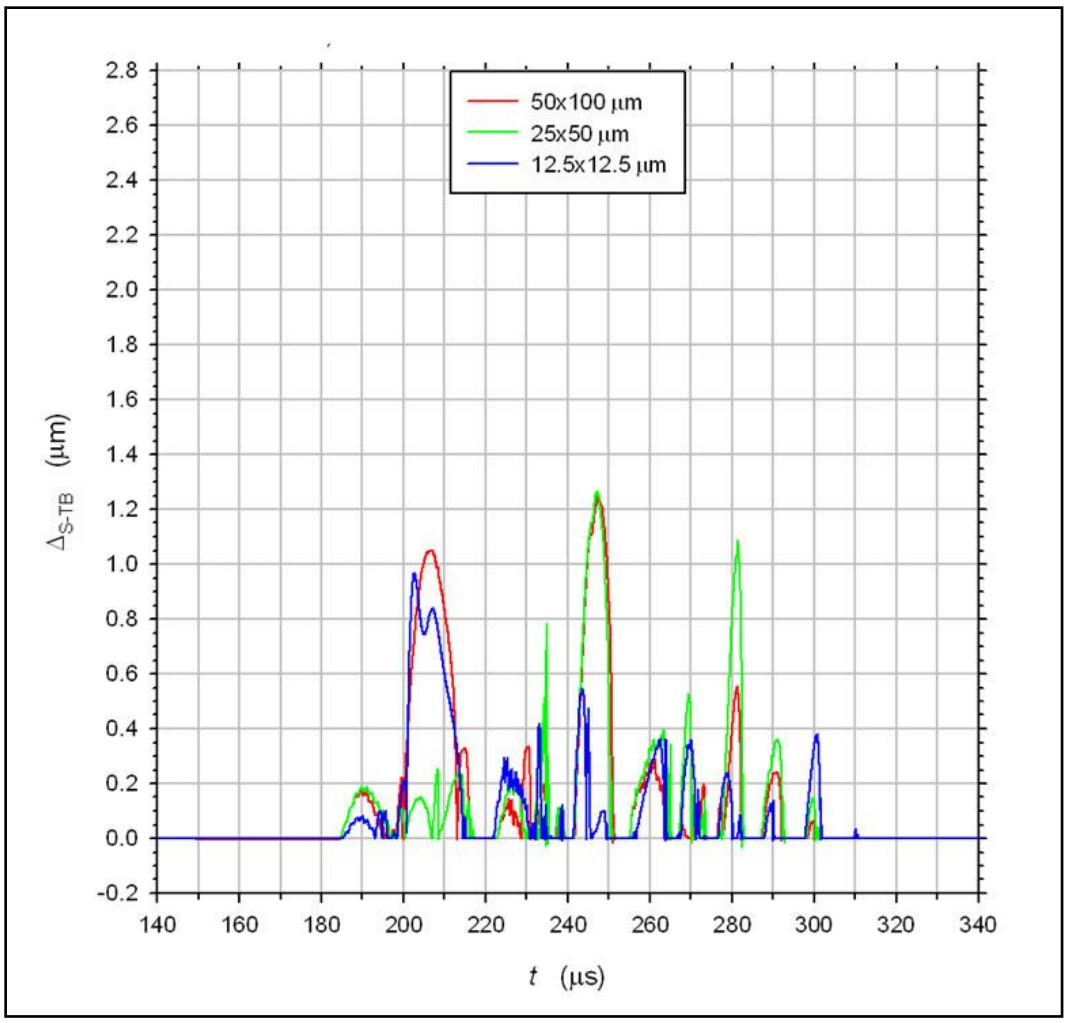

Figure B-4. Histories of the gap sizes on the centerline at the S-TB interface for three specimen meshes and a 25-μs initial rise time for the loading wave.

First, we consider the 1-μs initial rise time for the loading wave. A detailed discussion of the results for this case using the baseline mesh was given in section 6.1, where the gap formation was broken down into six stages. At both interfaces, there is mesh convergence in the onset of the gaps (at 165 μs). For the gap at the S-IB interface (figure B-1), we see that there is substantial mesh convergence in both gap size and duration for Stage II (165–280 μs, during which there is a persistent gap) and Stage III (280–286 μs, during which the gap remains closed). For the gap at the S-TB interface (figure B-2), we see that there is substantial mesh convergence in the duration of Stages II and III, but no convergence in the size of the gap during Stage II. However, the results for all three meshes are qualitatively similar during Stage II, that is, the gap opens and closes several times. For Stage IV (286–324 μs, during which both gaps re-open), there is a degree of convergence in the duration of the gaps at either interface but not in gap size. Convergence has not been achieved at later times.

Next, we consider the 25-μs initial rise time for the loading wave. A discussion of the results for this case using the baseline mesh was given in section 7. At both interfaces, there is mesh convergence in the onset of the gaps. For the gap at the S-IB interface (figure B-3), we see that there is substantial mesh convergence in both gap size and duration during the Stage II (184–218 μs, during which there is a persistent gap); in particular, the timing of the peak value (2.2–2.4 μm) agrees within 1 μs for all three meshes. For other times at the S-IB interface and all times at the S-TB interface (figure B-4), the gap sizes remain under about 1.2 μm; the local peaks in gap size generally occur at similar times; and the gaps persist for similar durations for the three meshes. However, gap sizes generally display less mesh convergence than gap durations.

The results above support the conclusion that the gap phenomenon is not a numerical artifact introduced by an insufficiently fine mesh in the specimen.

B-2 Sensitivity to the Contact Algorithm Parameters

Refer to section 4.2 for a brief discussion of the contact algorithm. Figures B-5, B-6, B-9, and B-10 compare the histories of the gap size on the centerline for three values of the scale factor SFACT: 0.1, 1 and 10, which correspond to a less stiff, the default, and a stiffer penalty force, respectively. Figures B-7, B-8, B-11, and B-12 compare the histories of the gap size on the centerline for two values of the viscous damping coefficient VDC: 10 and 20, which correspond to the default damping and twice the default damping, respectively. Figures B-5–B-8 are for the 1-μs initial rise time for the loading wave; figures B-9–B-12 are for the 25-μs initial rise time. The results at the S-IB interface are given in figures B-5, B-7, B-9, and B-11; those for the S-TB interface are given in figures B-6, B-8, B-10, and B-12.

First, we consider the 1-μs initial rise time for the loading wave (figures B-5–B-8). A detailed discussion of the results for this case using the default values for the contact parameters was given in section 6.1, where the gap formation was broken down into six stages. The durations of Stage II (165–280 μs), Stage III (280–286 μs) and Stage IV (286–324 μs) are unaffected by the changes in SFACT and VDC. The size of the gap at the S-IB interface during Stage II (165–280 μs) is also unaffected by the changes in SFACT and VDC. At other times, the size of the gap at both interfaces varies somewhat with the values of these parameters, but the results are qualitatively similar.

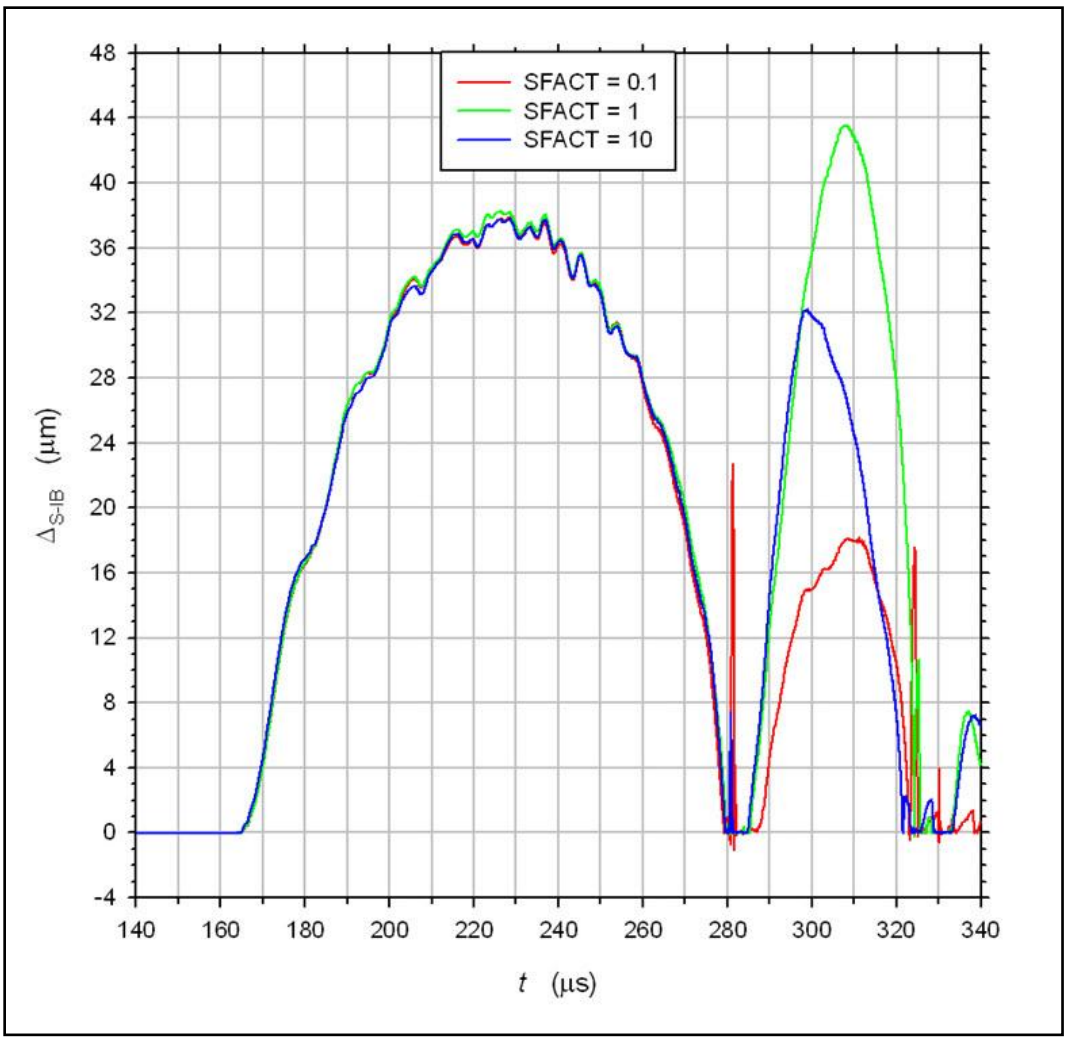

Figure B-5. Histories of the gap sizes on the centerline at the S-IB interface for three values of the contact parameter SFACT and a 1-μs initial rise time for the loading wave.

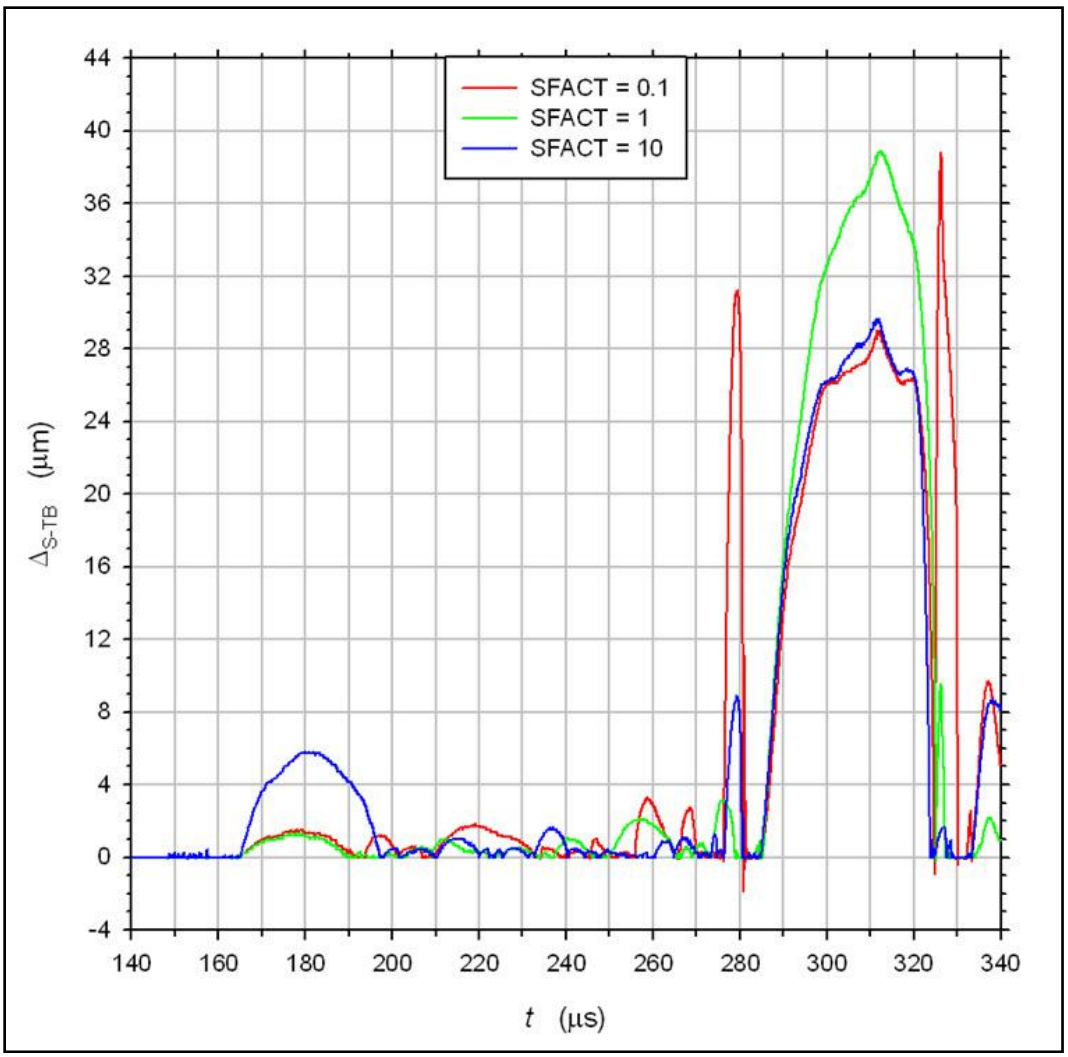

Figure B-6. Histories of the gap sizes on the centerline at the S-TB interface for three values of the contact parameter SFACT and a 1-μs initial rise time for the loading wave.

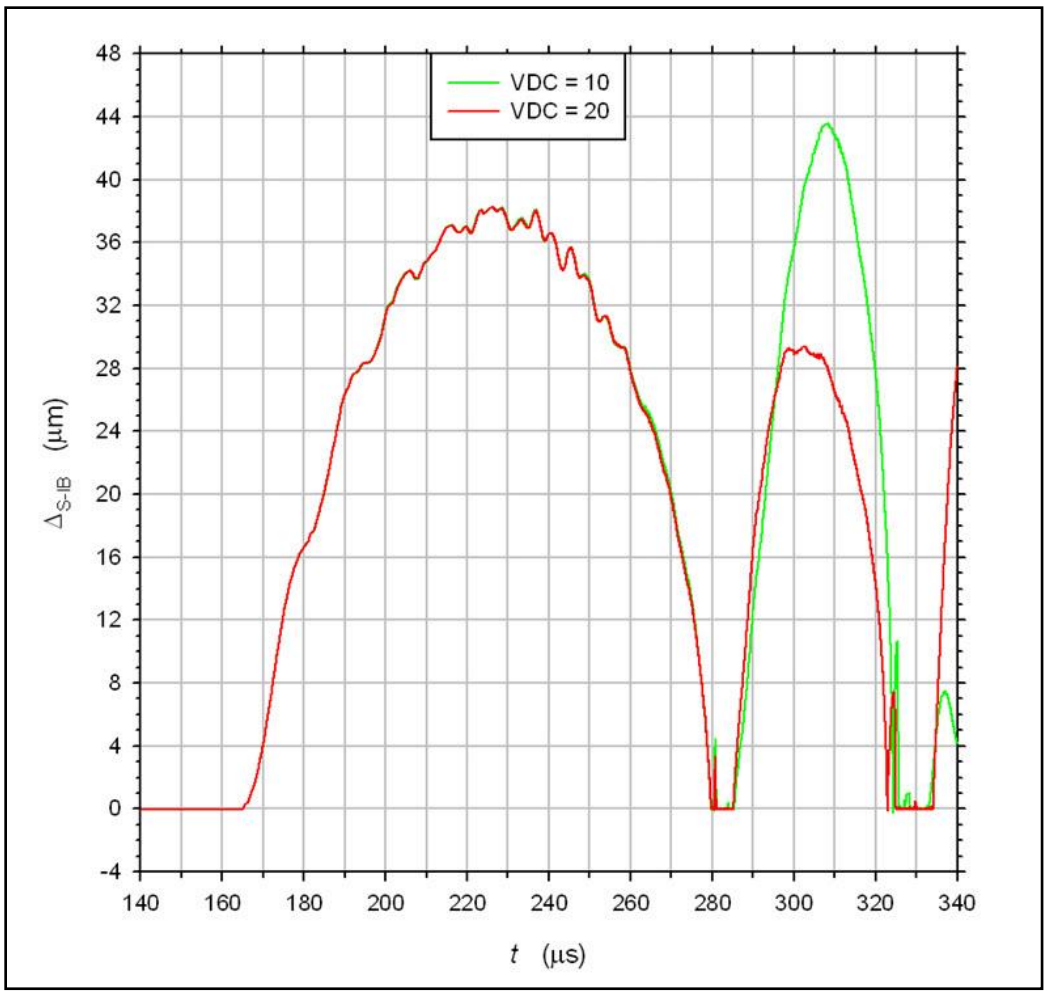

Figure B-7. Histories of the gap sizes on the centerline at the S-IB interface for two values of the contact parameter VDC and a 1-μs initial rise time for the loading wave.

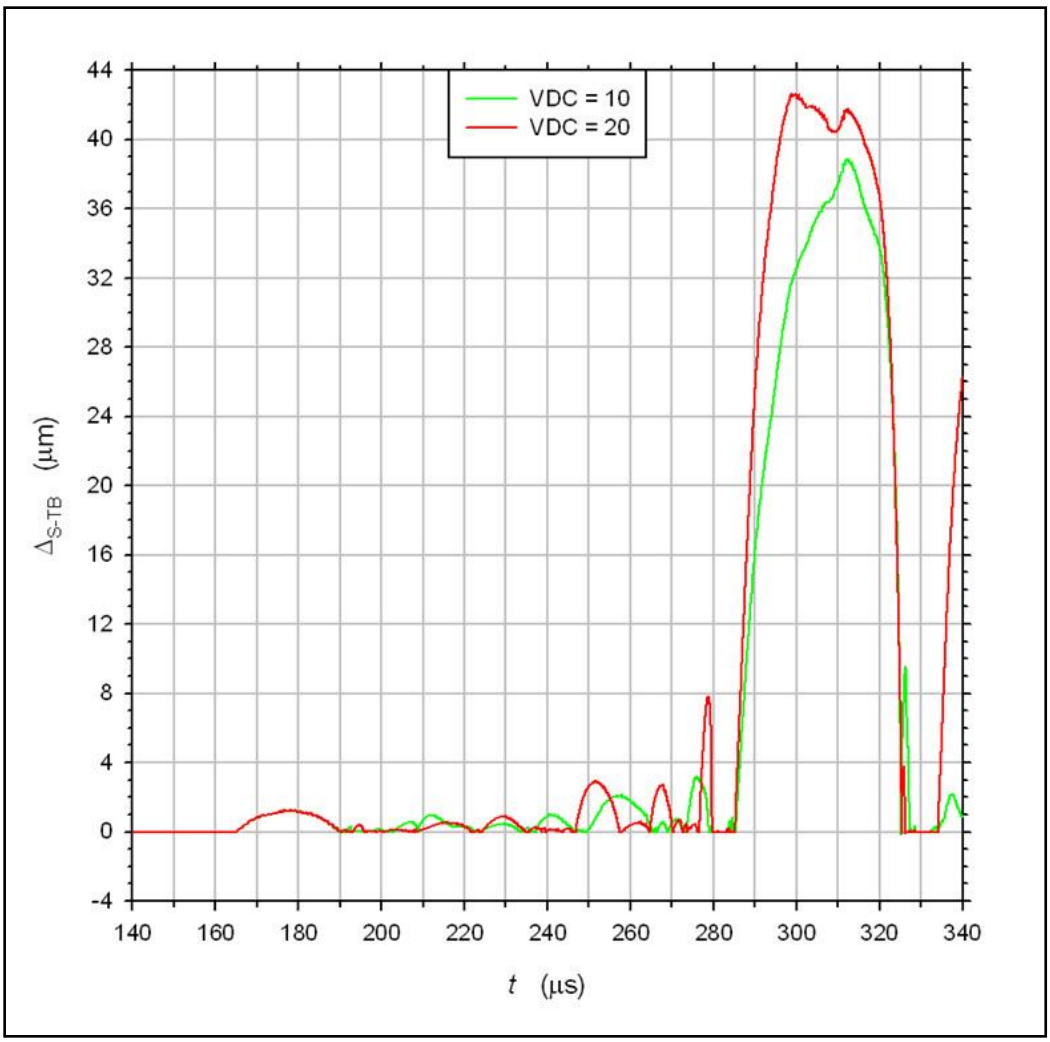

Figure B-8. Histories of the gap sizes on the centerline at the S-TB interface for two values of the contact parameter VDC and a 1-μs initial rise time for the loading wave.

Next, we consider the 25-μs initial rise time for the loading wave (figures B-9–B-12). A discussion of the results for this case using the default values for the contact parameters was given in section 7. At the S-IB interface, we see that doubling VDC has no effect on the duration or size of the gap during the Stage II (184–218 μs). The changes in SFACT also have no effect on the duration and only a slight effect on the size of the gap during this stage; in particular, the peak value occurs at about 200 μs for all three cases. For other times at the S-IB interface and all times at the S-TB interface, doubling VDC has little effect on the duration of the gaps and only a slight effect on their size. The changes in SFACT have more effect on both duration and size, but the results are qualitatively similar.

The results above support the conclusion that the gap phenomenon is not a numerical artifact introduced by the contact algorithm.

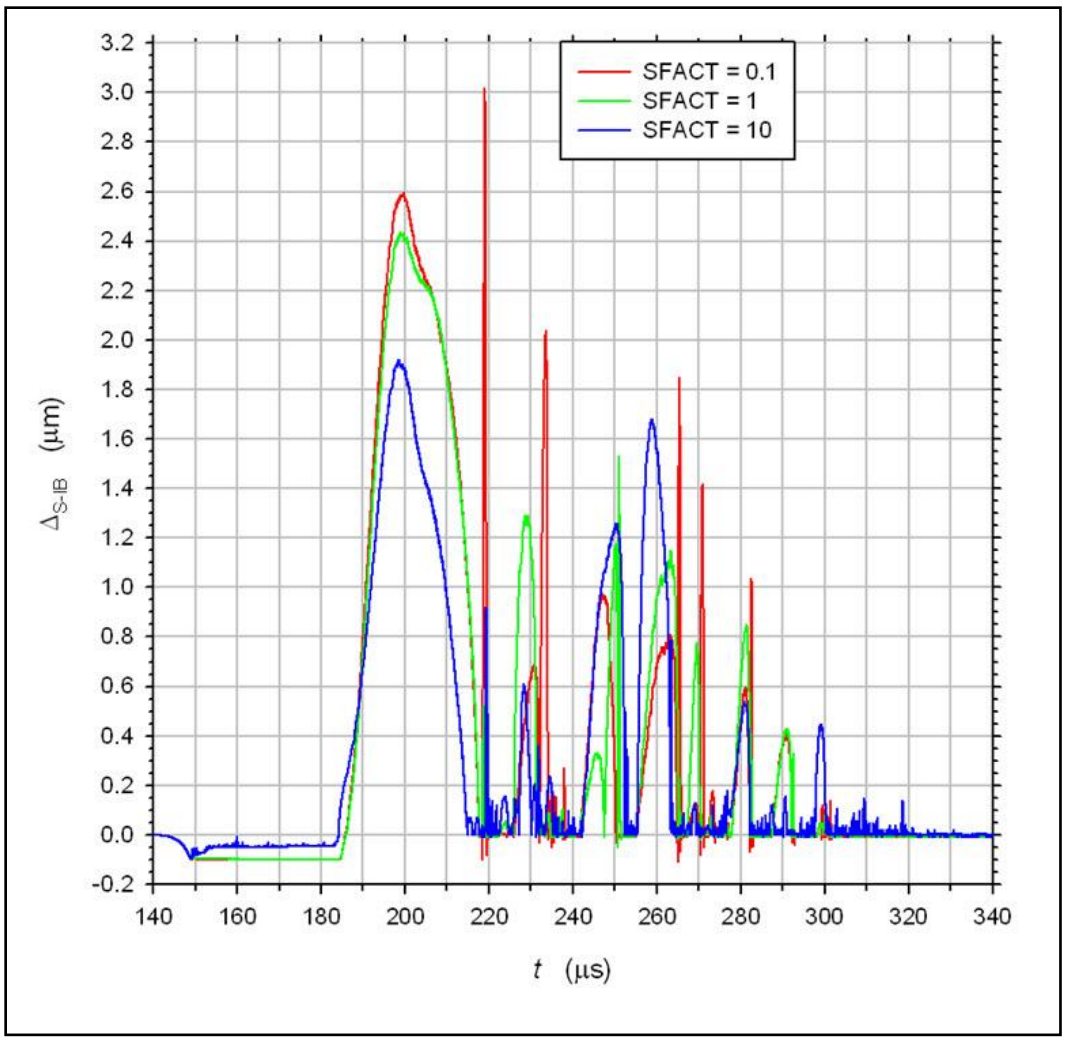

Figure B-9. Histories of the gap sizes on the centerline at the S-IB interface for three values of the contact parameter SFACT and a 25-μs initial rise time for the loading wave.

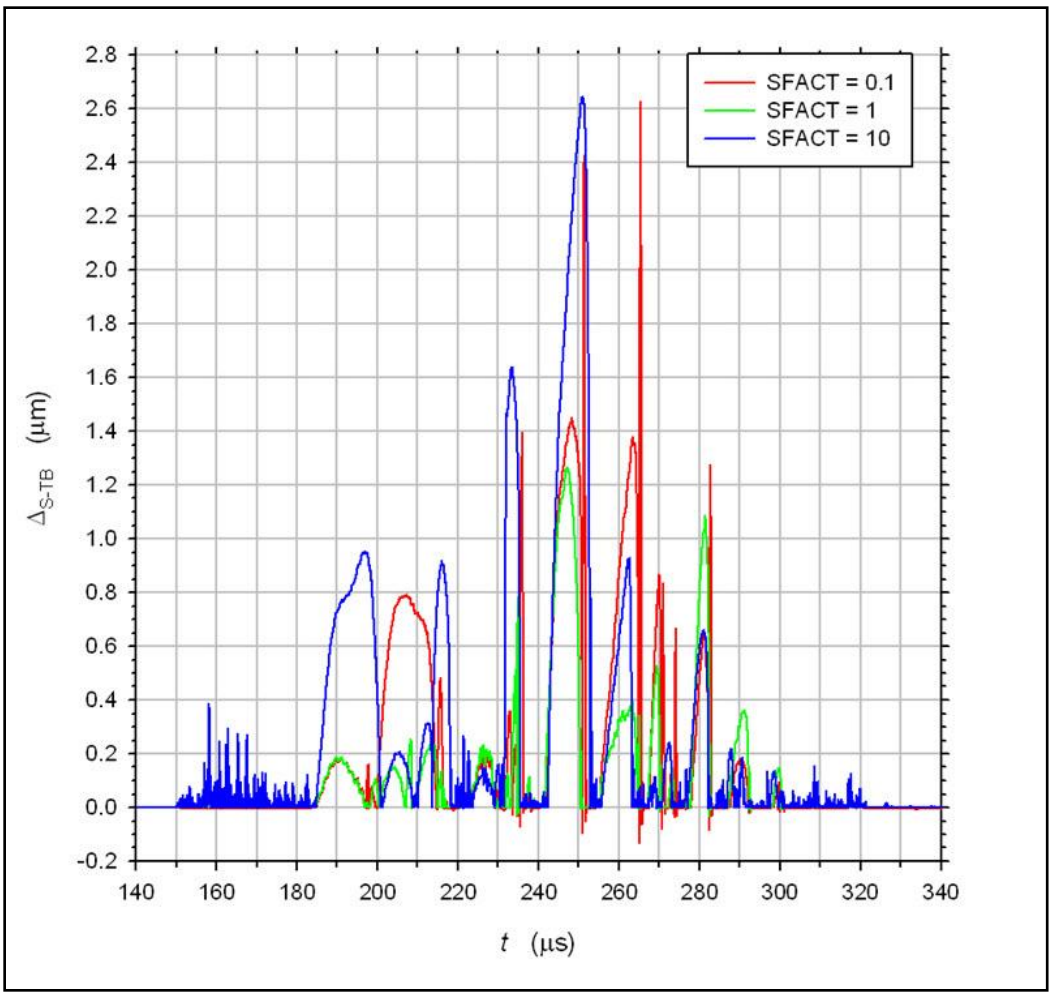

Figure B-10. Histories of the gap sizes on the centerline at the S-TB interface for three values of the contact parameter SFACT and a 25-μs initial rise time for the loading wave.

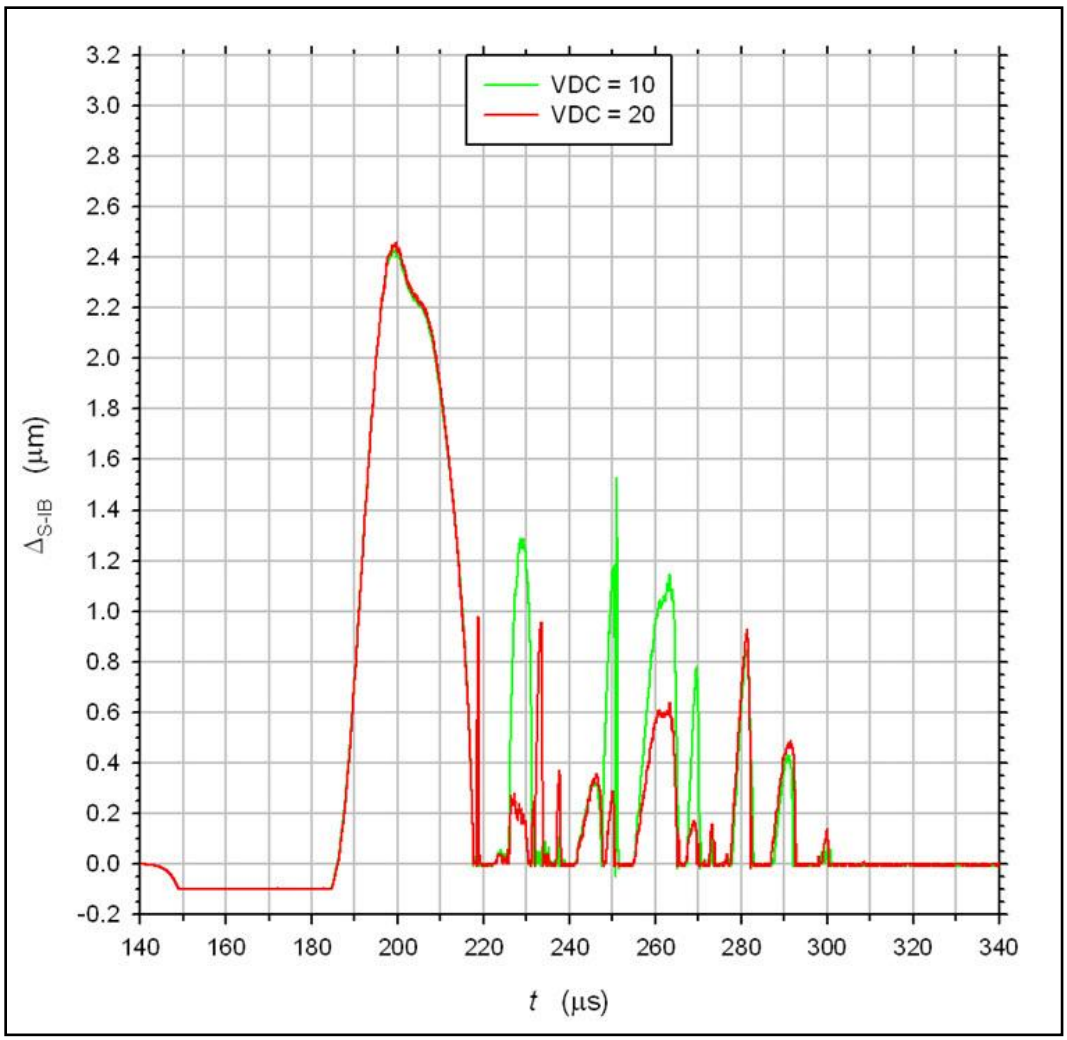

Figure B-11. Histories of the gap sizes on the centerline at the S-IB interface for two values of the contact parameter VDC and a 25-μs initial rise time for the loading wave.

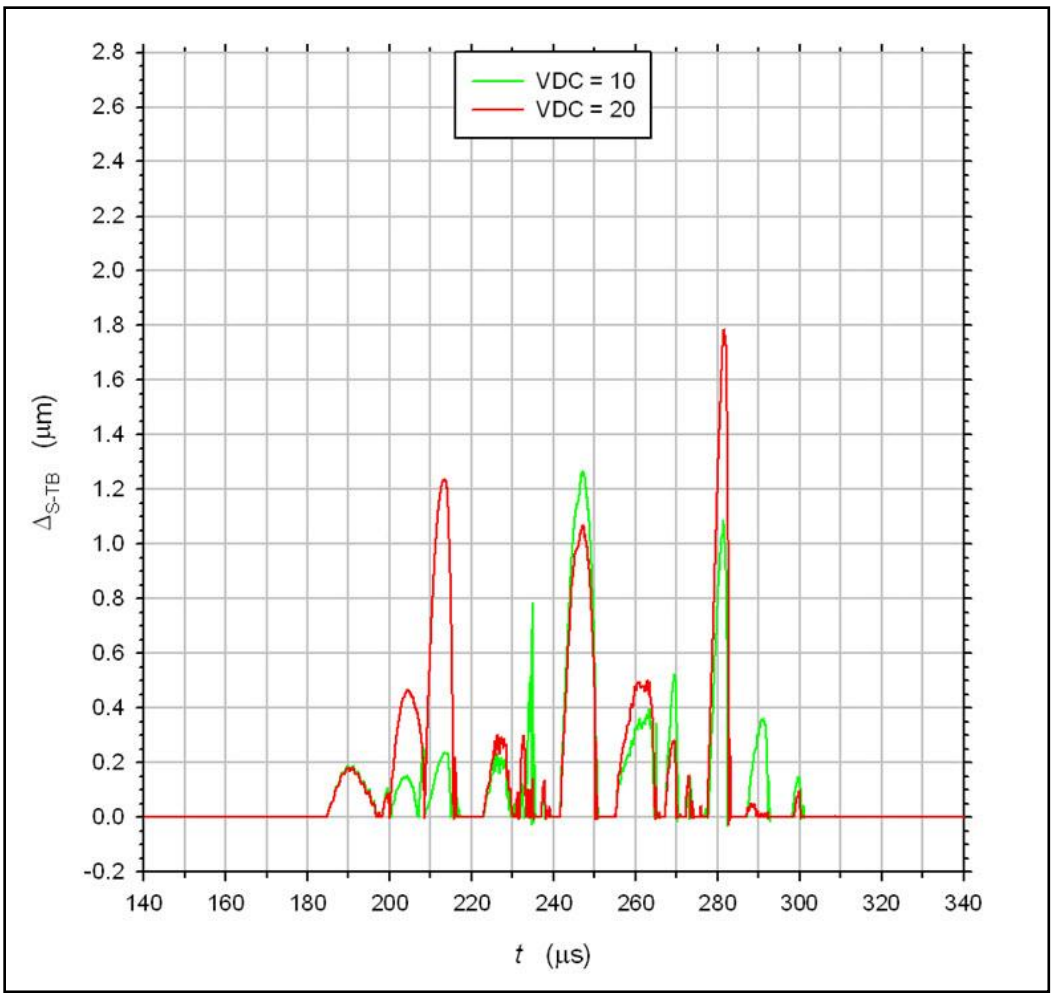

Figure B-12. Histories of the gap sizes on the centerline at the S-TB interface for two values of the contact parameter VDC and a 25-μs initial rise time for the loading wave.

Appendix C. Additional Computational Studies

This section contains summaries of additional numerical simulations in which gaps formed at the specimen-bar interfaces. These simulations involve conditions that differ in one or more ways from those considered previously, and in appendix C-3 they involve the use of a different code.

C-1 Direct Impact on the Specimen

Recall that in a conventional SHPB test, the striker bar impacts the incident bar and generates a compressive stress pulse which propagates along the incident bar and subsequently into the specimen and the transmission bar; and for soft specimens, a pulse shaper is often inserted between the striker and incident bars to produce a smoother loading wave. A variation of the SHPB test, known as the direct impact Hopkinson bar or direct impact compression test, involves the elimination of the incident bar, so that the striker bar directly impacts the specimen (*27–30*). The transmission bar is retained and serves the same purpose as in a conventional SHPB test. The main advantage of this technique is that it permits higher strain rates to be imposed on the specimen. There are some disadvantages as well; see the papers cited above and also the discussions in Gray (*1*) and Jia and Ramesh (*31*).

We performed several simulations in which a striker bar directly impacts the specimen. The specimen geometry, bar diameters, bar properties, and mesh sizes were the default values used previously (sections 2.1, 2.3, and 4.1). The compressible Mooney-Rivlin model (section 3) was used for the specimen. The initial velocity of the striker bar is $v_{SB} = 3.625$ m/s, which yields a nominal axial strain rate of approximately $v_{SB}/L_S = 2500$/s, as before. Note that v_{SB} is twice the plateau velocity v_0 imposed at the far end of the incident bar in the previous SHPB simulations; on the other hand, the particle velocity in the incident bar nearly doubles as the loading wave reflects from the S-IB interface (section 5.3). Thus, in either case an axial velocity of roughly 3.625 m/s is ultimately imposed on the face of the specimen. However, in the SHPB simulations the imposed velocity ramps up smoothly from zero (figures 5 and 6), whereas the direct impact imposes an initial step in velocity (and hence an acceleration impulse) on the specimen. In the subsequent discussion, the SHPB simulation mentioned for purposes of comparison will be the case with a 1-μs initial rise time (section 6), as this case imposed the most severe accelerations on the specimen.

In the SHPB simulation, the velocity at the S-IB interface exhibits large oscillations as a result of wave dispersion in the incident bar (figures 3 and 5). This dispersion effect will be absent for direct impact. Nevertheless, there will be some slight deceleration of the striker bar as well as (possibly large) oscillations in velocity throughout the specimen at early times due to multiple reflections from the specimen-bar interfaces. Unfortunately, we do not have any plots of the velocity history for this case.

In the SHPB simulation, gaps formed at the S-IB and S-TB interfaces about 25 μs after the arrival of the loading wave at the S-IB interface. In the direct impact simulation, gaps formed much sooner at both the specimen-striker bar and S-TB interfaces. In fact, by 6 μs after impact, *the entire face of the specimen had separated from the transmission bar*. This complete separation continued for the short duration of the simulation, which was stopped at about 13 μs after impact, corresponding to a compressive axial strain of about 3%. Prior to gap formation, the peak compressive axial stress in the specimen was about 8 times that for the SHPB simulation. Also, tensile axial stresses on the centerline were first observed in the transmission bar, analogous to the SHPB simulation (section 6.3).

Our goal in doing these direct impact simulations was not to study the direct impact compression test per se, but rather to examine the effect of a different loading history on the formation of gaps. However, the results described above call into question the use of direct impact on soft, nearly incompressible specimens. Indeed, whereas inertial effects at early times in SHPB tests can be reduced (though not eliminated) with better pulse shaping, for a direct impact test there is no way to reduce the acceleration impulse imparted to the specimen.

C-1.1 Lateral Constraints

The lateral surfaces of the specimen and the bars are unconstrained and hence stress-free in both the SHPB and direct impact compression tests. We performed two additional direct impact simulations to examine the effect of these free surfaces on gap formation. The conditions in both simulations were as described above for the direct impact test, with the exceptions noted below.

In the first simulation, the lateral surfaces of the bars and the specimen were constrained to prevent any radial motion, whereas the axial component of the motion at these surfaces was unconstrained as before. No gaps formed in this case. Axial stress contours at 10 μs revealed a uniform compressive stress state throughout the specimen and the bars (in the neighborhood of the specimen), with the exception of a small region of tensile stress adjacent to the portion of the faces of the bars overhanging the specimen. These results are not surprising. Indeed, under these conditions, the specimen essentially undergoes a compressive, uniaxial strain, just as in a normal plate impact test. Since the radial motion throughout the specimen is eliminated for the most part, so are the associated radial inertia effects.

In the second simulation, the lateral constraint on the specimen was removed, but the constraint on the bars was retained. Gaps formed at both interfaces. The results were similar to those for the unconstrained direct impact simulation described previously.

These two simulations support the conclusion that radial inertia effects are responsible for gap formation in the direct impact tests as well.

C-2 Annular Specimens

All of the results presented up to this point have been for solid (disc shaped) specimens. Annular (washer shaped) specimens have also been used in SHPB tests on soft materials in an effort to reduce inertial effects (*5, 6*). The motivation for hollowing out the specimen comes from approximate theoretical estimates for the inertially induced radial stress in solid specimens, which predict that the radial stress is largest on the centerline and decreases parabolically to zero at the lateral (stress-free) surface (*6, 7, 26, 27, 32, 33*). Furthermore, numerical simulations reveal that in situations where gaps do not form but the axial acceleration is sufficiently large, the pressure at the center of a solid specimen may undergo large oscillations (*32, 34*). Therefore, removing the center portion of the specimen might reduce these inertial effects, resulting in a stress state that is closer to uniaxial. Experimental results indicate that this works for early times (*5, 6*).[52]

We performed several numerical simulations on an annular specimen with the same initial thickness (L_S = 1.45 mm) and initial outer radius (R_S = 6.35 mm) as the solid specimens discussed previously. The inner radius of the annular specimen was taken to be 2.638 mm. As before, we considered two values for the radius of the pressure bars, R_B = 12.8 mm and R_B = 9.5 mm. The dimensions of the annular specimen and the smaller bar radius were chosen to agree with those used in the experimental study on ballistic gelatin by Moy et al. (*5*).[53] The compressible Mooney-Rivlin model was used for all annular specimen simulations.

For the larger diameter pressure bars and a 25-μs initial rise time for the loading wave, the total force acting on a cross-section of the incident and transmission bars was measured at an axial location of 2.52 mm from the specimen-bar interfaces (cf. section 7.3). The force history in the transmission bar was qualitatively similar to that for the solid specimen (figure 30), although the negative forces (indicating gap opening) persisted for a shorter time. The force history in the incident bar oscillated between positive and negative from 157 μs to the end of the simulation at 340 μs (43% nominal axial strain), indicating repeated gap opening and closure.

For the smaller diameter pressure bars and a 25-μs initial rise time, no gaps were observed except momentarily (at about 7% axial strain) at the S-IB interface over a small region midway between the inner and outer surfaces.

For the smaller diameter pressure bars and a 1-μs initial rise time for the loading wave, a substantial gap was observed at the S-IB interface but not the S-TB interface. At t = 182 μs and an axial strain of 7%, this gap extends over ¾ of the S-IB interface, as seen in figure C-1. This figure also reveals bulging of the annular specimen at the outer (top) and inner (bottom) stress-free lateral surfaces, near the S-IB interface. The centerline of the specimen and bars lies outside

---

[52] However, theoretical and computational results demonstrate that the presence of a stress-free inner surface leads to additional inertial effects at later times (*32, 36*). This complication will not be discussed further here.

[53] Actually, the inner radius of the annular specimen used here is 1% smaller than the value used in Moy et al. (*5*). The reason for this slight difference is that it allowed us to use the same mesh size for the solid and annular specimens.

of (below) the figure. Figure C-1 also shows contours of the pressure. In order to reveal more clearly the regions of negative (tensile) pressure, any point with zero or positive pressure (compression) is shaded red; any color other than red indicates a tensile state. The figure reveals a region of tensile pressure in the specimen bordering the gap at the S-IB interface.

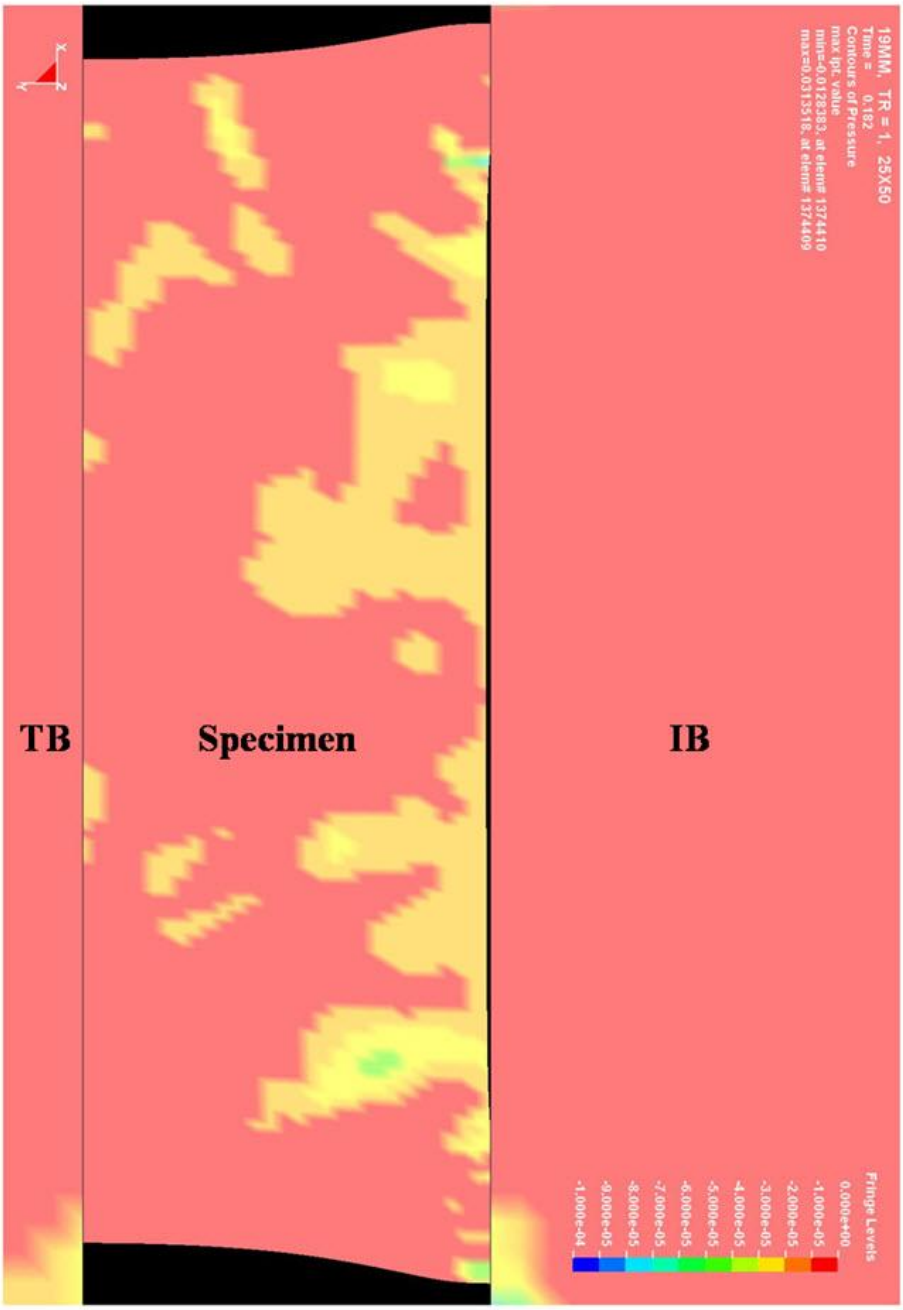

Figure C-1. Pressure contours in the vicinity of an annular specimen at 7% axial strain. Any positive pressure (compression) is shaded red; other colors indicate negative (tensile) pressure in units of GPa. The loading wave had a 1-μs initial rise time. Observe the gap along most of the S-IB interface.

C-3 Simulations with the PRESTO Code

With the exception of the results to be discussed in this section, all of the numerical simulations in this report used the commercial finite-element code LS-DYNA (*8, 9*) in the 2-D axisymmetric mode. In an effort to verify that the formation of gaps at the specimen-bar interfaces is not some artifact of this particular code, Bryan Love (*37*) performed analogous numerical simulations with PRESTO, a finite-element code from Sandia National Laboratories. All of the PRESTO simulations were fully three-dimensional, which necessitated larger element sizes than those used in the LS-DYNA simulations. The two codes also have different contact algorithms.

A compressible version of the Mooney-Rivlin model was used for the specimen, with the same calibration used in the LS-DYNA simulations (see section 3).[54] Both solid and annular specimens were considered; these had the same dimensions as in the LS-DYNA simulations.

The diameter of the aluminum pressure bars used in these simulations was 1 inch (25.4 mm), which is essentially the larger of the two diameters considered previously. The pressure bars were much longer (2438 mm) than in the LS-DYNA simulations, corresponding to the bar lengths in an actual Hopkinson bar setup (*25*). The loading condition in the PRESTO simulations involved an aluminum striker bar (of the same diameter) impacting the far end of the incident bar, as in a real SHPB test. However, no pulse shaper was used between the striker and incident bars. A few direct impact simulations were also performed.

The results of these PRESTO simulations confirmed the findings of the previous LS-DYNA simulations with regard to the formation of gaps at the specimen-bar interfaces. The fact that the PRESTO simulations were fully three-dimensional rules out the possibility that gap formation in the LS-DYNA simulations was in some way associated with issues at the centerline in the 2-D axisymmetric mode.

[54] However, the PRESTO version of the compressible Mooney-Rivlin model does not suffer from the unrealistic behavior of the pressure at very large volumetric compression and high Poisson's ratio that is exhibited by the LS-DYNA version (see appendix A-3).

List of Symbols, Abbreviations, and Acronyms

A_1, A_2	constants in the Mooney-Rivlin model
c_L, c_G, c_E	longitudinal, shear, and bar wave speeds
E	Young's modulus
e_z	nominal axial strain in the specimen
F_z	total force on a cross-section of the transmission bar
G	shear modulus
IB	incident bar
J	Jacobian of the deformation
K	bulk modulus
L	longitudinal modulus
L_{IB}	length of the incident bar
L_{S}	initial length (thickness) of the specimen
L_{TB}	length of the transmission bar
p	pressure
r	radial coordinate of the deformed material
R	radial coordinate of the undeformed material
R_{B}	radius of the incident and transmission bars
R_{S}	initial radius of the specimen
S	specimen
SFACT	scale factor for the penalty force stiffness in the contact algorithm
SHPB	split Hopkinson pressure bar
S-IB	specimen-incident bar
S-TB	specimen-transmission bar
t	time
TB	transmission bar
t_R	rise time of the axial velocity prescribed at the end of the incident bar

u_{IB}, $u_{S\text{-}IB}$	axial displacements of the incident bar and specimen at the S-IB interface
u_{TB}, $u_{S\text{-}TB}$	axial displacements of the transmission bar and specimen at the S-TB interface
v_0	plateau value of the axial velocity prescribed at the end of the incident bar
VDC	viscous damping coefficient in the contact algorithm
v_{IB}, v_{TB}	axial velocity of the incident and transmission bars at the specimen interface
v_z	axial velocity of the incident bar
z	axial coordinate of the deformed material
Z	axial coordinate of the undeformed material
z_{IB}, $z_{S\text{-}IB}$	deformed axial coordinates of the incident bar and specimen at the S-IB interface
z_{TB}, $z_{S\text{-}TB}$	deformed axial coordinates of the transmission bar and specimen at the S-TB interface
$\Delta_{S\text{-}IB}$	gap size at the specimen-incident bar interface
$\Delta_{S\text{-}TB}$	gap size at the specimen-transmission bar interface
ν	Poisson's ratio
λ_S	deformed length (thickness) of the specimen
λ_z, λ_r, λ_θ	axial, radial, and hoop stretches in the specimen
$\boldsymbol{\sigma}$	Cauchy (true) stress tensor
ρ	initial density
σ_{zz}, σ_{rr}, $\sigma_{\theta\theta}$	axial , radial, and hoop components of the Cauchy stress

NO. OF COPIES ORGANIZATION

1 (PDF ONLY) DEFENSE TECHNICAL INFORMATION CTR
DTIC OCA
8725 JOHN J KINGMAN RD
STE 0944
FORT BELVOIR VA 22060-6218

1 DIRECTOR
US ARMY RESEARCH LAB
IMNE ALC HRR
2800 POWDER MILL RD
ADELPHI MD 20783-1197

1 DIRECTOR
US ARMY RESEARCH LAB
RDRL CIM L
2800 POWDER MILL RD
ADELPHI MD 20783-1197

1 DIRECTOR
US ARMY RESEARCH LAB
RDRL CIM P
2800 POWDER MILL RD
ADELPHI MD 20783-1197

1 DIRECTOR
US ARMY RESEARCH LAB
RDRL D
2800 POWDER MILL RD
ADELPHI MD 20783-1197

3 INSTITUTE FOR ADVANCED TECHNOLOGY
S BLESS
S SATAPATHY
S LEVINSON
3925 WEST BRAKER ST
SUITE 400
AUSTIN TX 78759-5316

3 SOUTHWEST RESEARCH INSTITUTE
C A ANDERSON
J WALKER
K DANNEMANN
6220 CULEBRA RD
DRAWER 28510
SAN ANTONIO TX 78228-0510

NO. OF COPIES ORGANIZATION

4 SOUTHWEST RESEARCH INSTITUTE
G JOHNSON
T HOLMQUIST
S BEISSEL
C GERLACH
5353 WAYZATA BLVD
MINNEAPOLIS MN 55416-1340

1 INTERNATIONAL RESEARCH ASSOCIATES
D ORPHAL
4450 BLACK AVE STE E
PLEASANTON CA 94566-6145

4 JOHNS HOPKINS UNIVERSITY MECHANICAL ENGINEERING
K T RAMESH
A DOUGLAS
K HEMKER
T NGUYEN
223 LATROBE HALL
3400 N CHARLES ST
BALTIMORE MD 21218-2682

1 JOHNS HOPKINS UNIVERSITY CIVIL ENGINEERING
L GRAHAM-BRADY
210 LATROBE HALL
3400 N CHARLES ST
BALTIMORE MD 21218-2682

1 VIRGINIA POLYTECHNIC INST COLLEGE OF ENGRG
R BATRA
BLACKSBURG, VA 24061-0219

1 LIVERMORE SOFTWARE TECHNOLOGY CORP
M JENSEN
7374 LAS POSITAS RD
LIVERMORE CA 94550

1 UNIVERSITY OF ALABAMA AT BIRMINGHAM
MECHANICAL ENGINEERING
D LITTLEFIELD
HOEN ENGINEERING BLDG
1530 3RD AVE S
BIRMINGHAM AL 35294-4440

NO. OF COPIES ORGANIZATION

1 PURDUE UNIVERSITY
AERONAUTICS & ASTRONAUTICS
W CHEN
701 W STADIUM AVE
W. LAFAYETTE IN 47907-2045

1 UNIVERSITY OF RHODE ISLAND
MECHANICAL ENGINEERING
A SHUKLA
206 WALES HALL
KINGSTON RI 02881

1 UNIVERSITY OF MISSISSIPPI
MECHANICAL ENGINEERING
A RAJENDRAN
201 CARRIER HALL
UNIVERSITY MS 38677

2 UNIVERSITY OF CALIFORNIA
SAN DIEGO
MECHANICAL AND AEROSPACE
ENGINEERING
M MEYER
V NESTERENKO
9500 GILMAN DR
LA JOLLA CA 92093-0411

1 UNIVERSITY OF CALIFORNIA
SAN DIEGO
DEPT APPLIED MECH & ENG SCI
S NEMAT-NASSER
9500 GILMAN DR
LA JOLLA CA 92093-0416

1 UNIVERSITY OF UTAH
MECHANICAL ENGINEERING
R BRANNON
50 S CENTRAL CAMPUS DR
SALT LAKE CITY UT 84112

1 BROWN UNIVERSITY
ENGINEERING DIV
R CLIFTON
182 HOPE ST
PROVIDENCE, RI 02912

1 UNIVERSITY OF TEXAS-AUSTIN
AEROSPACE ENGINEERING AND
ENGINEERING MECHANICS
K RAVI-CHANDAR
1 UNIVERSITY STATION, C0600
AUSTIN TX 78712-0235

NO. OF COPIES ORGANIZATION

2 UNIVERSITY OF NEBRASKA-
LINCOLN
DEPT OF ENGINEERING MECHANICS
R FENG
M NEGAHBAN
LINCOLN NE 68588-0526

1 STANFORD UNIVERSITY
MECHANICS AND COMPUTATION
GROUP
ATTN A LEW
WILLIAM F DURAND BLDG
STANFORD CA 94305

1 UNIV OF DELAWARE
CTR FOR COMPOSITE MTRLS
ATTN B GAMA
201 SPENCER LABORATORY
NEWARK DE 19716

1 UNIV OF DELAWARE
CTR OF COMPOSITE MTRLS
ATTN S LOPATNIKOV
215 CONPOSITES MANUFAC SCI LAB
NEWARK DE 19716

1 UNIV OF DELAWARE CTR FOR
COMPOSITE MATERIALS
ATTN J GILLESPIE
201 SPENCER LAB
NEWARK DE 19716

1 UNIVERSITY OF FLORIDA
MECHANICAL AND AEROSPACE
ENGINEERING
ATTN G SUBHASH
GAINESVILLE FL 32611

1 UNIVERSITY OF WATERLOO
DEPT OF MECHANICAL
ENGINEERING
ATTN C P SALISBURY
WATERLOO ONTARIO CANADA

2 AIR FORCE RESEARCH
LABORATORY
RWMW
J L JORDAN
L CHHABILDAS
101 WEST EGLIN BLVD
EGLIN AFB FL 32542

NO. OF
COPIES ORGANIZATION

5 SANDIA NATIONAL LABORATORIES
M R BAER MS 0836
S SILLING MS 1322
E S HERTEL MS 1185
S SCHUMACHER MS 0836
P A TAYLOR MS 1160
P O BOX 5800
ALBUQUERQUE NM 97185

2 SANDIA NATIONAL LABORATORIES
T J VOGLER MS 9402
B SONG MS 9404
P O BOX 969
LIVERMORE CA 94551-0969

8 LOS ALAMOS NATIONAL LABORATORY
E N BROWN
G GRAY III
E MAS
D DATTLEBAUM
T MASON
P RAE
J WALTER
B E CLEMENTS
P O BOX 1663
LOS ALAMOS, NM 87545

2 LAWRENCE LIVERMORE NATIONAL LABORATORY
D GOTO
M MURPHY
P O BOX 808
LIVERMORE, CA 94551-0808

1 APPLIED RESEARCH ASSOCIATES SOUTHWEST DIVISION
D E GRADY
4300 SAN MATEO BLVD NE
ALBUQUERQUE NM 87110

1 T W WRIGHT
4906 WILMSLOW RD
BALTIMORE MD 21210

1 M J FORRESTAL
1805 NEWTON PL NE
ALBUQUERQUE NM 87106

NO. OF
COPIES ORGANIZATION

ARMY RESEARCH OFFICE:

1 RDRL ROE M
D STEPP
1 RDRL ROE N
B LAMATTINA

ABERDEEN PROVING GROUND

93 DIR USARL
RDRL CIM G (BLDG 4600)
RDRL CIH C
D GROVE
J CAZAMIAS
P CHUNG
J KNAP
RDRL SL
R COATES
RDRL SLB W
W MERMAGEN
RDRL WM
P PLOSTINS
J MCCAULEY
J SMITH
RDRL WML
J NEWILL
M ZOLTOSKI
RDRL WML H
M FERMEN-COKER
L MAGNESS
D SCHEFFLER
S SCHRAML
RDRL WMM
J BEATTY
R DOWDING
RDRL WMM B
B CHEESEMAN
C FOUNTZOULIS
G GAZONAS
D HOPKINS
P MOY
B POWERS
C RANDOW
M VANLANDINGHAM
R WILDMAN
RDRL WMM C
R JENSEN
RDRL WMM D
E CHIN
RDRL WMM G
J LENHART

NO. OF COPIES ORGANIZATION

RDRL WMP
P BAKER
S SCHOENFELD
RDRL WMP A
B RINGERS
RDRL WMP B
C ADAMS
R BECKER
S BILYK
J BRADLEY
D CASEM
J CLAYTON
A DAGRO
D DANDEKAR
A DWIVEDI
M GREENFIELD
C A GUNNARSSON
RDRL WMP B
C HOPPEL
J HOUSKAMP
Y HUANG
R KRAFT
B LEAVY
B LOVE
M LYNCH
J NIEMCZURA
M RAFTENBERG (5 COPIES)
M SCHEIDLER (10 COPIES)
T WEERASOORIYA
C WILLIAMS
K ZIEGLER
RDRL WMP C
T BJERKE
K KIMSEY
S SEGLETES
W WALTERS
RDRL WMP D
R DONEY
J RUNYEON
B SCOTT
RDRL WMP E
P BARTKOWSKI
M BURKINS
T JONES
E HORWATH
C KRAUTHAUSER
M LOVE

NO. OF COPIES ORGANIZATION

RDRL WMP F
R BITTING
E FIORAVENTE
D FOX
A FRYDMAN
N GNIAZDOWSKI
R GUPTA
RDRL WMP G
R BANTON
N ELDREDGE
S KUKUCK

INTENTIONALLY LEFT BLANK.